THE BELL SYSTEM TECHNICAL JOURNAL

DEVOTED TO THE SCIENTIFIC AND ENGINEERING ASPECTS OF ELECTRICAL COMMUNICATION

Volume 58 November 1979 Number 9

Copyright © 1979 American Telephone and Telegraph Company. Printed in U.S.A.

A Gallium-Arsenide Laser Facsimile Printer

By R. C. MILLER, R. H. WILLENS, H. A. WATSON, L. A. D'ASARO, and M. FELDMAN

(Manuscript received May 23, 1979)

We summarize the development of a high-resolution facsimile printing system in which miniature archival images are machined in metal film by a pulsed, focused, scanning laser beam. The film is designed to machine at optical energies within the pulse-power capabilities of GaAs semiconductor lasers. The images are instantly available, as machined, for rear-projection viewing in a compact desk-top printer. Frames of 8 × 10 mm area containing 3.3 × 10^6 pixels and demonstrating up to seven distinguishable gray levels have been written in 12 seconds. Extensive data on hole machining in partially oxidized, low-melting-temperature, metal films are marshalled to show that single-layer films are inhospitable media for facsimile machining with GaAs lasers. We describe a two-layer film consisting of about 600Å of bismuth followed by approximately 650Å of selenium evaporated onto a low-surface-energy substrate. This selenium thickness is antireflective at the laser wavelength, and the composition is nearly stoichiometric for Bi_2Se_3. A strongly exothermic reaction occurs when molten bismuth and selenium mix in the irradiated area. We present data illustrating the machining performance of this film with a thick-cavity, GaAlAs, double-heterostructure laser providing 300 mW of peak power at 3-percent duty factor and 0.1-μs pulse duration and give examples of the image quality obtained in raster-scanned, hole-array machining. Studies of film adhesion, scratch resistance, and shelf life are summarized. Several diffraction-limited optical systems for acquiring, deflecting, and focusing the GaAs beam onto the film, cylindrically corrected for astigmatism and

ellipticity, are described, and several laser properties which affect image machining adversely are characterized.

I. INTRODUCTION

This paper describes the printing of miniature, high-resolution, pictorial images[1] by machining with a gallium-arsenide laser. The focused beam from a pulse-modulated laser is raster-scanned over a thin metal film deposited on a transparent plastic substrate. The energy in each burst of laser power is controlled in correspondence with a transmitted signal so as to machine an array of holes in the metal film.[2] This signal may correspond to the optical reflectivity of a remotely located, synchronously scanned, original document, or it may represent the machining instructions of a graphics-generating computer.

A capability for high resolution is intrinsic to this printing method. The machined image can readily contain 1600 hole sites per line and 2000 lines per frame, and is similar in appearance to a frame of microfilm or microfiche. The pulse repetition rate, raster scanning speeds, and maximum pulse energy are chosen such that the holes machined in "all-white" regions of the image are nearly contiguous. These regions are about 50 percent transparent to visible light. Unmachined regions are <1 percent transparent to visible light. With suitable projection optics, the received portion of a frame can be viewed while the remainder is still being transmitted. Such a projection receiver need be little larger than a conventional microfilm viewer of comparable screen dimensions. The machined image is available without further processing as an archival record.

Hole machining begins at a threshold laser intensity whose value depends on various optical, thermodynamic, mechanical, and—in the case of certain metal composites—chemical parameters of the film. It also depends on the heat loss mechanism, which is usually dominated[3] by thermal conduction to the plastic substrate. Such conduction losses are greatly decreased if energy is supplied to the film in short-duration, high-peak-power bursts,[2] rather than in a low-average-power, continuous-duty stream.[4] Thus, with careful attention given to the output beam optical quality, cavity-dumped He-Ne, ArII, and Nd:YAG lasers, supplying 1 to 2 W power in 30-ns-duration bursts, have overcome the machining threshold of thin bismuth films sufficiently to produce satisfactory images.

Present GaAs lasers[5,6] cannot machine useful images in pure bismuth films. Pulse energies comparable to those from cavity-dumped lasers can be attained from GaAs only by roughly trebling the pulse duration with consequently increased heat conduction loss in the film and decreased machining efficiency. Further, a significant portion of the

GaAs power is dispersed into secondary nonmachining modes, making its beam inferior for machining to the nearly Gaussian beam profiles produced by gas and YAG lasers. Thus, the development of a film with machining threshold several times less than that of bismuth is the key to realizing GaAs as a practical laser machining source.

The advantages of GaAs are large. The low cost and small size of GaAs lasers, together with the inherent mechanical stability of their cavities and the simplicity with which they can be modulated by low voltage pulses, suggest the possibility of a moderately priced, compact, high-speed, facsimile receiver with superior resolution, a useful gray scale range, and instantly accessible images. The miniature size of these images and the capability of laser-machining additional information onto unwritten areas of the film can be advantageous in many information storage applications.

II. GENERAL DESCRIPTION OF FRAME MACHINING

The film transparent substrate is a 100-μm-thick, polyester base overcoated on one side with a low-surface-energy acrylic polymer. A 600 Å-thick layer of bismuth is evaporated onto the polymer, and about 650Å of selenium is evaporated onto the bismuth. The chosen selenium thickness is antireflective for air-incident radiation at 0.885-μm wavelength, permitting about 85 percent of the incident laser power to be absorbed in the bismuth layer. This type of composite film presents interesting points of comparison with the amorphous arsenic-telluride film recently proposed[7] for obtaining cleanly machined holes in optically recorded video disks.

The energy delivered by the pulsed beam melts a disk of Bi-Se whose radius depends on the intensity profile of the focused beam, on the pulse duration, and on the heat loss rate to the substrate. Surface tension pulls this liquid towards the solid periphery where it piles up and freezes into a narrow rim. An exothermic reaction[8] occurs when the molten bismuth and selenium mix; the released energy, in combination with the increased absorption due to the selenium antireflective property, more than offsets the thermal mass added by the selenium. Assisted by the low surface energy at the polymer interface, the Se/Bi bilayer can achieve machining threshold at laser beam intensities four to six times lower than those required for bismuth alone.

Metal "tektites" are strewn beyond the hole boundary at all machining energies, and some metal is ejected from the film at high machining energies. However, the primary function of the absorbed optical energy is to unlock surface forces which displace metal into the peripheral rim surrounding the hole. Image white areas are local regions of nearly contiguous holes, each bordered by piled-up metal; such regions are about 50 percent transparent to visible light. Image

black areas contain no machined holes, and their transparency is less than 1 percent. Gray-scale effects can be achieved by varying the laser pulse duration or amplitude in correspondence with a received analog signal, while maintaining constant center-to-center hole spacing. Figures 1a and 1b are photographs of an individual machined hole and an assemblage of variable size holes defining an image of a human eye. (The pulse duty factor is typically a few percent, so that the beam is essentially stationary during the machining of each hole.) When the

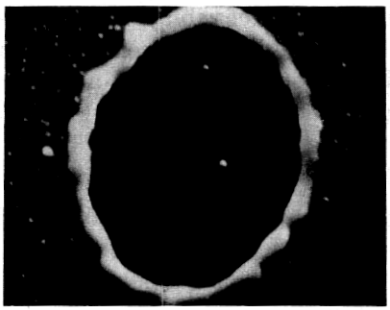

(a)

(b)

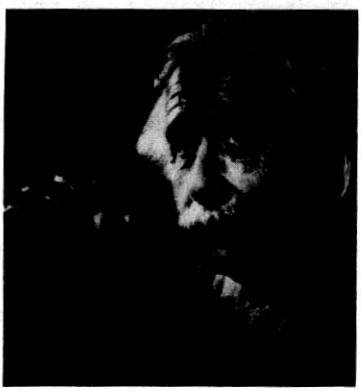

(c)

Fig. 1—Formation of microimages by hole machining with a cavity-dumped YAG laser. (a) An isolated 5-μm-diameter machined hole in Se/Bi film deposited on a plastic substrate. Most of the displaced metal is found in a thickened rim around the hole periphery. A few metal droplets remain in the hole, and some appear beyond it. (b) Microimage of a girl's eye. The center-to-center hole spacing is maintained constant. The hole sizes are varied to attain a gray-scale effect. This figure is an enlargement of a portion of an IEEE Test Chart. (c) The capabilities of the cavity-dumped YAG-laser machining printer for rendering detail and gray-scale tonality are illustrated by this microimage of Albert Einstein. The light vertical scratches were caused by a film manufacturing error.

image is projected onto a screen, the eye does not resolve individual holes at normal (25 cm) reading distance, so local regions machined at constant pulse energy appear to be uniformly bright, as indicated in Fig. 1c. (The images of Fig. 1 were made on Se/Bi film with a cavity-dumped YAG laser.)

The rectangular frame area, usually of 17/22 aspect ratio, has been defined by a mechanical raster scan in all machining printers built to date. The line scan (fast scan) is obtained by collimating the laser beam and deflecting it with a galvanometer mirror driven in sawtooth, oscillatory motion about the galvanometer axis. The mirror is centered in the entrance pupil of a writing lens which converts the beam angular deflections into displacements of the focused beam waist over a line in the flat focal plane. Hole machining occurs only during the line scan forward ramp. The galvanometer loaded resonant frequency, usually dominated by the deflecting mirror moment of inertia, dictates a minimum value for the sawtooth flyback time: it becomes difficult or impossible to provide acceptable ramp linearity if the scan rate exceeds about 40 percent of the loaded resonant frequency.[9] Frame widths up to 9 mm have been machined. (An exception to this flat-field method is described in Section 6.1.1.) The frame scan (slow scan) has been obtained either by translating the film past the fast-scanned line focus or by translating this line focus down the length of the stationary frame. Hesitation or jerkiness in the frame scan affects entire lines or groups of lines and produces prominent defects in the printed image. The smoothest scans are obtained by translating strongly tensioned film with a heavily damped capstan.

Because the film has a finite machining threshold and because lateral thermal conduction is negligible[3] in thin films, long, low-amplitude tails on the beam do not contribute to machining—i.e., the optical beams which machine adjacent holes may overlap greatly, but the machined holes need not. Discrete, contiguous machining sites are thereby defined, leading naturally to a capability for high resolution. Resolutions corresponding to 1600 holes per line are easily obtained and are typical of our printers. We find, however, that the optical numerical apertures needed to focus the GaAs machining beam exceed those which would be required if the beam obeyed the propagation law for Gaussian beams.[10] These large aperture requirements present an obstacle to the achievement of high printing speeds. Line scan rates of 166 Hz and pulse repetition rates of 330 kHz, corresponding to 12-s printing time for a 2000-line frame, have been obtained from GaAs laser printers without much difficulty, but appreciably higher scan rates require certain optical modifications, described in a later section. The fastest line scan rate attempted during our printer development was 500 Hz, corresponding to 4-s printing time for a 2000-line frame.

The scan linearity was barely acceptable even when flyback occupied approximately 30 percent of the line period, and successful hole machining required the use of a cavity-dumped gas laser at a pulse repetition rate of 1.0 MHz, producing only 1400 holes during the forward ramp. Attempts to print with GaAs lasers at 1.0-MHz pulse rate have so far been unrewarding; modifications in the laser structure, combined with thermoelectric cooling of the laser mounting stud, may be needed.

The beam emerging from the present GaAs laser is elliptical in cross section. It is also astigmatic: that is, when viewed in a plane normal to the p-n junction, the beam appears to diverge from the output mirror surface, but when viewed in the junction plane it appears to diverge from a point at least 25 μm deep within the laser.[11] All beam-acquisition lens systems, whether fiber-optical[12] or conventional,[13] must include one or more cylindrical elements which accurately remove this astigmatism. Unless this is done, machining, if it occurs at all, will take place with greatly reduced efficiency and very small depth of focus. By proper choice and placement,[12,13] these cylindrical elements can also correct beam ellipticity. This latter correction need not be particularly accurate since nearly round holes are machined at beam ellipticities as large as 2:1, provided the beam energy is not too far above machining threshold.

Astigmatism and ellipticity are easily remedied, but unfortunately the laser cavity design which produces these effects exhibits a more serious and intransigent beam defect. A low-amplitude, rather complicated, mode structure appears parallel to the junction plane at currents slightly above lasing threshold. The amplitudes of these modes usually increase, relative to the fundamental mode, as the current increases. At high currents as much as ⅓ to ½ of the total optical power is diverted into this secondary structure. This power contributes very little to raising the film temperature within the periphery of the main (machining) mode, and its presence represents a serious loss of machining efficiency. The problem is tolerable only because the Se/Bi film machining threshold is exceptionally low. The GaAs beam also evinces several lesser defects which, luckily, can be disposed of without seriously limiting the printer performance. The longevity of present lasers is probably adequate for commercial printing usage provided the average pulse repetition rate is restricted to keep the laser junction near room temperature.

Readers for whom the above general description of frame machining has provided sufficient detail may wish to turn to the final sections of this paper for examples of the image quality which has been attained in GaAs laser printers. The intervening sections describe the methods, problems, and design compromises used in producing those images.

III. THE GALLIUM-ARSENIDE MACHINING LASER

3.1 Machining requirements; epitaxial structure

The GaAlAs double heterostructure laser described next was developed around the needs of machined-image printing. The requirements on the laser evolved during this development, mainly in response to advances in the machining film technology. The present nominal requirement is a single-mirror output of 0.3-W peak pulse power in the fundamental cavity modes parallel and perpendicular to the junction plane, with 3-percent duty-factor capability at room temperature and median life corresponding to the machining of 10^4 to 10^5 frames. Junction-plane filamentation (strongly erratic beam-intensity variations along the junction plane) cannot be tolerated.

Figure 2 depicts the typical epitaxial structure[14] used in machining lasers and also illustrates the confinement of current to a 12-μm-wide stripe in the outermost epitaxial layers. The stripe is defined by masking the 12-μm width from 300-KeV proton bombardment which reduces electrical conductivity in the adjacent, penetrated regions.[15] Proper confinement decreases the total current which must be supplied at the laser threshold current density, and it also leads to gain profile variations which provide mode guidance parallel to the junction plane. The epitaxial layers are grown on a 100-μm-thick, n-type, GaAs substrate. The topmost layer is usually a GaAs, p-type, capping layer included primarily to assist contact formation and to reduce the propagation of contact strains into the recombination volume. This cap is sequentially metalized with layers of titanium, platinium, and gold, and the substrate with layers of tin, palladium, and gold. Individual laser chips are obtained from a wafer by cleaving into 375-μm lengths and sawing into 200-μm widths the cleaved surfaces defining the laser mirrors. The epitaxial side is indium-bonded to a copper stud, and the substrate is contacted by a thermal-compression-bonded gold wire.

3.2 Mode confinement perpendicular to junction plane

Double heterostructures fabricated by liquid phase epitaxy are among the most efficient room-temperature junction lasers. The energy bandgap and optical refractive index of $Ga_{1-x}Al_xAs$ depend on the aluminum fraction x. Epitaxial layer sequences with different x-values can be arranged to create optical potential wells which define radiation field confinement perpendicular to the junction plane. Simultaneously, this sequencing creates diffusion barriers at some layer interfaces which confine minority carriers to the optical well where most of them recombine radiatively. The optical cavity of a machining laser must be comparatively thick lest the output mirror peak loading approach the catastrophic damage limit,[16] but thick cavities tend to

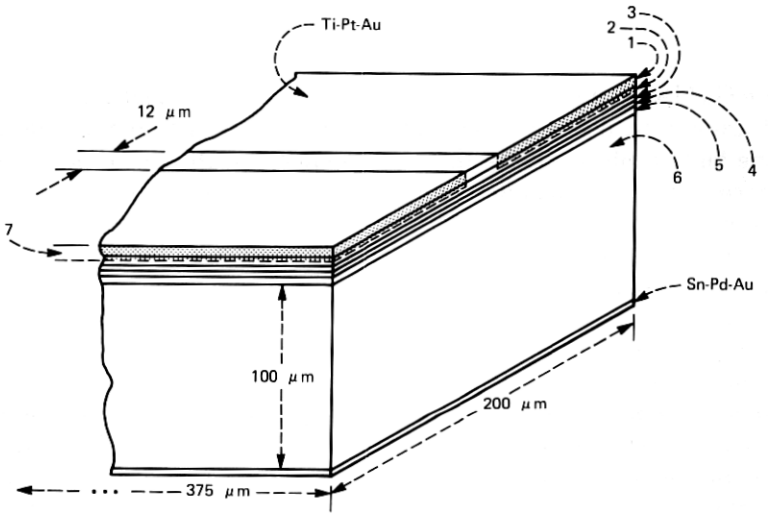

(a)

LAYER	DESCRIPTION	PRINCIPAL DOPING ELEMENT	THICKNESS
1	p-CAP, x=0	Ge	2 μm
2	P-TERNARY, x=0.24	Ge	2 μm
3	p-ACTIVE LAYER, x=0	Ge	1.3-1.6 μm
4	n-LOSS LAYER, x≃0.02	Te	0.8 μm
5	N-TERNARY, x=0.24	Te	2-3 μm
6	n-SUBSTRATE, x=0	Si	100 μm
7	REGION PENETRATED BY 300 keV PROTONS	–	~2.3 μm

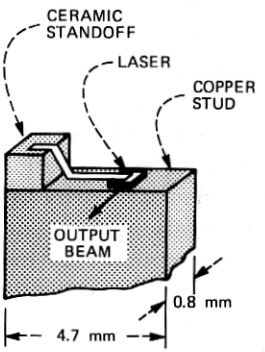

(b)

Fig. 2—Micrographics-laser structure and mounting. (a) Structure. The label x refers to the aluminum fraction in $Ga_{1-x}Al_xAs$. Five epitaxial layers are indicated. The topmost layer (p-cap) is included to facilitate bonding; however, it also increases the thermal resistance and has been omitted from some micrographics wafers. Proton bombardment penetrates only into the top of the $P_{0.24}$ region, as indicated by the dashed line, defining a 12-μm-wide x 375-μm-long conductive cross section. (b) Mounting. The laser is indium-bonded to a copper stud with the output mirror overhanging the edge of the stud by ~ 10 μm. The laser n-contact is wire-bonded to a gold-plated ceramic standoff. The epitaxial layers are overplated with a 10-μm-thick gold heat sink before indium bonding. The illustrated arrangement produces a steady-state temperature rise of 34°C per watt of electrical input power.

favor high-order modes over the fundamental mode. A distinctive feature of the present laser design is the selective introduction of optically lossy dopants[17] into the epitaxial growth sequence to suppress high-order modes.

Figure 3 illustrates the mode and carrier-confining mechanisms for typical refractive index and band-gap energy variations. Band-edge positions for the forward-biased junction are shown in Fig. 3b. Electrons are injected across the p-$n_{0.02}$ junction* by application of forward bias, and their diffusion in the p-region is limited by the large, nearly lossless, potential barrier at the p-$P_{0.24}$ boundary. Thus, carrier radiative recombination—the lasing power source—occurs almost exclusively within the p-region. The optical fields are confined within the $n_{0.02}$-layer and the p-layer by the large refractive-index discontinuities at the $N_{0.24}$-$n_{0.02}$ and $P_{0.24}$-p boundaries shown in Fig. 3c.

The technique[17] for maintaining fundamental mode operation with this thick optical cavity is indicated by Fig. 4, in which 0- and 1-order mode profiles have been superimposed on a cavity refractive-index plot. The small index discontinuity at the p-$n_{0.02}$ interface shifts the 0-order mode center preferentially toward the p-region where most of the gain-producing radiative recombination occurs. The same shift occurs for the 1-order mode, but since a larger volume is needed to accommodate this mode, most of one of its lobes remains in the tellurium-doped $n_{0.02}$-layer. Calculations[18] indicate that the high optical losses created by tellurium doping reduce the 1-order mode net gain below that of the 0-order mode. Hence this design should produce a large 0-order cavity volume compatibly with low threshold current. Both factors are important in achieving long laser life at high pulse powers and at room temperature.

3.3 Junction plane mode guidance

The previous section dealt with the use of real-refractive-index discontinuities to achieve mode confinement perpendicular to the junction plane. This method can provide fundamental mode operation so long as the confining layer thickness is less than about 1.6 μm. The high peak powers which must be produced by a machining laser require cavity cross sections of 15 to 20 μm^2 to keep the mirror loading[16] and lateral current crowding[19,20] within conservative limits. Therefore, if the cavity can be only 1.6 μm thick, it must be made at least 10 μm wide. Fundamental mode operation in this wide a cavity is not easily achieved with structurally defined, real-index discontinuities, although recent advances in real-index mode guidance have been encouraging (see Section 4.2.4). Lateral mode confinement in the present laser has been based on gradual variations in the imaginary part of the dielectric constant. A guidance mechanism of this type is illustrated in Fig. 5.

In Fig. 5a, the junction plane is the $x - z$ plane. A thick, high-

* Ternary layers are distinguished with capital letters, and an optional subscript denotes the aluminum fraction, x.

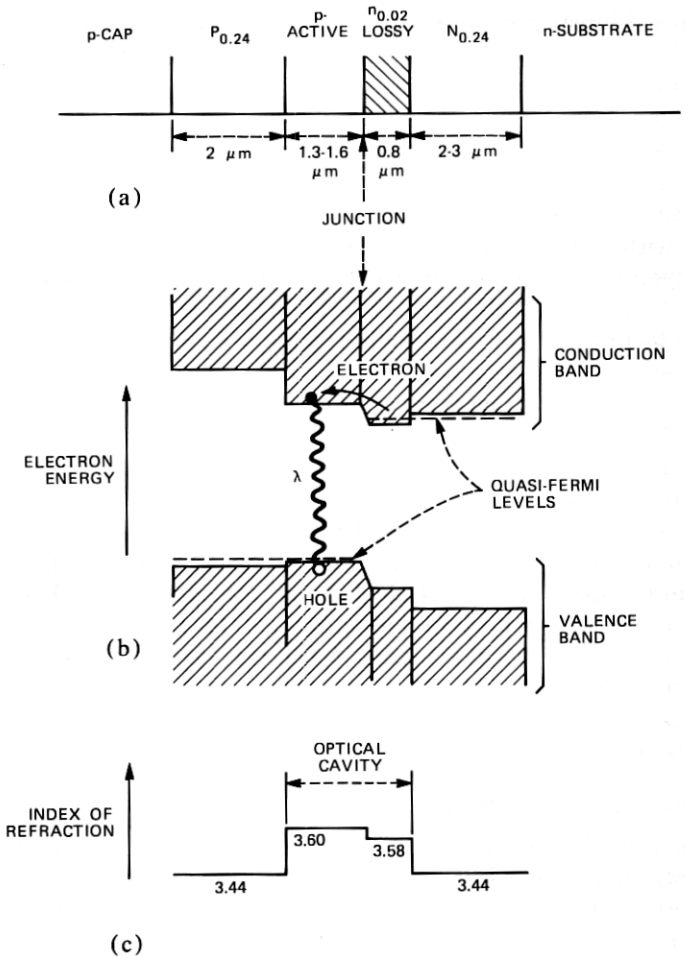

Fig. 3—Optical- and carrier-confinement mechanisms. (a) Epitaxial structure. Forward bias causes electrons to be injected across the $n_{0.02}$-p junction. (b) Carrier well. Electrons injected from the $n_{0.02}$-region into the p-region are transported toward the $P_{0.24}$-region by diffusion. At the p-$P_{0.24}$ boundary, they encounter a potential barrier whose height is large compared to the electron thermal energy, limiting radiative recombination between minority carriers (electrons) and majority carriers (holes) almost entirely to the p-region. (c) Optical well. Optical fields tend to remain confined in the regions of highest (real) refractive index (i.e., the p-active region) because of critical-angle reflections at boundaries with lower index layers. Thus, the optical and carrier wells overlap substantially.

conductivity, n-GaAs region is assumed to occupy the space $y \leq 0$. The lower conductivity, p-GaAs, active region extends from $y = 0$ to $y = d$, and a high conductivity P-$Ga_{1-x}Al_xAs$ region extends from $y = d$ to the external contact at $y = a$. Proton bombardment, penetrating partway into the P-layer, defines a contact width $2w = 12$ μm through which current flows. We assume that the proton-penetrated volume has zero

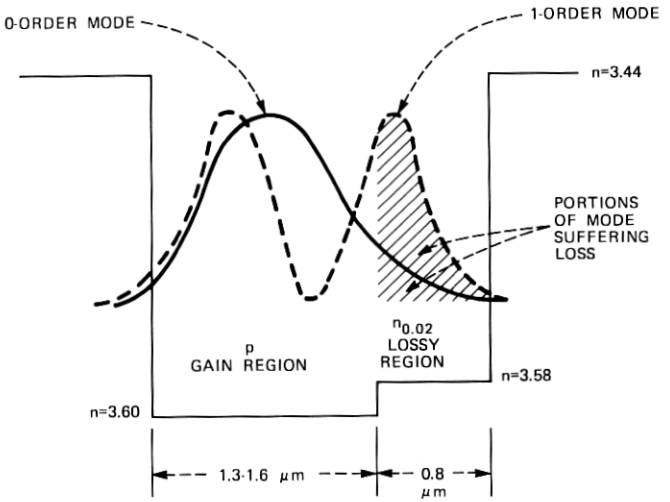

Fig. 4—Mode control perpendicular to junction plane by loss selectivity of optical modes. The $n_{0.02}$-layer is made optically lossy by heavy tellurium doping. A larger fraction of the undesired 1-order mode exists within this lossy region than is the case for the desired 0-order mode. By properly controlling the loss and the p- and $n_{0.02}$-layer thicknesses, the pulse-current threshold for 1-order lasing can be kept above the currents required for micrographics use.

conductivity. When forward bias is applied, electrons are injected across the junction into the p-layer where they move by ambipolar diffusion. Because of the 168-mV-high diffusion barrier at the p-P interface, the electrons are effectively trapped in the p-layer, and nearly all of them recombine there radiatively. Their diffusion is driven by the profile $J_y(x)$ of the junction current density. This current density is concentrated in an area beneath and slightly wider than the stripe, rather than being uniformly distributed over the junction, as would occur if the p-region conductivity were infinite. That is, the finite conductivity and lateral current density $J_x(x)$ within the p-region cause the junction forward bias to depend on x. The bias is largest at $x = 0$ and decreases with increasing $|x|$, effectively shutting off the junction at large $|x|$.

This combination of diffusion and junction-bias variation produces an electron density profile, and hence a laser gain profile, which is peaked at $x = 0$, as shown in Fig. 5b. The ability of gain peaking to guide modes is readily shown[21-23] by treating gain transparency by inclusion of a positive imaginary term in the complex dielectric constant. The modes predicted when the gain profile is approximated by a parabola are constant-curvature cylindrical wavefronts with Hermite-Gaussian intensity distributions centered about $x = 0$. The refraction of these wavefronts at the output mirror, illustrated in Fig. 5c, is responsible for the astigmatism in the beams emitted by stripe-

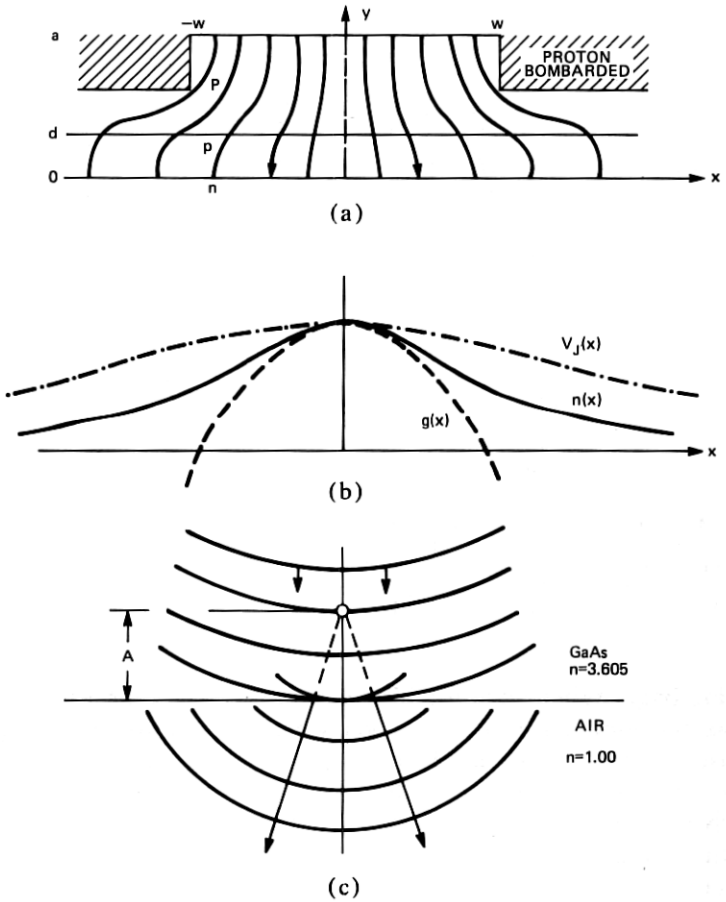

Fig. 5—Mode control parallel to junction plane. (a) Expected current-flow pattern in micrographics laser. (b) Proton bombardment and layer resistivity inhibit the lateral (i.e., x-directed) flow of current and cause the junction forward bias $V_J(x)$ to decrease with increasing $|x|$, confining junction current to the region $|x| \approx 1.5w - 2w$. The result is a bell-shaped minority-carrier profile $n(x)$ in the active region, which produces an approximately parabolic variation in optical gain $g(x)$. Ideally, this gain profile is centered symmetrically underneath the stripe. (c) The gain profile supports Hermite-Gaussian modes with constant-curvature wavefronts. This curvature produces astigmatism, since the cylindrical wavefront which is refracted into air at the GaAs-air interface appears to originate from a line focus located a distance A inside the laser.

geometry junction lasers. However, the electron density also changes the real part of the dielectric constant via several effects.[11] The sum of these effects is perhaps slightly anti-guiding,[11,24] but is too small to overcome[25] gain guidance. Some of these real-part effects could be nonsymmetric in x and could displace the mode center from $x = 0$. The retention of cubic (and higher odd-order) terms in approximating the gain profile also predicts a mode whose center is displaced from

$x = 0$. Whatever its physical origin, mode displacement does occur,[26–28] and it leads to degradations in the beam intensity profile which have serious consequences for machining.

The junction-plane behavior is sometimes unstable and erratic. This tendency appears to be correlated with high aluminum content in the ternary P-layer. Wafers with $x = 0.36$ have yielded very few stable machining lasers, whereas $x = 0.24$ wafers have produced many usable lasers. The difference may be related to the ternary electrical conductivity, which is about 10 times higher for $x = 0.24$ than for $x = 0.36$.

IV. DESCRIPTION OF LASER NEAR AND FAR FIELDS

4.1 The major beam defects

The electric-field-amplitude profile of the cylindrical beam waist at the output mirror determines[29] the divergence of rays perpendicular to the junction plane whereas, in the plane of the junction, the beam appears to diverge from a cylindrical waist located a short distance A behind the output mirror because of refraction of the constant-curvature wavefronts.[11] A simplified statement[13] of the printer optical function is that a cylindrical optical element(s) superimposes these two waists onto one another, and spherical elements image this superposition onto the metal film. A characterization of these waists prior to their superposition provides valuable information on the laser beam properties that create difficulties in machining images.

The most important beam defects are:

(*i*) Beam steering in the junction plane. The beam, viewed in the junction plane, emerges at an angle to the mirror normal, and this angle is current dependent.

(*ii*) A sidewise displacement of the junction-plane virtual waist toward one edge of the 12-μm-wide conductive stripe, accompanied by the appearance of side-lobe mode structure. At high currents, the side lobes contain an appreciable fraction of the total power, but contribute very little to hole machining.

(*iii*) Destabilization of the mode by optical feedback. Reflections from beam waists formed by optics external to the laser, e.g., from the metal film, are focused back into the laser cavity. This feedback is superimposed onto the internal feedback from the output mirror, and its phase fluctuates because of unavoidable microphonic, thermal, and convection effects, producing erratic power variations.

(*iv*) Current dependence of the astigmatism distance, A. The value of A increases with increasing current (i.e., the wavefront curvature decreases), and the various junction-plane mode components have differing A values.

The deleterious effects of items (*i*), (*iii*), and (*iv*) on this list can be rather easily remedied or reduced as described in the remainder of

Section IV. However, the avoidance of power loss into junction plane side lobes [item (*ii*)] is somewhat less certain, at least within the context of a fundamental-mode, high-duty-factor, long-lived laser.

4.2 Experimental evidence of beam defects; possible remedies

4.2.1 Beam steering

Beam steering is measured by mechanically scanning the laser emission profile parallel to the junction plane with a slit/photomultiplier arrangement. The plane of the slit can be spaced 2 to 3 cm from the laser mirror, and no optics are needed. The direction of the mirror normal can be determined accurately by reflecting a He-Ne laser beam from the cleaved facet. A family of such profiles is shown in Fig. 6 for an ascending sequence of currents in a selected laser. The structure which appears in the wings of these profiles at high currents indicates that junction-plane side lobes can propagate into the far field at angles different from the principal-ray angle of the main lobe. Below lasing threshold, the main-lobe profile peak is accurately located along the mirror normal but, as the current increases above threshold, the peak shifts monotonically away from the normal, the shift exceeding 8 degrees at high currents. The angular shifts θ_s and the profile angular full-widths at half-amplitude $(2\Delta\theta)_{1/2}$ are plotted in Fig. 7 as functions of current.

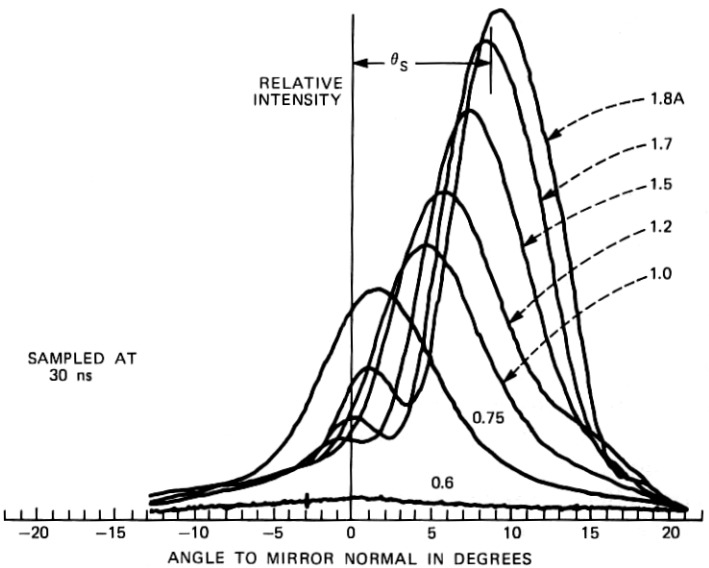

Fig. 6—Intensity angular distribution parallel to junction plane. The angular position of the peak of the far-field intensity distribution parallel to the junction plane defines the beam-steering angle, θ_s. Side-lobe structure in the intensity profiles becomes increasingly pronounced as the current is raised. The data were measured 30 ns after the beginning of a 100-ns-duration pulse.

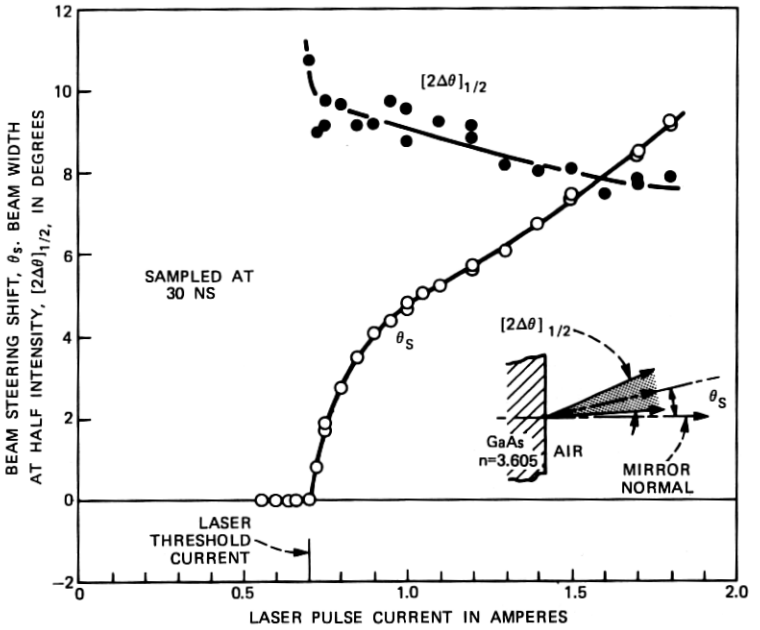

Fig. 7—Dependence on current of beam-steering angle and profile width parallel to junction plane. The far-field intensity full-width at half-maximum amplitude, $[2\Delta\theta]_{1/2}$, depends very little on current, whereas the beam-steering angle, θ_s, increases rapidly with current and actually exceeds $[2\Delta\theta]_{1/2}$ at high currents.

The immediate effect of beam steering is to increase the printer optical apertures needed to accommodate the junction-plane rays at all currents. This works no particular hardship until one reaches the galvanometer mirror. There the consequence of beam steering can be a sizable displacement of the collimated beam parallel to the laser junction plane. This displacement, for a collimated beam full-width at half-amplitude of $(2R)_{1/2}$, equals $[\theta_s/(2\Delta\theta)_{1/2}]\ (2R)_{1/2}$. As seen from Figs. 6 and 7, this quantity can actually exceed the collimated beam diameter. The net effect, if a large range of laser currents must be accommodated, is considerably to increase the galvanometer-mirror moment of inertia and the writing lens entrance-pupil diameter. The moment-of-inertia increase is smallest if the laser junction plane is oriented parallel to the galvanometer axis.

The increases in aperture size demanded by beam steering disappear if only one pulse-current level is used to print images. Time-sampled studies of junction-plane behavior show that the beam-steering angles in Figs. 6 and 7 are attained within 30 ns of the current pulse turn-on instant. Therefore, if the pulse machining energy is controlled by pulse-duration modulation (30 ns $\leq \Delta t \leq$ 100 ns) at constant pulse-current amplitude, rather than by current modulation at constant pulse dura-

tion ($\Delta t = 100$ ns), then beam-steering displacements will be constant and can easily be eliminated by mechanically biasing the laser.

Beam steering is small or absent from profiles scanned perpendicular to the junction plane. The normalized far-field profiles shown in Fig. 8 indicate that a slight ($\lesssim$2 degrees) shift may have occurred when the current in this laser was raised above threshold. (The illustrated data are chart recorder tracings, uncorrected for aperture inclinations.) The smooth, monotonically decreasing sides and tails of these profiles invite comparison with the junction-plane data of Fig. 6.

4.2.2 Mode displacement

Displacement of the junction-plane principal lobe towards the stripe edge is illustrated in Fig. 9. These profiles were obtained by scanning a ×43 magnified image of the laser output mirror, formed by a 0.68-NA microscope objective, parallel to the junction plane. The shift begins abruptly near laser threshold and proceeds rapidly with increasing current towards an asymptotic value equal to about 0.8 of the stripe half-width. In Fig. 9, one or more unresolved peaks is visible on the right of the higher current profiles, filling in the space left vacant by the shifted main-lobe peak. Mode displacement in itself does not cause important printing defects. But as a manifestation of secondary junction-plane mode structure, it is symptomatic of the rather serious defect which is elaborated on in Section 4.2.4. It has been established, by sampling the profiles at various instants within the 100-ns-long

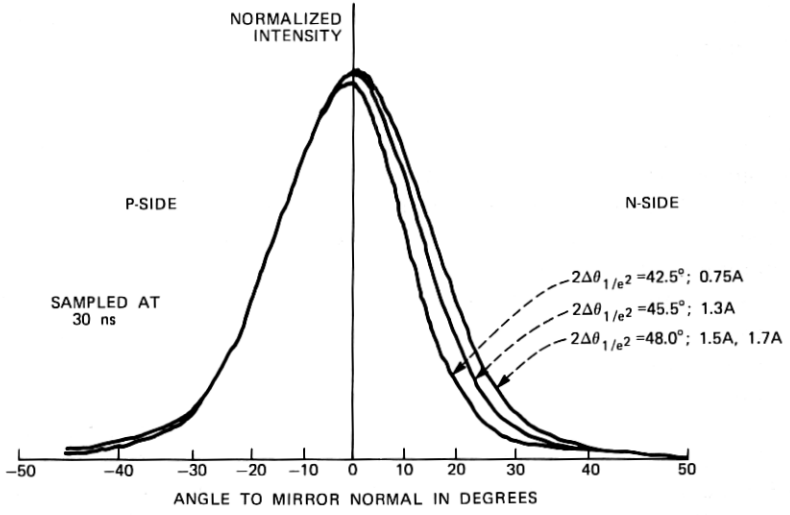

Fig. 8—Intensity angular distribution perpendicular to junction plane. The far-field intensity distribution normal to the junction plane shows evidence only of the 0-order mode. Its width increases slightly with increasing pulse current.

pulse, that mode displacement attains its final value somewhere within 10 to 30 ns of current-pulse turn-on.[28]

The width of the main peak can be roughly estimated by measuring the width of the left-hand half of the Fig. 9 profiles and assuming symmetry. This full width is current-independent at high currents, and its $1/e^2$-intensity value equals twice the stripe width. The same width is found for the spontaneous emission profiles well below threshold. The profiles are significantly narrower than this value only in the neighborhood of threshold.

4.2.3 Mode destabilization

The brass scanning slit used for the data of Fig. 9 was lined on both sides with diffusely reflecting black tape. When the tape was removed, erratic scans such as those illustrated in Fig. 10 were obtained. The shape of these profiles depended on the instant within the 100-ns pulse at which they were sampled, and their reproducibility was poor. If the slit is replaced by a piece of Se/Bi film and an attempt made to machine images with this beam, uncontrollable gradations in the machined hole sizes will appear on many portions of the film, and in some areas as many as half of the intended holes may be missing. Examples of such erratic machining behavior are presented in Section 8.3.

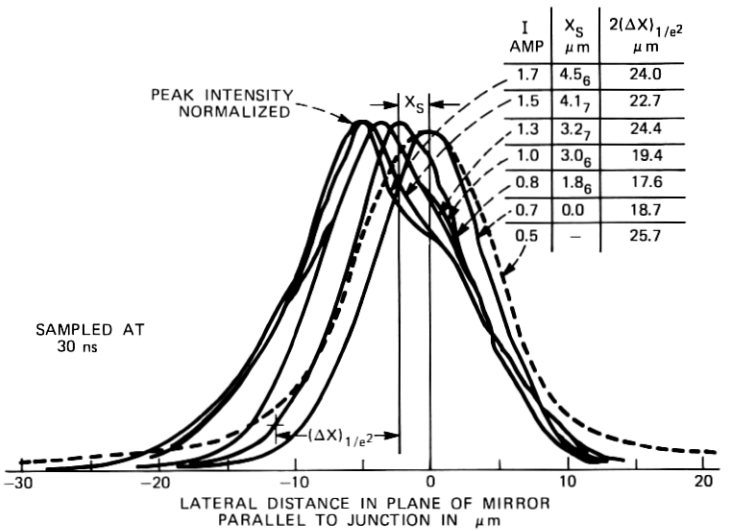

Fig. 9—Output-mirror intensity distribution parallel to junction plane. These mirror scans parallel to the junction plane show that the intensity peak shifts to the left by an amount x_s with increasing current; simultaneously, a shoulder appears on the right, indicative of multimode output. The values of $2(\Delta x)_{1/e^2}$ are estimates of the main lobe width.

The type of destabilization shown in Fig. 10 appears only on profiles taken at currents above laser threshold and is correlated with the laser output mirror reflectivity. The erratic machining which results is most serious with mirrors that have been antireflection-coated to forward-angle reflectivities smaller than 1 percent. The observations suggest that the laser cavity is being upset by time-dependent optical feedback. Light reflected from the neighborhood of a beam waist is refocused back onto the laser by the printer optics. This light re-enters the cavity and combines with the internal feedback from the mirror. The internal feedback is small if the mirror reflectivity is small, and the external feedback, whose phase and amplitude can vary slightly over the raster-scanned film, may be comparable to it in magnitude. Hence the observed destabilization consists of power overshoots and undershoots caused by pulse-to-pulse variations in the effective net feedback.

The likelihood of destabilization can be reduced by controlling the output-mirror reflectivity to guarantee the dominance of internal feedback in normal printing situations. The mirror coating designs used to accomplish this are summarized in Section 4.3.

4.2.4 Astigmatism and near-field side lobes

A virtual waist is produced inside the laser when the constant-curvature, junction-plane wavefronts are refracted[11] at the output mirror. Suppose that a 4-mm-focal-length microscope objective is positioned to form an image of the mirror at an appropriate conjugate distance, say, 180 mm. Then, as shown by the composite in Fig. 11 of

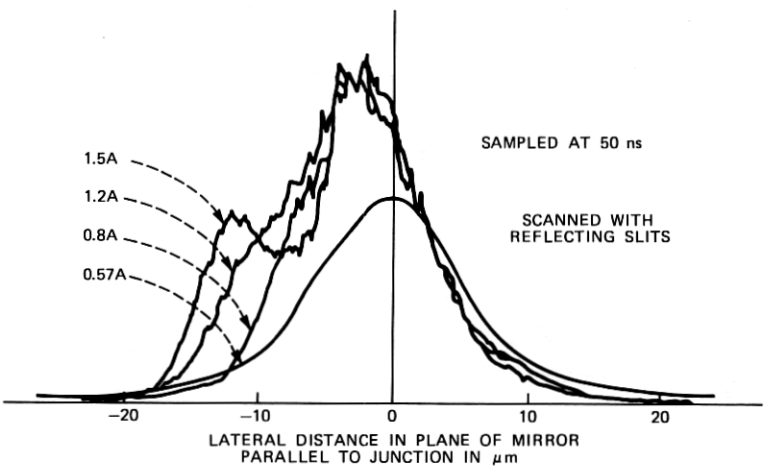

Fig. 10—Output-mirror scans parallel to junction plane, illustrating mode destabilization. Light reflected from the scanning slits and focussed back onto the laser output mirror destabilizes the laser cavity at currents above lasing threshold. There is no destabilizing effect below threshold.

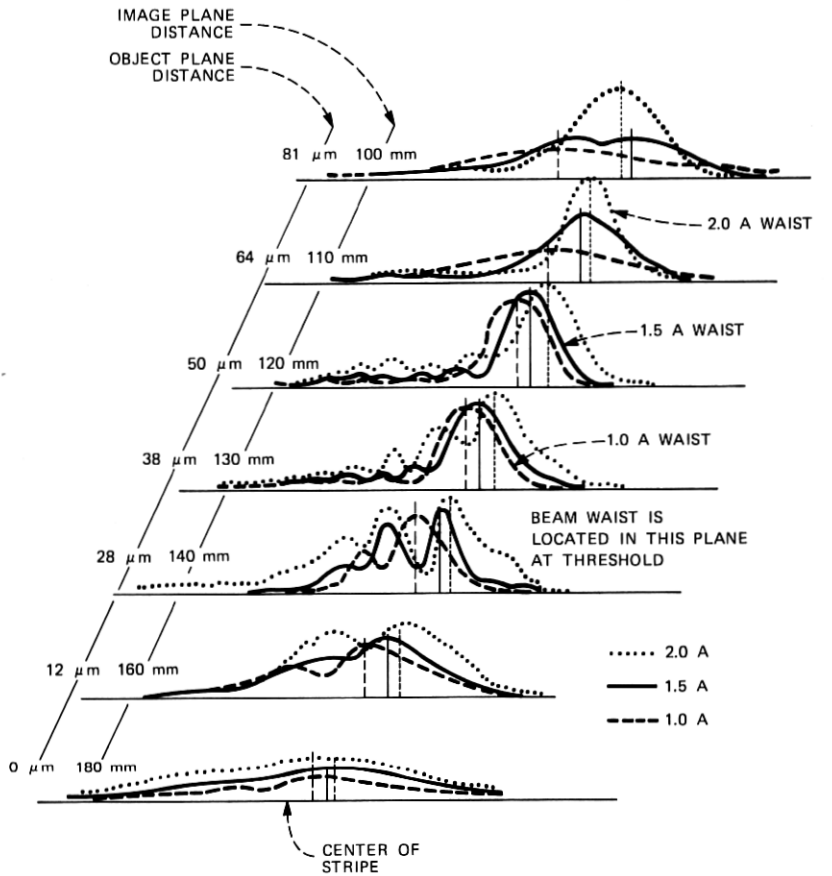

Fig. 11—Junction-plane profiles produced at various conjugate positions by beam-acquisition lens. A 4-mm-focal-length, 0.68-NA, microscope objective was used to focus an image of the laser output mirror at 180-mm distance from the mirror, and the intensity distributions parallel to the junction plane were measured at various intermediate planes between the lens and the 180-mm image position for several currents. The air-equivalent object distances within the laser, conjugate to these intermediate planes, are indicated. The plane at which the beam profile is narrowest, i.e., the astigmatism distance, depends on beam current. The astigmatism distance within the laser increases with current, corresponding to decreasing wavefront curvature of the junction-plane mode. Complicated multimode structure is evident throughout the focal region at machining current levels.

profile scans taken parallel to the junction plane, a real image of the junction-plane virtual waist will occur at some lesser, current-dependent, conjugate distance. At and below threshold this distance is, typically, about 140 mm; it decreases steadily as the current increases, approaching 110 mm at high machining currents. This change corresponds to an increase in the virtual-waist distance behind the mirror from 28 to 64 μm. The apparent width of this virtual waist has been approximated by applying the cylindrical-beam expansion law[30] to the

lower current mirror scans of Fig. 9, equating the appropriate astigmatism distances to the wavefront radii of curvature. Values of approximately 3.0 μm for the virtual-waist $1/e^2$-intensity full-width at high currents are obtained by this procedure.

Junction-plane profiles scanned at an axial distance of 125 mm for the laser of Fig. 11 and the mirror-emission profile scanned perpendicular to the junction plane at 180-mm axial distance are shown in Figs. 12a and 12b. The 125-mm plane was chosen to emphasize the strong side-lobe structure which accompanies the main lobe. If the image axial position is kept fixed and the current increased, the position of the main peak shifts laterally, and the side lobes build up and intrude into the main lobe. The loci of individual side lobes can be traced as functions of axial position in the image field with the aid of Fig. 11. One sees that the narrowest width of a given side lobe occurs in an image plane different from that of the main lobe and of other side lobes, and that the steering angle of its principal ray is similarly unique, a fact already known from Fig. 6.

Care must be taken that the above description does not mislead. A real "image" in Figs. 11 or 12a derives its identity from being the position in the image field at which the main junction-plane lobe appears to be narrowest. The virtual waist within the laser is the conjugate of this image as demagnified by the microscope objective. However, it must be kept in mind that the illustrated lobe structure in no sense depicts the shape of cavity traveling-wave modes. (The intensity distributions of these modes should be correctly illustrated by the mirror scans of Fig. 9.) The scans of Figs. 11 and 12 represent the response of the microscope objective (and the detecting photomultiplier) to both phase and amplitude at the mirror, in accordance with the Kirchoff-Huygens formulation.[10] The actual phase variation at the mirror parallel to the junction plane becomes more complicated than square-law at high currents and produces the secondary-lobe intensities found in the lens image plane.

As mentioned in Section 4.1, the final beam waist at the machining film is a cylindrically corrected superposition of a junction-plane profile (such as those in Fig. 12a) and of the mirror-emission profile viewed perpendicular to the junction plane (as in Fig. 12b). The dependence of the main-lobe astigmatism distance on current[11,30] causes the machining-waist diameter also to depend on current. This can complicate the rendition of gray scales when images are printed by pulse-amplitude modulation. However, since time-sampled profile measurements show that the mode structure is established within 30 ns of the pulse turn-on time, the use of pulse-duration modulation, as discussed in Section 4.2.1, should eliminate astigmatism current-dependence as a potential problem.

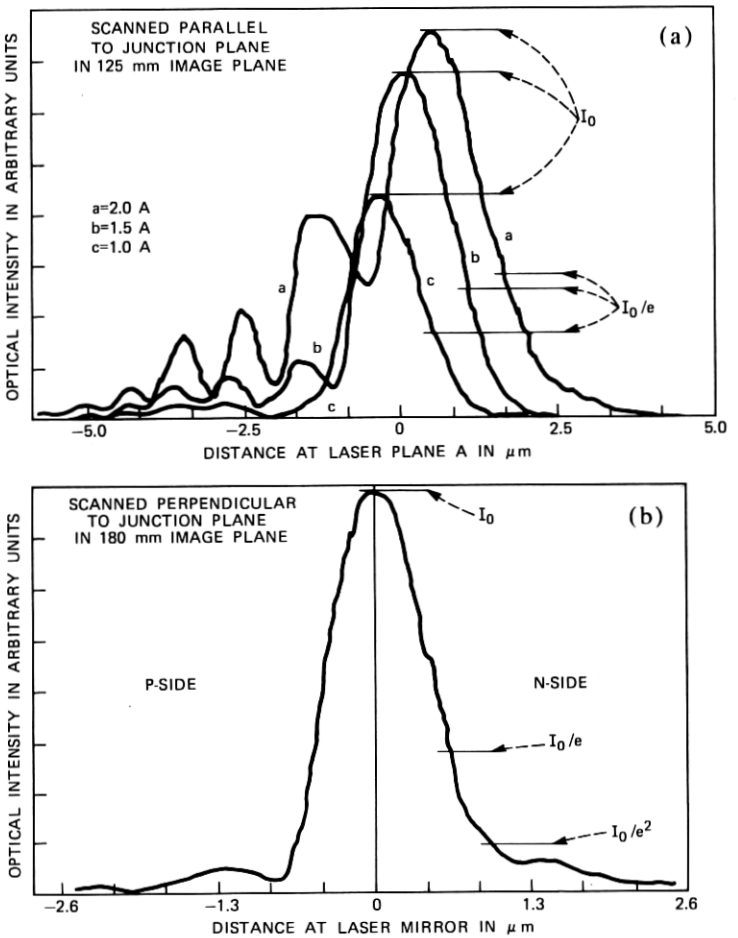

Fig. 12—Intensity profiles in image planes of beam-acquisition lens. (a) At 1.5 A, the profile scanned parallel to the junction is narrowest in the 125-mm image plane. As the current is varied above and below this value, the secondary-lobe structure at 125 mm varies rapidly. All the secondary-lobe peak intensities are below machining threshold, except for the largest secondary lobe at 2.0 A. (b) The 4-mm-focal-length, 0.68-NA, microscope objective focuses the laser output mirror at 180-mm image distance. Profile scans perpendicular to the junction plane at 180 mm are essentially independent of current; the profile full width at $1/e^2$ of peak intensity is 1.50 μm, comparable to the p-region width.

The presence of secondary junction-plane modes* in the machining waist is a different matter. At machining current levels, these lobes

* The permanence of the lobe structure, the regularity of the lobe spacings, and the apparent interrelatedness of their amplitudes are evidence that the structure represents higher-order, guided, junction-plane modes rather than independent lasing filaments. Filamenting, when it occurs, usually involves violent and erratic beam displacements and beam steering within the 100-ns-duration pulse, which bar use of the laser for image printing.

can carry an appreciable fraction of the beam power, yet their individual amplitudes are insufficient to machine (nor would it be desirable to have them machine). Typically, they are strung out asymmetrically on one side of the main (machining) lobe, and because lateral thermal conduction is very small in the film being machined, they contribute little to the attainment of machining threshold within the main lobe. The loss of machining efficiency implied by their existence is a serious defect of the present laser design, which relies on gain guidance to control the junction plane modes. The side-lobe amplitudes could be reduced optically only by non-square-law, cylindrical, phase corrections which, even if physically realizable, would be *ad hoc* with each laser. Practical control of the mode displacement that permits the secondary lobes to arise requires further laser design effort. (The GaAs machining lasers used in video disk recording also utilize gain guidance but operate at much lower powers than in the present application; acceptable junction plane mode control is obtained by narrowing the proton bombardment stripe to 5 μm.[31])

Real-refractive index guidance in the junction plane can be provided by burying the laser active p-region in ternary layers of lower refractive index. By controlling the index differences and the active region width in these buried-stripe heterostructure devices, lowest-order transverse-mode operation parallel to the junction plane has recently been obtained[32] at pulse currents up to nine times lasing threshold. At this level, had the laser been antireflection-coated, the pulsed output power would have been enough to machine Se/Bi film. Astigmatism is absent with real index guidance, and it appears that buried-stripe heterostructures can be designed to yield near-field ellipticities smaller than 3:1. Hence, cylindrical optical corrections may not be needed. Whether the buried-stripe geometry would present more severe thermal limitations at printing duty cycles than the proton-delineated stripe geometry is unknown, but this approach to junction plane mode control certainly merits consideration in future studies of GaAs machining lasers.

4.3 Laser antireflectance coatings

Antireflection coatings are needed on the laser output mirror for a variety of practical reasons, the most important from an image-printing standpoint being laser longevity. Such coatings can double the output-mirror differential quantum efficiency, furnishing machining-level powers at significantly reduced pulse currents; they can suppress higher-order modes and improve power stability, increasing the device yield of thick-cavity wafers; and they can protect the output-mirror facet against harsh chemicals and abrasion. Although refractory coatings are available which can reduce facet reflectivity to values smaller

than 0.1 percent, the resultant laser would be highly sensitive to the mode-destabilization effect explained in Section 4.2.3. In practice, the coating small-angle reflectivity must be controlled carefully.

Antireflectance coatings usually broaden the laser longitudinal mode spectrum and increase the optical bandwidth that must be chromatically corrected. Hence, their use in high-optical-resolution applications can have the economic drawback of requiring expensive glasses in lens fabrication. The objection is not trivial since the cost of fabricating diffraction-limited printer optics could become prohibitive unless design simplifications of this type were possible.

The antireflection coatings presently used on printing lasers are: (*i*) single-layer films of ZrO_2 deposited on the output mirror in optical thickness of approximately one-quarter or three-quarter wavelength and (*ii*) bilayer films consisting of ZrO_2 overcoated with Al_2O_3. These refractory oxides are deposited by electron-gun evaporation at $\sim 10^{-5}$ Torr of O_2 partial pressure. The measured ZrO_2-film refractive index is 1.92, and the Al_2O_3-film index is 1.63, at 0.885-μm wavelength.

The refractive index of ZrO_2 is a close antireflection match to the value 3.605 of the refractive index of binary GaAs, and ZrO_2 films can reduce the forward angle reflectivity to values smaller than 0.1 percent when deposited in exact odd-quarter-wavelength optical thicknesses. Unfortunately, its index is not sufficiently larger than the Al_2O_3 index to permit much exploitation of bilayer design possibilities. Higher index materials such as ZnS and TiO_2 are well known. However, the ZnS/Al_2O_3 bilayers are found to suffer from limited room-ambient shelf life, and the high substrate temperatures needed to make thin TiO_2 films in rutile form are a deterrent.

Properly fabricated coatings can greatly assist in achieving exclusive fundamental-mode output from thick cavities; namely, they can provide an assigned small-angle reflectivity together with deep reflection minima in both polarizations[33] at a specified large angle. Both polarizations must be accounted for, since the laser output is usually of mixed polarization at machining power levels. In Fig. 13, we have superposed the angular distributions of 0- and 1-order modes* measured for a particular laser onto the Fresnel-reflectivity angular dependences of a ZrO_2/Al_2O_3-bilayer design to illustrate that reflection losses can be made significantly larger for the 1-order than for the 0-order mode. Discrimination between the 0- and 1-order modes would clearly be largest if coatings whose reflection minima occur near the 1-order mode maximum could fabricated. Unfortunately, with our lim-

* Reflection-loss angular dependence discriminates only between modes perpendicular to the junction plane. The junction-plane modes have comparatively narrow angular distributions which are sensitive only to the reflectance values at forward angles. Those values are asymptotically independent of angle.

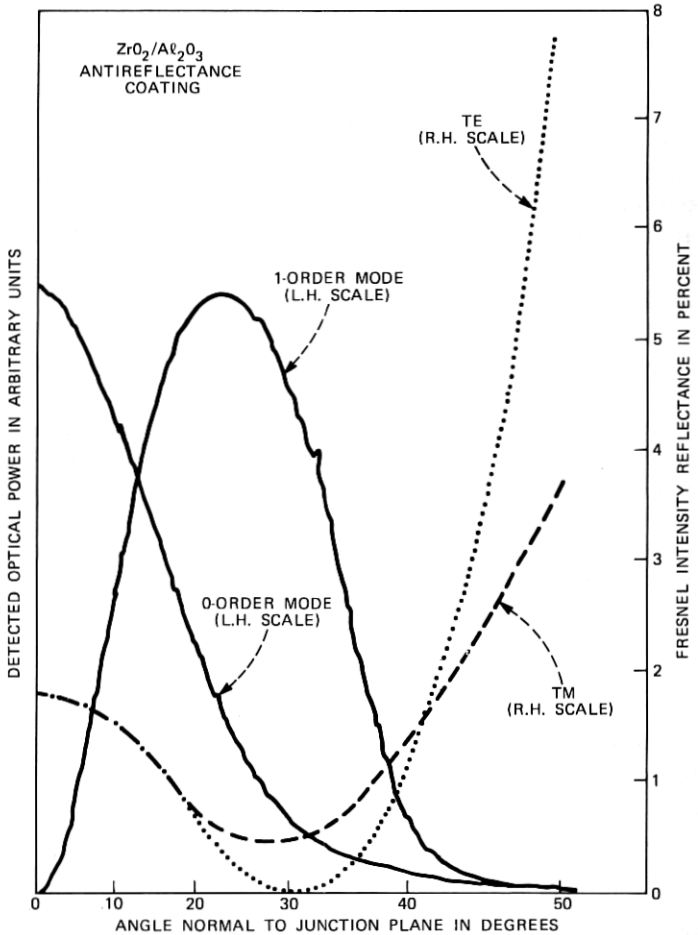

Fig. 13—Mode discrimination perpendicular to junction plane by output-mirror antireflection coating. The antireflectance design is chosen to produce minima in the TE and TM Fresnel reflectivities at angles as close as feasible to the maximum in the 1-order mode intensity. The necessity of maintaining at least a 2-percent small-angle reflectivity value (to inhibit mode destabilization by reflections from the micrographics film) makes it difficult to secure exact overlap between the Fresnel-reflectivity minima and the mode-intensity maximum, but rough approximations to this condition are sufficient to produce significantly higher mirror losses for the 1-order mode than for the 0-order mode.

ited selection of refractory coating materials, reflectivity minima at angles below 25 degrees are predicted only for designs whose 0-degree reflectivity is smaller than 0.7 percent, a situation very susceptible to external-reflection-induced destabilization.

Nevertheless, valuable amounts of mode discrimination can be obtained with the present coatings. Fresnel-reflectance measurements on

a selection of coated output mirrors show that our single-layer and bilayer films produce reflection minima for both polarizations in the range 25 to 40 degrees, with 0-degree reflectivities ranging from 2 to 6 percent. These measured Fresnel-reflectivity angular distributions have been multiplied by the mode angular distributions of Fig. 13 and integrated over angle to obtain *mode reflectivities*,[34-36] and hence comparative mirror losses, for the 0- and 1-order modes. The loss discriminations so computed significantly favor 0-order over 1-order oscillation and are compatible in detail with the switching of numerous lasers from oscillation in the 1-order mode (or in a mixture of 0- and 1-order modes) prior to coating to the 0-order mode exclusively after coating. (The 0-order device yield increased from 50 to 83 percent on one thick-cavity wafer.)

An antireflection coating applied to the front mirror increases its differential quantum efficiency and reduces that of the rear mirror, as shown by the laser output characteristics in Fig. 14. These coatings increase the laser threshold current slightly, but allow machining powers to be reached at significantly reduced currents and, more importantly, at lower peak values of laser internal circulating power.[37,38]

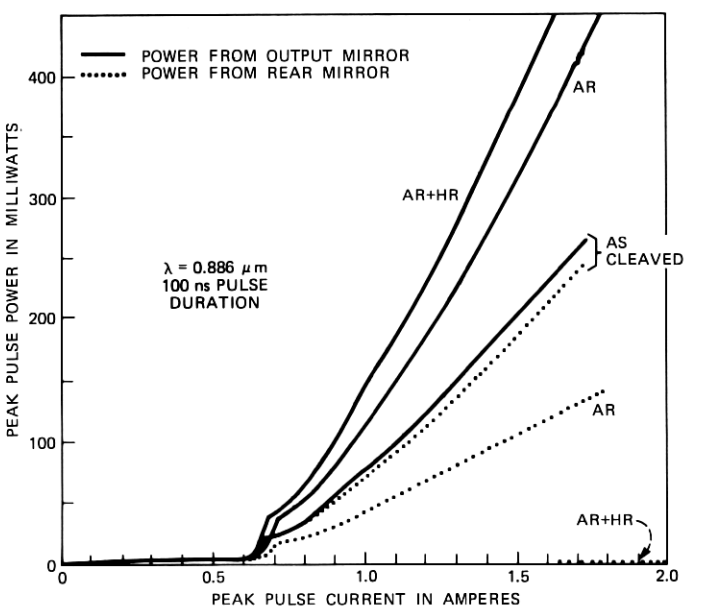

Fig. 14—Effect of mirror reflectance coatings on laser output power. The output- and rear-mirror powers in milliwatts are shown for: (a) The as-cleaved, uncoated mirrors. (b) Antireflection-coated output mirror and uncoated rear mirror, *AR*. (c) Antireflection-coated output mirror and high-reflectance-coated rear mirror, *AR* + *HR*. The increase in threshold current caused by *AR*-coating the output mirror is reduced when an *HR* coating is applied to the rear mirror.

If the rear mirror is now coated with a high reflector (a one-half wavelength optical thickness of ZrO_2, overcoated with aluminum), the threshold current approaches the as-cleaved mirror value, and the front-mirror output power at constant current increases further. This combination of coatings increased the front-mirror differential efficiency by a factor of 2.3 relative to its uncoated value, as determined by averaging over many lasers.

4.4 Laser longevity

End-of-life in thick-cavity, printing lasers has occurred from adverse changes in output mode structure and from a gradual loss of mode stability against external-reflection-feedback, as well as from diminished output power. Only the first and last aging symptoms have been investigated quantitatively, and these only on devices from one wafer. Gradual cavity destabilization has been seen on ZnS/Al_2O_3-coated lasers operated in room ambient; but it is absent, so far, from ZrO_2- and ZrO_2/Al_2O_3-coated devices.

4.4.1 Median life and failure symptoms

Antireflection-coated lasers from one wafer were pulse-current aged at 5 or 10-percent duty factors and at 20°C (time-averaged) junction temperature. The output mirror coatings represented various ZrO_2- and ZrO_2/Al_2O_3-evaporation runs. The rear mirrors of some lasers were high-reflectance coated, producing 20 to 30 percent higher internal optical powers at the output mirrors of these lasers than in the remaining aged devices. The median life against total power failure was 3×10^{11} pulses ($\sigma = 3.45$) independent of duty cycle, with the failure rate of high-reflectance-coated lasers being significantly greater than the average failure rate. Aging produced both favorable and adverse changes in machining performance of the survivors. Specifically, the difference between machining and lasing threshold currents, which is affected by details of the focussed beam profile and hence is sensitive to mode degradation, was—on the average—unchanged among survivors.

Failure was uncorrelated with the post-aging appearance of the mirrors, and mirror erosion was detectable on only two of the aged devices. However, the ratio of output-mirror to rear-mirror power was decreased among survivors, indicating that reduced net transmission of aged, coated mirrors (relative to as-cleaved mirrors subjected to somewhat lower optical power densities) had occurred despite the absence of visible damage. Scanning-electron-microscope examination of several failed lasers, using the electron-bombardment-induced recombination current at various primary energies, suggested that the devices had been damaged over as much as 75 percent of the device

length, with the damage originating at or near the output mirror. (The power loading of these mirrors is less than ⅛ the catastrophic damage limit reported[37] for similarly constructed lasers.) An increase of at least 40 mV in junction voltage and a softening of the laser V-I characteristic were observed in nearly all failed or severely degraded lasers, but were absent in healthy survivors.

4.4.2 Duty-factor limitation

Although a commercially feasible life* against power decrease, mode degradation, and mode destabilization seems established (at 20°C junction temperature) for the above devices, the data do not establish that satisfactory images can be machined at the 5 and 10-percent duty factors used in the aging tests. Attempts to machine images at 10-percent duty factor produced unintended hole size decreases from beginning to end of long machined lines, even though the junction was held at a time-averaged temperature of 20°C. The thermal relaxation time of 150 ns estimated for the laser active region is apparently not short enough to prevent a gradual build-up of junction temperature during the machining of many contiguous holes at 1-MHz repetition rate.[39] The build-up raises the laser threshold current and therefore lowers the machining power available for a given pulsed-current amplitude and duration. It is not known whether a significant reduction in the relaxation time could be obtained by redesigning p-cap and $P_{0.24}$-epitaxial thicknesses without degrading the already marginal junction-plane mode stability.

V. THE FILM SYSTEM

The laser machining performance of many *single-element* metal films, as fabricated by evaporation, sputtering, or electrodeposition onto a transparent substrate, has been investigated with high-pulse-power, cavity-dumped lasers. However, single-element metal films are found to be fundamentally limited in their ability to absorb light. In thicknesses which produce acceptable "black-white" contrast ratios at visible wavelengths, none achieves low enough machining threshold to serve satisfactorily with the present GaAs laser. Also, the long-term chemical stability—and hence the machining reproducibility—is poor for low-melting-temperature metals in oxidizing environments, limiting the room-ambient storage life of unused film.

Because of this unsatisfactory single-metal performance, a search for lower machining energies and improved chemical stability has been made among multiconstituent films. Over 70 film systems, including

* The median life of 3×10^{11} pulses is sufficient to machine about 90,000 all-white frames, and probably more than 500,000 negative-image frames.

eutectics, alloys, and metal-dielectric combinations, have been investigated. These were chosen primarily, but not exclusively, from low-melting-point elements. Antireflective combinations which might improve the film chemical stability while increasing its optical absorptance have been of special interest. The compositions were studied for machining performance as functions of laser power, for storage life (i.e., oxidation resistance) as determined by changes in optical transmission and machined hole size, for scratch resistance, and for adhesion. The next sections identify some of the chemical and physical attributes believed to affect hole formation in unoxidized and partially oxidized thin films, and attempt to justify the selection of a Se/Bi composition as a practical metal-dielectric film for facsimile image machining with pulsed GaAs lasers.

5.1 Hole machining in thin metal films

5.1.1 General description; hole-nucleation hypotheses

A machined hole represents the permanent rearrangement of film material in response to a localized temperature pulse exceeding a threshold temperature.* The final state consists of a debris pattern—typically, thickened peripheral rims (viz., Fig. 1a) accompanied by congealed metal droplets—whose surface energy is smaller than that of the unruptured film but whose optical transmission is much higher. Heat is absorbed from the focused laser beam in unruptured film areas and is radially redistributed via the debris pattern. Very nearly all the absorbed heat is eventually lost to the substrate by laminar conduction.

A free liquid surface is required for hole enlargement. The kinetic energy of the molten constituents as they recede towards the solid boundary or are flung slightly beyond it is usually attributed[40] to the surface energy decrease. Debris is ejected from the film surface at high power densities, possibly with the assistance of pressure from entrapped gases. During raster-scanned laser machining of large-area background "whites," these ejecta are evolved from the film in numbers sufficient to form a highly visible plume whose density is a convenient indicator for optimizing the machining beam focus. Redeposition of these "tektites" onto the film can degrade the image (viz., Sec. 8.3 and Fig. 46b) and must be kept under control. The avoidance of machining "splatter" and the production of clean holes with uniform rims are central problems[7,41] in attaining broadcast-quality signal-to-noise ratios with reflection-readout video disks.

The thickness of a film and the severity of its oxidation strongly

* Holes can also be opened by the repeated application of subthreshold pulses. At a low duty factor, approximately 16 pulses, each containing about 20 percent less energy than the threshold energy for one pulse, were needed to open a hole in 540Å-thick bismuth film.

affect the laser pulse energy needed to nucleate and enlarge a hole. The film-substrate interface also affects hole-opening dynamics via the interfacial surface energy and thermal impedance. Studies of hole-opening kinematics by a finely focused, very-low-power, laser probe beam, incident onto a surface-oxidized, 350 Å-thick bismuth film simultaneously and collinearly with the machining beam, showed that at powers just above machining threshold a hole tends to nucleate after the end of the laser pulse and, at powers five or six times larger than threshold, holes start to open before the end of the pulse, but at powers between these extremes, most holes nucleate near the end of the laser machining pulse. The occurrence of hole nucleation slightly before, or at, the end of the machining pulse is also compatible with an independent experiment on a 1200Å-thick composite film in which close agreement of machined hole areas with the predictions of laminar heat flow theory was obtained (viz., Sec. 5.3).

Hole nucleation in very thin films ($\leq$250Å of bismuth) is generally agreed to originate at pinholes and to involve a reduction in surface energy by local balling up of the metal into numerous droplets. In thicker films, however, the physical causes of hole nucleation are speculative. Figure 15 presents evidence for two hypotheses. Figure 15a shows the onset of hole opening in 540Å-thick, pinhole-free, bismuth film, apparently occurring at a multiplicity of sites in the neighborhood of, but not immediately beneath, beam center. This observation supports a hypothesis of hole nucleation in thick films involving changes in surface-tension gradients[42,43] during the transition from heating to cooling the film. (The radial temperature gradient is zero at beam center.) The photographic sequence in Fig. 15b of holes opened in an unoxidized Ni-P film at successively larger laser powers further illustrates this hypothesis. Secondary electron micrographs of thick films irradiated at energies just below machining threshold sometimes show circular blisters of metal lifted from the substrate, as in Fig. 15c. Blistering has been attributed to pressure from gas evolved from the heated substrate and trapped between it and the metal film, or alternatively to buckling of the film due to thermal expansion of the heated area. In either case, it is hypothesized that nucleation proceeds by rupture of the blister. Further evidence for buckling or loosening of film from the substrate is seen in the wrinkling of the irradiated area in Fig. 15d.

Freezeback of molten material begins when the pulse ends, and a solidification front propagates inwardly[44] towards beam center, terminating the outward displacement of molten material and defining the final hole diameter. The relevant freezing temperature may be the melting temperature of the metal or of a mechanically stiff oxide; in some volume-oxidized films, it may approach the metal boiling tem-

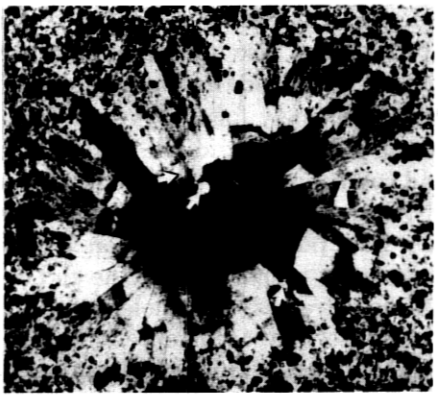

(a)

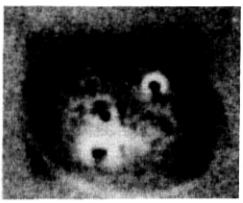

(b)

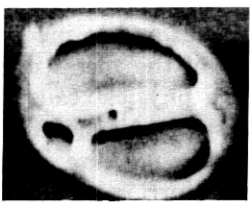

(b′)

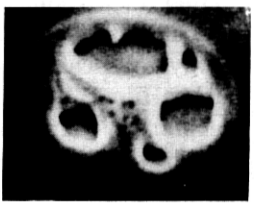

(b″)

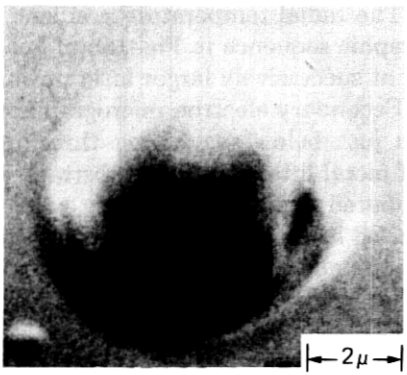

(c)

(d)

Fig. 15—Evidence for hole-nucleation hypotheses. (a) Transmission electron micrograph of 540Å-thick, free-standing, Bi film irradiated just at machining threshold. Three very small holes near, but not beneath, beam center are indicated by arrows. (b) to (b″) Three areas in NiP film irradiated at successively higher powers. (c) A blistered area in NiP film irradiated below machining threshold. (d) Hole in 400Å-thick Bi film. Wrinkled annulus surrounding lip of the hole suggests that film may have lifted from substrate prior to hole nucleation.

perature. Thus, the hole is circumscribed by an annulus of resolidified film material whose outer diameter may be only slightly larger than the machined hole diameter if the film oxide structure is fragile, but which can be considerably larger than the hole diameter if the oxide structure is strong (particularly for holes machined close to threshold).

5.1.2 Experimental description of laser-machined holes; hole-enlargement hypothesis

The sizes of holes machined by pulsed laser beams in thin metal films, and the patterns of the resulting debris, depend on the film thickness, the machining pulse intensity and duration, and the extent of film oxidation (film age). Figure 16 is a montage of scanning electron

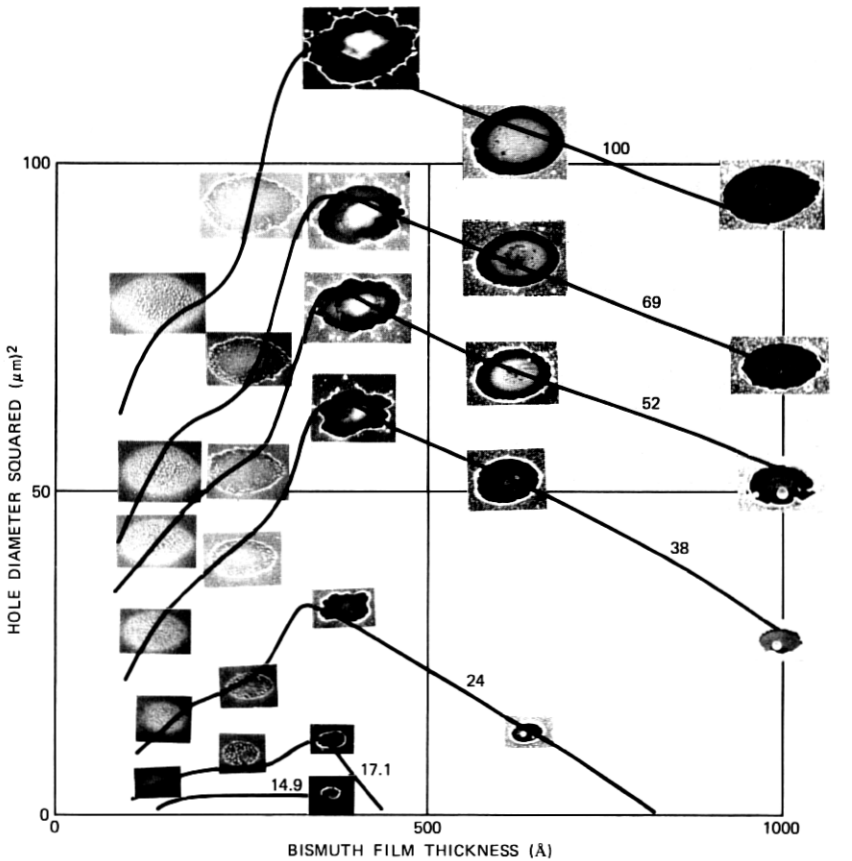

Fig. 16—Size and appearance of holes machined in bismuth films of various thickness, with laser pulse energy as a parameter. The curves connect data obtained at the same laser pulse energy and are labeled by the energy value as a percentage of 120×10^{-9} joules (corresponding to 4.0-W peak power at the measured 30-ns duration of the cavity-dumped YAG-laser pulse). See text for discussion.

micrographs showing the holes machined in evaporated bismuth films of various thicknesses by 30-ns-duration laser pulses of variable intensity. The focused beam diameter was 6.8 μm at 1/e intensity. These data reveal the following:

(*i*) The hole areas are maximized in the neighborhood of 350 to 400 Å film thickness. The debris in 400 Å-thick film machined at low intensities congeals into a raised lip surrounding the hole, and at high intensities into a characteristic pattern of balled-up metal droplets flung out beyond the lip. This type of splatter has been attributed[7] to the relatively low viscosity of molten bismuth. The photographs in Fig. 16 support the generalization that droplet size is an increasing function of film thickness.

(*ii*) Machining efficiencies diminish rapidly as the film thickness is decreased below 350Å. This thickness is coincident with the value below which the continuity of bismuth film is poor,[45] resulting in a proliferation of pinholes throughout the finished film. The debris pattern consists of droplets remaining within the hole; for the thinnest film, the metal droplets do not appear to have moved outwardly at all.

(*iii*) As the film thickness is increased above 400 Å, the hole areas machined at given power decrease inversely with thickness (viz. also Fig. 19). The debris from holes machined close to threshold consists of one large droplet lying within a thick peripheral rim. At high powers, the droplets lie outside the hole, and the rim thickness is nonuniform.

Figure 17 provides a more detailed look at hole opening in "optimally-thick" bismuth films. Holes of incomplete circumference (viz. Figs. 17a and 17b) have been formed by scanning the machining beam along a line making a shallow angle with a sharply defined edge in 400 Å-thick film. Their debris patterns are similar to those from nearly complete (Fig. 17c) or complete (Fig. 17d) holes, in that the rims of the holes are formed into *azimuthally discrete segments*. The number of segments increases with hole size, but the average segment length is roughly constant. Regularly spaced metal droplets of approximately constant size either congeal out directly onto the peripheral lip (Fig. 17d) or are flung radially beyond it, often remaining attached by a thin thread. Sometimes the thread breaks, producing detached, comet-like droplets.

The regularity of the azimuthal patterns in Fig. 17 tends to invalidate a "brush-fire" hole enlargement model (such as might be kindled by the 250Å data of Fig. 16) in which the melt surrounding one or more hole nucleation sites contracts into independent droplets which random-walk over the film surface and disappear by consolidating into a cooler rim. Figures 1a and 17 hint instead at a propensity of *peripheral* material in thicker films to form beads, implying that the rim is the source of droplets rather than the reverse. The rim of an expanding

hole is "superheated" since it contains molten material which originally lay closer to beam center. The initial accretion of material to form a rim may have involved the surface-tension-controlled, iris-like withdrawal of molten metal away from the site of hole nucleation—an hypothesis which is compatible with a widely observed tendency of small holes to be smooth-edged and circular. However, further expansion must proceed by drawing cooler liquid metal into the rim from an

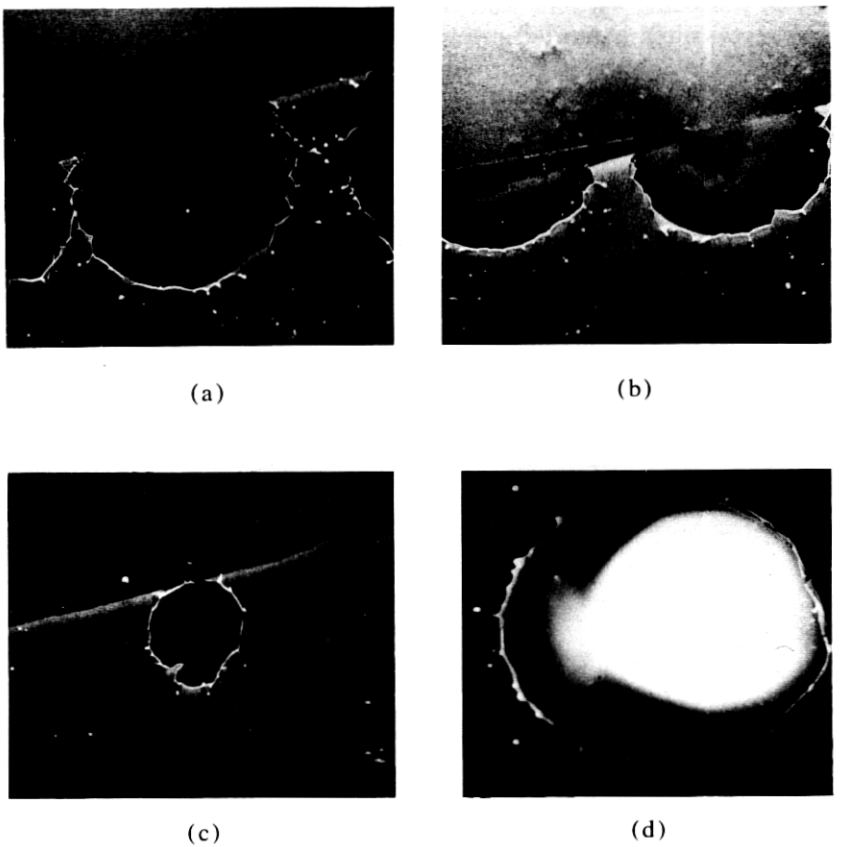

Fig. 17—Regularities in the debris patterns of holes machined in "optimally-thick" bismuth films. The following descriptions refer to holes machined in 400Å-thick bismuth evaporated onto Mylar.* A 30-ns-duration, cavity-dumped, YAG-laser beam of 6.8-μm diameter at $1/e^2$ of maximum intensity was employed. (a)–(c) A straight film boundary was sharply defined by masking the evaporation with a knife edge. Holes of incomplete circumference were formed by translating the machining beam at a shallow angle to the boundary. Vapor-pressure buildup could not have occurred with these holes. Segmentation of the hole rims and the regular spacing of metal drops around them are clues to the hole opening kinematics. (d) Regularly spaced beads are visible in the rim of a complete hole.

* Registered trademark of E. I. DuPont de Nemours.

incrementally larger radius and redistributing it circumferentially into beads whose spacing and maximum size are characteristic of the film thickness. Once it acquires spherical shape, a bead is somewhat insulated both from the incident beam and from the rest of the film and may persist briefly as a superheated liquid droplet after its surroundings have resolidified.

5.2 Film oxidation

The preceding sections hint that the laser-machining shelf life of thin metal films is limited primarily by the growth of mechanically rigid oxide structures which must be melted or ruptured before hole nucleation and enlargement can proceed. *Melting* the oxide may permit hole nucleation in pinhole-free, thick films subject only to surface oxidation; but *rupture* by attainment of high metal vapor pressures is required to nucleate holes in films which contain a high

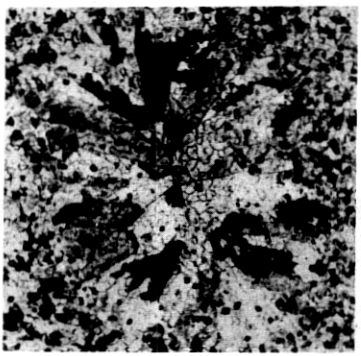

(a)

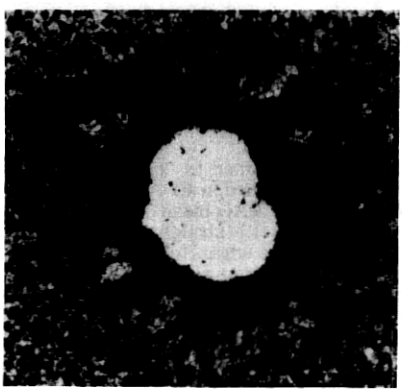

(b)

(c)

density of oxide-filled pinholes or whose preparation has incorporated oxygen into the crystalline grain boundaries. Evidence for the types of surface and bulk oxide structures present in thin metal films, and their effects on hole machining, is given in Figs. 18 through 21.

5.2.1 Surface oxidation

Figure 18 consists of transmission electron micrographs of laser-irradiated areas of 540Å-thick, free-standing bismuth film. The area shown in Fig. 18a was irradiated with two or three laser pulses, each of energy sufficient to melt the metal but not the oxide; the metal is seen to resolidify after each pulse into large, radially oriented crystallites while the oxide (faint pattern within the grains) retains the structure of the original, as-evaporated metal crystallites. If the area is subjected, as in Fig. 18b, to a total of 20 such pulses, a hole is eventually produced, the opening being bridged by an intact skeleton which can be identified as a surface oxide.

The practical effect of this surface oxide on laser-machined miniature images is revealed by Figs. 18c, 18d, 18e, and 19. Unmelted surface oxide surrounds the holes in Figs. 18c and 18d. These holes were

(d)

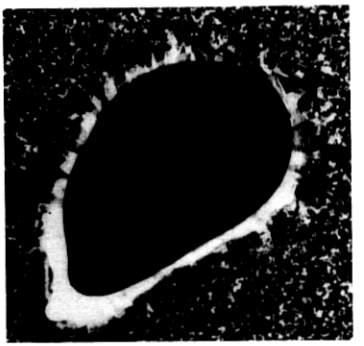

(e)

Fig. 18—Resolidification in bismuth films at various machining energies, illustrating nucleation delay caused by surface oxidation. Transmission electron micrographs of 540Å-thick, free-standing bismuth film irradiated with a cavity-dumped He-Ne beam for the pulse-power conditions described in the text. Very similar data are found for 700Å-thick films. The areas that have melted and resolidified are defined by the large, radially oriented gains. The low-contrast tracery in (a) and (b) establishes the existence of a thin surface oxide whose structure corresponds to the crystalline matrix of the as-evaporated metal. This tracery remains visible in (c) and (d), which depict holes machined just above threshold. Hole diameters near threshold are much smaller than the diameter to which the film was melted; i.e., because the hole opening is restrained by the surface oxide, the temperatures underneath beam center were able to reach values significantly higher than the 660°C equivalent temperature corresponding to the enthalpy to melt bismuth. Large holes (e) consume a much larger fraction of the maximum liquidus diameter. Note that the annulus surrounding the hole of (e) has recrystallized by heat flow perpendicular to the hole boundary.

produced by single pulses at energies just above machining threshold, and they are very much smaller than the diameter to which the metal was melted. In contrast, hole diameters approach the molten diameter at high machining energies, as shown in Fig. 18e. This tendency finds quantitative expression in the "two-diameter" picture of hole machining suggested by Fig. 19. Data points lying within the dotted region of this figure represent the hole "areas" (hole diameters squared) machined in numerous bismuth films ranging in thickness from 420 to 980Å as functions of volume energy density (i.e., absorbed machining-energy-density per unit film thickness). Film temperatures have been associated with the abscissa by using the experimental result (obtained

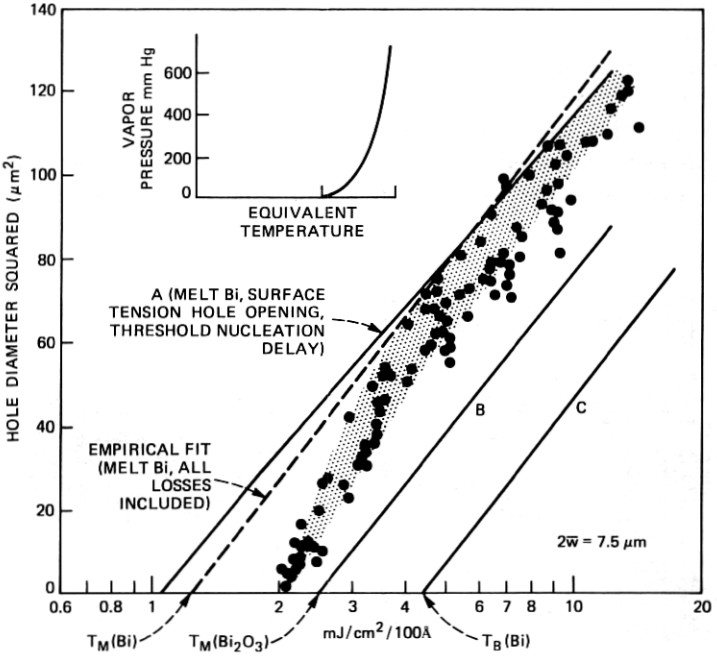

Fig. 19—Dependence of machined-hole areas in surface-oxidized bismuth films on absorbed volume-energy-density: hypothetical and measured dependence. The ordinate is the square of the hole diameter in units of $(\mu m)^2$. The abscissa is the logarithm of absorbed volume-energy-density, in units of millijoules/cm^2 in the focused machining beam per 100Å of bismuth thickness. A temperature scale derived from film-resistivity data (see text) has been fitted to the abscissa. The equivalent-temperature scale of the vapor pressure (inset) corresponds to this abscissa. The data (dotted region) represent the diameter squared of holes machined in numerous bismuth films, ranging in thickness from 350Å to 1000Å, by a pulsed YAG-laser beam of 7.5-μm diameter at $1/e$-intensity and of 30-ns duration. Incident beam power was varied with neutral-density filters. Film optical absorptions were measured in independent experiments. Curve A was calculated from eqs. (2) and (3) of the text for a 900Å-thick film, assuming τ = 300 ns thermal-relaxation time and hole-nucleation delay time shorter than the laser pulse duration. Lines B and C were obtained from eq. (2) evaluated for $\tau = \infty$. Line B corresponds to hole diameters determined by the enthalpy needed to reach the Bi_2O_3 melting point, line C to that needed to reach the Bi boiling point.

by monitoring film resistance during machining, viz. Section 5.3.1) that the pulse energy needed to nucleate holes in 500Å-thick bismuth film is approximately twice that needed to melt the metal (including heat of fusion) and hence is enough to raise the film to 900°C, slightly above the Bi_2O_3 melting point. The semilogarithmic straight lines A, B, and C in Fig. 19 are the predicted[46] machining curves if the final hole diameters in 500Å-thick bismuth were determined, at all pulse energies, by freezeback of the bismuth liquidus, by freezeback of the Bi_2O_3 liquidus, or by attainment of the bismuth boiling temperature, respectively.

The rapid dependence of hole area on machining energy at the transition between melt-oxide and melt-metal machining explains the observation that gray-level tonality is very hard to control near the "black" end of the contrast scale in unprotected films of low-melting-temperature metals (such as evaporated bismuth) and in alloys which do not form intermetallic compounds (such as the Bi/Pb-alloy). Such films usually lose the fight against surface oxidation within a few hours, and their gray-scale reproducibility is especially sensitive to film aging. Indeed, definition of the final hole diameter in terms of the metal melting enthalpy at all pulse energies—i.e., curve A of Fig. 19—is observed in the case of bismuth only for *in vacuo* machining of freshly evaporated metal. Also, machining and SEM data on metallic Ni and electroless nickel[47] indicate that these slow-oxidizing films remain in the "melt-metal" mode for about 10^5 hours at room temperature. Further, hole formation in certain multiconstituent films which remain free of oxygen throughout most of their lives can be described in terms of a chemically stable "melt-compound" mode analogous to the "melt metal" mode of curve A. This machining process, described in Section 5.4, applies to fairly thick composite films, such as Se/Bi, which can form tightly bound interfacial compounds (Bi_2Se_3) that prevent bulk oxidation of the bismuth.

5.2.2 Bulk oxidation

5.2.2.1 Pinhole-Rich Films. The deliberate fabrication of pinhole-rich films has been proposed as a means of artificially seeding the film with hole nucleation sites and lowering the threshold machining energy. The discussion of Fig. 16 shows that this scheme won't work. The film thickness for maximum machining efficiency coincides with a critical value—dependent on substrate surface roughness and on film deposition conditions—below which the layer uniformity and continuity of bismuth evaporated onto Mylar* are poor, resulting in high pinhole density in the finished film. Mechanically stiff oxides develop readily

* Trademark of E. I. DuPont de Nemours Company.

within the volume of pinhole-rich films and impair machining. Electrical conductivity measurements support the hypothesis that extensive oxidation at the metal-substrate interface, centered around the foot of each pinhole, lifts metal from the substrate because of the increased volume displaced by the oxide. This exposes an appreciable area of fresh metal around the base of each pinhole to reaction with oxygen and increases the size of the foot.

Sufficiently thin free-standing films are also pinhole rich. Figure 20 consists of SEM and TEM micrographs of 340Å-thick, free-standing bismuth films laser-machined at different pulse energies. These suggest that hole nucleation may occur at several locations near beam center, perhaps caused by independent melting of the oxide pillars lining the pinholes. Figures 20b and 20c show that liquid metal released by

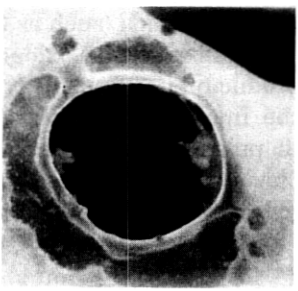

(a)

(b)

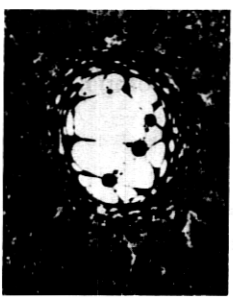

(c)

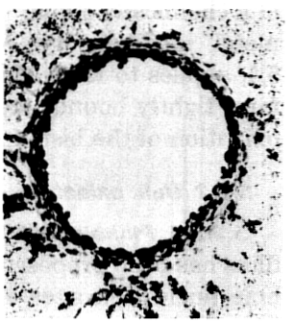

(d)

Fig. 20—Hole machining in presence of bulk oxidation. The micrographs for this figure were obtained from 340Å-thick, free-standing bismuth film machined by 25-ns-duration pulses from a cavity-dumped He-Ne laser. Heavy oxidation of this film can be presumed because of the exposure of both its surfaces to atmospheric oxygen and because of the presence of numerous pinholes. (a) SEM micrograph suggesting an oxide membrane surrounded by resolidified metal and perforated by several holes frozen in the process of coalescing into one hole. (b)–(d) TEM micrographs of areas irradiated at progressively higher powers. See text.

independent meltings beads up into nodes connected by oxide threads. These threads contract toward the oxide liquid boundary, pulling the nodes after them and producing the clustering seen in Fig. 20c. The outer resolidification boundaries in Figs. 20b, 20c, and 20d are identified with the bismuth liquidus, and the inner boundaries with the Bi_2O_3 liquidus; a similar identification is suggested by Fig. 20a. The machined hole diameters are seen to equal, at most, the diameter to which the oxide can be melted.

5.2.2.2 Heavily Oxidized Thick Films. The grain sizes of sputtered metal films tend to be much smaller than those of evaporated films. Complete oxide penetration even of fairly thick films occurred readily in sputtered films of tin and indium, producing individual metal grains imbedded in an oxide honeycomb. Melting the oxide changes this structure from a solid to a liquid honeycomb, but it does not nucleate holes. Experimentally, hole nucleation requires that the honeycomb be ruptured mechanically by heating the metal to approximately its boiling temperature. A hole initiated near beam center then enlarges to the boundary defined by the metal boiling point and, if the oxide structure is strong, stops there. The machining curves of Fig. 21 indicate that hole formation in sputtered tin and indium can be described in terms of this "boiling-point" mode.

However if the oxide structure is weak, it may be torn away when the hole opens, causing the machining to switch from the boiling-point mode near threshold to an oxide mode at high powers. This appears to be the case for sputtered bismuth, as is consistent with electron microscopy data which show that its crystallites are appreciably larger than those of sputtered tin and indium and present correspondingly less surface area for oxidation.

Despite their higher threshold machining energies, a certain interest persists in films of the above type. Since the sputtered coatings represent an extreme state of oxidation, they have the virtue of being comparatively stable against further loss of machining efficiency with age, and can be considered whenever sufficiently high-pulse-power lasers are available. The inclusion in sputtered films of a soluble element to increase the vapor pressure has been proposed as a means of lowering their machining threshold. However, a trial of this proposal on sputtered Bi/Sb film produced no improvement in machining over sputtered bismuth.

Strong oxide honeycombs which require boiling-point machining can be formed in other ways. The oxide Bi_2O_3 has been investigated as an antireflection coating between the transparent substrate and the deposited bismuth film, for use when the machining laser beam is incident onto the metal through the substrate ("back machining," viz. Section 5.4). The Bi_2O_3 is vacuum-evaporated in a high oxygen am-

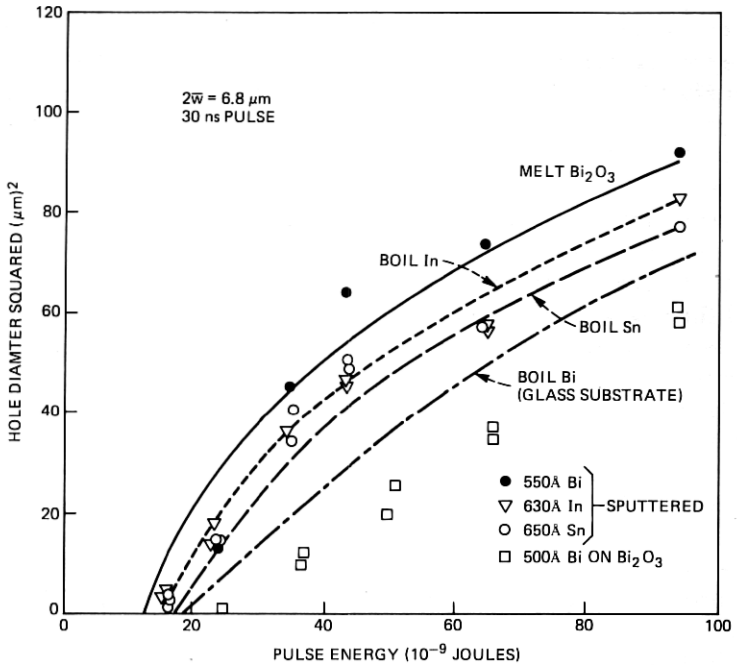

Fig. 21—Machining curves for oxidized films of bismuth, indium, and tin. Squares of machined-hole diameters are shown as functions of incident pulse energy for 1-percent transmitting films of bismuth (●), (550Å thick, 400Å grain size), indium (▽), (630Å thick, 150Å grain size), and tin (○), (650Å thick, 150Å grain size), sputtered onto polyethylene teraphalate substrate, and for bismuth evaporated onto Bi_2O_3 without breaking vacuum (□). The 30-ns-duration pulse was obtained from a cavity-dumped YAG laser; the focussed machining-beam diameter was 6.8 μm at the 1/e-intensity level. The curves were calculated from the simplified hole-opening models, eqs. (2) and (3) of the text, with Rayleigh velocities estimated from listed surface-tension values, and thermal-relaxation times scaled from the 300-ns value for 500Å-thick bismuth and the specific heats of the various metals. Comparison between these calculated curves and the machining data indicates that the temperatures of small-grain size, sputtered, indium and tin films must be raised to the metal boiling point to nucleate holes, but the temperature of large-grain-size, sputtered bismuth need be raised only up to the Bi_2O_3 melting point. Forces even higher than the vapor pressures obtainable at the boiling point are required to break the tenacious Bi/Bi_2O_3 bonds.

bient. If bismuth is evaporated onto this surface without breaking the vacuum, tenacious bonds surround the metal grains so tightly that the bismuth must be brought to its boiling point to rupture them. As shown in Fig. 21, it is difficult to machine large holes in such films until substantially more energy has been supplied than the boiling point energy.

5.2.3 Control of surface energy and thermal impedance at the metal-substrate interface

The polyethylene teraphalate substrate (Mylar or Celanar*) evolves impurities at room temperature that tend to oxidize the bismuth metal

* This polyester is a trade name of the Celanese Company.

deposited on it. This evolution eventually forces the machining into an oxide-dominated mode, even though the upper surface of the metal may be protected from atmospheric oxygen, and is believed to be the principal aging mechanism in dielectric-overcoated metal films (such as Se/Bi) deposited directly onto the substrate. It is possible to block the evolution of oxygen and to modify the surface energy (both favorably and unfavorably) by overcoating the substrate with selected, thin, transparent films prior to evaporating the metal. For example, poly-isobutyl methacrylate (IBM)* flourinated ethylene polymer (FEP), TiO_2 exposed to air, and cross-linked vinyltrimethylsilane (VTMS) have low surface energies and affect machining favorably; high-surface-energy polyamide (PA), polyvinylidine chloride (PC), and fresh Bi_2O_3 coatings on the substrate produce the opposite effect. A comparison of bismuth machining curves made with various undercoatings is shown in Fig. 22. All these coatings reduce the evolution rate of substrate impurities.

Substrate overcoatings can modify the thermal impedance for heat flow between the metal and the bulk substrate and can also modify the film-substrate interface bonding energy. Even though a free liquid surface may exist at the metal-air interface, the metal may be so strongly bound to the substrate as to delay nucleation or to reduce the hole opening velocity significantly, allowing appreciable resolidification to occur before the final hole diameter is reached. Thus, changes in bonding energy should primarily affect the hole diameters which can be attained at energies somewhat above threshold, whereas increases in thermal impedance—i.e., in the thermal relaxation time τ—should both lower the threshold energy and increase the final hole diameter. (However, for cases in which hole nucleation involves lifting the metal from the substrate, reductions in substrate surface energy can improve the ease with which a dome or blister can form, via the reduced adhesion.) Adhesion and scratch resistance must obviously be considered in any effort to improve machining by reducing the bonding energy. The TiO_2 (and also the VTMS) overcoating probably increased both the characteristic thermal decay time and the hole opening velocity. In correlation, metals deposited on these two overcoatings have extremely poor adhesion to the substrate, whence the improved machining is without practical value. An approximate factor-of-two reduction in machining threshold, relative to bismuth on Mylar, is gained by the use of an IBM overcoating of the substrate, as seen in Fig. 22. The apparent effect of IBM is to permit the nucleation of small holes in bismuth at machining energies close to the "melt-metal" limit

* The IBM overcoating is prepared by solution-dipping Mylar in a 5-percent concentration of IBM in methyl ethyl ketone.

(curve A of Fig. 19); larger holes, already restrained by this limit, are less affected. Adequacy of the adhesion of the weakest interface in a complicated layer combination such as Se/Bi/IBM/Mylar can be determined on a "pass-fail" basis by the "Scotch-Tape-test." Scratch resistance, obtained quantitatively by varying the load on a 25-μm radius sapphire stylus, is sensitive[48] both to adhesion and to the

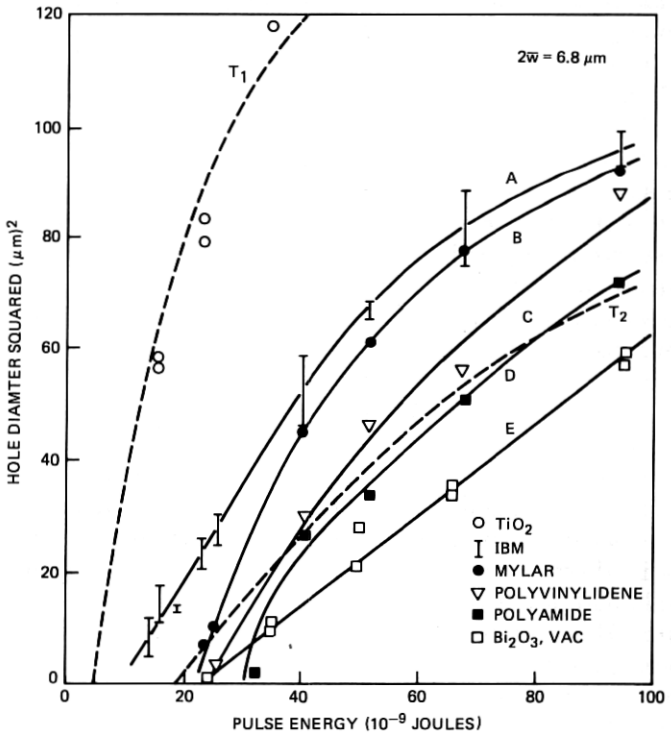

Fig. 22—Effect of substrate overcoatings on machining of bismuth films. Cavity-dumped YAG-laser beam of 30-ns duration, focused to 6.8-μm diameter at 1/e-intensity. ○—Back-machining data for 500Å-Bi evaporated onto 100Å-thick TiO_2 on glass; curve T_1 calculated for melt-bismuth, zero-heat-loss limit. Similar data have been measured for VTMS overcoatings on Mylar. I—Front-machining data for 600Å-Bi evaporated onto IBM on Celanar* (Celanar solution—dipped in 5-percent concentration of isobutyl-methacrylate in MEK); smooth curve A connects data points. ●—No overcoating; 600Å-thick Bi on Mylar, front-machined; smooth curve B drawn through data points. ▽, ■—Front-machining data for 600Å-Bi evaporated onto polyvinylidene (▽) or polyamide (■) on Mylar; smooth curves *C* and *D* connect data points. □—500Å-Bi evaporated onto 3600Å-Bi_2O_3 on 7059 glass and front-machined without breaking vacuum. Curve T_2 calculated for bismuth-boiling-point, zero-heat-loss machining; smooth curve *E* connects data points.

* Trademark of Celanese Corporation.

coefficient of friction at the selenium surface. The weakest link in the above film combination is found to occur at the IBM/Mylar interface. Recent data indicate that this interface can be strengthened satisfactorily, and the machining efficiency at high energies improved slightly, if the IBM is copolymered with a vinyl acetate. Results of adhesion and scratch tests are summarized in Table I.

5.3 Machining limitations set by laminar heat losses and optical absorption

The machining data of Figs. 16, 19, and 21 indicate that the incident intensities in Gaussian profile beams must equal 50–60 mj/cm^2 (at 1.06-μm wavelength) to produce the 900°C temperatures needed to nucleate holes in 500Å-thick, surface-oxidized bismuth evaporated onto Mylar, and must approach 200 mj/cm^2 to provide the range of hole sizes needed for high-quality microimage machining. These requirements on the laser are representative of the most favorable which can be achieved with single-element metal films, as is shown in this section.

Present GaAs lasers cannot machine practical microimages in single-element metal films even with the assistance of low-surface-energy undercoatings (viz. Fig. 22 and Table I). The film modifications needed to bring microimage machining within reach of GaAs lasers are described in Section 5.4.

5.3.1 Thermal conduction effects

The effects of laminar heat conduction on hole machining have been studied for surface-oxidized bismuth on Mylar and for the Se/Bi/Mylar system, using cavity-dumped gas lasers whose focused beams can be adequately approximated by Gaussian intensity profiles. Machining curves (hole-diameter-squared versus beam-energy or peak-power) were measured with pulse duration T as a parameter. They were compared with a machining model in which the film temperature at time T and at a radius equal to (or at least correlated with) the final hole radius was assigned a physically definite, characteristic value, e.g., the bismuth or Bi_2Se_3 melting temperature. The film temperatures

Table I—Adhesion and scratch test summary

Film Structure	Scratch Resistance (grams)	Scotch Tape Test (pass/fail)	Machining Performance with GaAs Laser
Bi/Mylar	2	fail	unusable
Se/Bi/Mylar	100	pass	good
Se/Bi/IBM/Mylar	10–15	fail	excellent
Se/Bi/IBM/Mylar*	~ 100	pass	best

* IBM copolymered with vinyl acetate.

were calculated[2] from the time-dependent heat equation,[3] assuming zero thermal impedance at the metal/Mylar interface and optical absorption only in the metal. (Resolidification diameters in the free-standing films of Figs. 18 and 20 were predicted accurately by assuming that all heat delivered to the film is redistributed by radial thermal conduction and that no optical power is lost by premature hole opening.)

The hole sizes machined in 600Å-Se/600Å-Bi/Mylar film by a cavity-dumped He-Ne laser beam of 3.2 μm diameter at $1/e$ intensity and 25 ns to 5000 ns pulse duration are plotted in Figs. 23a and 23b as functions of total pulse energy and of peak pulse power. A progressive increase in the total energy required to machine a given hole size occurs as the pulse duration is lengthened. This failure of "reciprocity" was observed for all hole sizes, and is illustrated in Fig. 23c for holes of 16-$(\mu m)^2$ area. Figure 23c shows that the machining energies required as functions of pulse duration T are compatible with calculations from the laminar-flow heat equation (normalized to the data at $T = 25$ ns). Earlier data[2] on the Bi/Mylar system also agree with the laminar flow calculation, similarly normalized at $T = 25$ ns. The overall energy efficiency, including heat loss during the pulse as well as the effects of refreezing, is illustrated in Fig. 23d for holes whose diameter approximately equals the laser beam $1/e^2$-intensity diameter. The machining efficiency of 100-ns-duration pulses is about 60 to 65 percent of the efficiency obtained with very short (25 ns) pulses.

The close agreement between experiment and theory in Fig. 23c has implications for hole-opening kinematics in the fairly thick films pertinent to these data. It appears that machining a hole of diameter d depends primarily upon attaining a physically definite temperature profile in unruptured regions of the film at the end of the laser pulse, no matter what the pulse duration. The data presented in Fig. 19 show that the diameter d of holes machined at energies somewhat above threshold in films of 500Å thickness and greater approaches the diameter to which the metal melts.

The time evolution of the molten diameter (liquidus) is estimated here by approximating the effects of film heat loss with a thermal relaxation time τ. The heat content at radius r and time t, per unit area of (unruptured) film, for a film whose absorptance at the laser wavelength is A and for a Gaussian profile beam of power P and pulse duration T whose $1/e$-intensity diameter is $2\bar{w}$, may be written

$$u = \begin{cases} (AP/\pi\bar{w}^2)e^{-(r/\bar{w})^2}\tau(1 - e^{-t/\tau}), & 0 \leq t \leq T \\ u_T e^{-(r/\bar{w})^2}e^{-(t-T)/\tau}, & t \geq T, \end{cases} \tag{1}$$

in which $u_T = A\tau(1 - e^{-T/\tau})(P/\pi\bar{w}^2)$ is the heat content per unit area at $r = 0$, $t = T$. The value $\tau = 300$ ns has been estimated for 500Å-thick

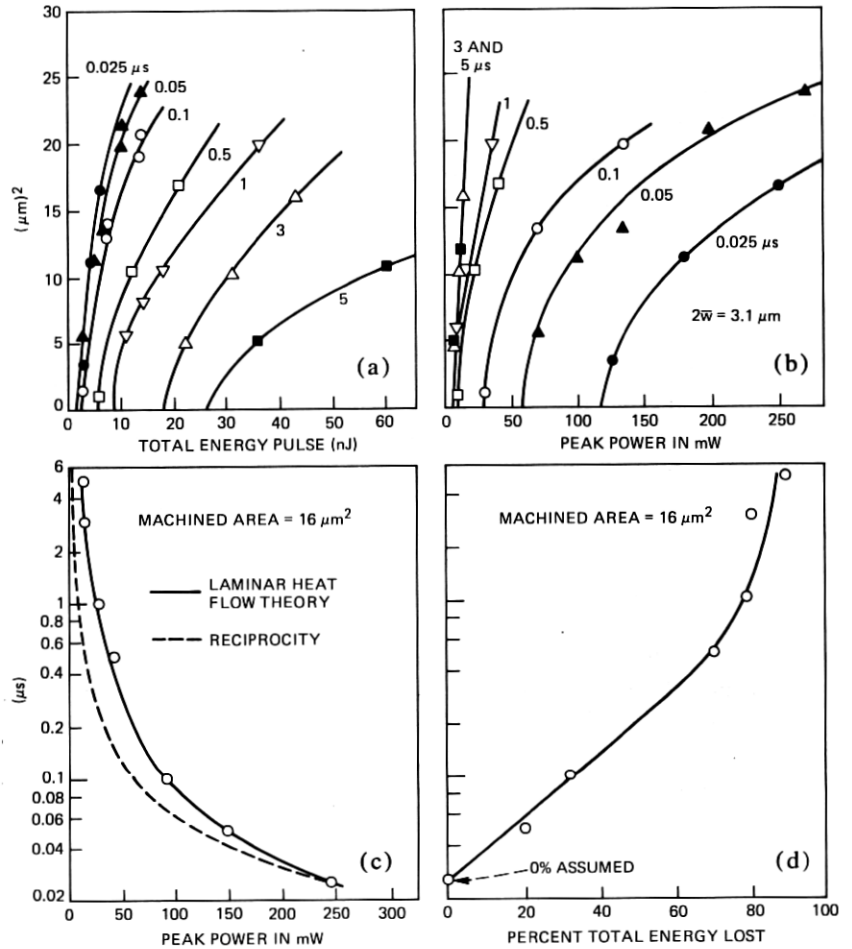

Fig. 23—The effect of pulse duration on hole machining by a Gaussian-profile laser beam. A cavity-dumped, He-Ne, laser beam at 0.63-μm wavelength incident onto Se/Bi film was used to obtain these data. A 1/e-intensity full width of $2\bar{w} = 3.1$ μm for the focused beam was estimated from the diameter at the entrance pupil of the 8-mm-focal-length writing lens. The smooth curves in (a), (b), and (d) have no theoretical significance. (a) Square of machined hole diameter versus total pulse energy (in units of 10^{-9} joules) for pulse durations from 0.025 to 5 μs. (b) The same data plotted versus peak pulse power. (c) The pulse duration versus peak pulse power required to machine a 16-μm^2 hole. The dashed curve is calculated assuming that reciprocity holds; the solid curve is obtained from the laminar heat-conduction model of Ref. 2. Both curves are normalized to the 0.025-μs data point. (d) Machining inefficiency of long-duration pulses, relative to the 0.025-μs pulse.

bismuth evaporated onto Mylar by measuring resistance changes in a 3-μm × 3-μm neck of film heated by a 25-ns-duration YAG laser pulse. (The beam diameter was about 8 μm at 1/*e*-intensity, and construction of the neck was such that only laminar heat flow to the substrate was important in the measurement.)

The position of the liquidus as a function of time is obtained by equating $u(r, t)$ to the enthalpy h_M needed to melt a unit area of the film starting from room temperature. The liquidus radius is given, in the approximation $T/\tau \ll 1$, by

$$(r/\bar{w}) = \begin{cases} 0, & t/T \leqslant h_M/u_T \\ [\log(u_T/h_M) + \log(t/T)]^{1/2}, & (h_M/u_T) \leqslant t/T \leqslant 1 \\ [\log(u_T/h_M) - (t-T)/\tau]^{1/2}, & t/T \geqslant 1. \end{cases} \quad (2)$$

(The inequalities $T/\tau < 0.1$ and $T/\tau < 0.3$ apply to practical microimage machining by cavity-dumped lasers and by GaAs lasers respectively.) The film melts underneath beam center at the instant $t_M = (h_M/u_T)T$. The liquidus expands to a maximum radius $(r_c/\bar{w}) = [\log(u_T/h_M)]^{1/2}$ at $t = T$, and then begins to contract as resolidification propagates inward. This growth and contraction are illustrated in Fig. 24 for a metal and its oxide, assuming $\tau/T = 3$. The example is chosen to correspond to bismuth, for which the enthalpy to reach the Bi_2O_3 melting temperature is 1.8 times the enthalpy to melt bismuth.

Equation (2) does not include the radial redistribution of heat which occurs when hot (possibly superheated) melt is transported away from beam center as the hole opens, nor are the possible effects of viscosity considered. Indeed, a kinematical description of hole opening which incorporates these effects is forbiddingly complicated. Fortunately, as is apparent from Fig. 24, the details of hole nucleation and enlargement are irrelevant in determining the hole size if τ is large enough. If the film stays hot for a long time, the hole diameter will always approach the molten metal diameter (oxide structure permitting). Alternatively, τ need not be large if hole nucleation and enlargement are prompt. The hole-opening loci in Fig. 24 were drawn by supposing, for the sake of definiteness, that hole nucleation occurs in the neighborhood of beam center after a specified delay, and that the hole opens outward like an iris at a radial speed estimated by equating the kinetic energy of the displaced material to the released surface energy. (Composite films whose viscosity has been increased[7] by the incorporation of arsenic or selenium might be expected best to exemplify iris-like hole opening. However, data presented in Fig. 26 below suggest that the hole opening dynamics in selenium-containing films do not differ greatly from those in slightly oxidized bismuth films of the same thickness.) If the surface energy of the hole debris is neglected, this speed has the constant value (Rayleigh velocity)[40] $v_R = \sqrt{4\gamma/\sigma}$, expressed in terms of the surface tension γ (erg/cm^2) and film surface density σ (gm/cm^2), and leads to the expression

$$(r/\bar{w}) = (v_R/\bar{w})(t - t_N) \quad (3)$$

for the hypothetical hole rim loci in Fig. 24. The calculated Rayleigh

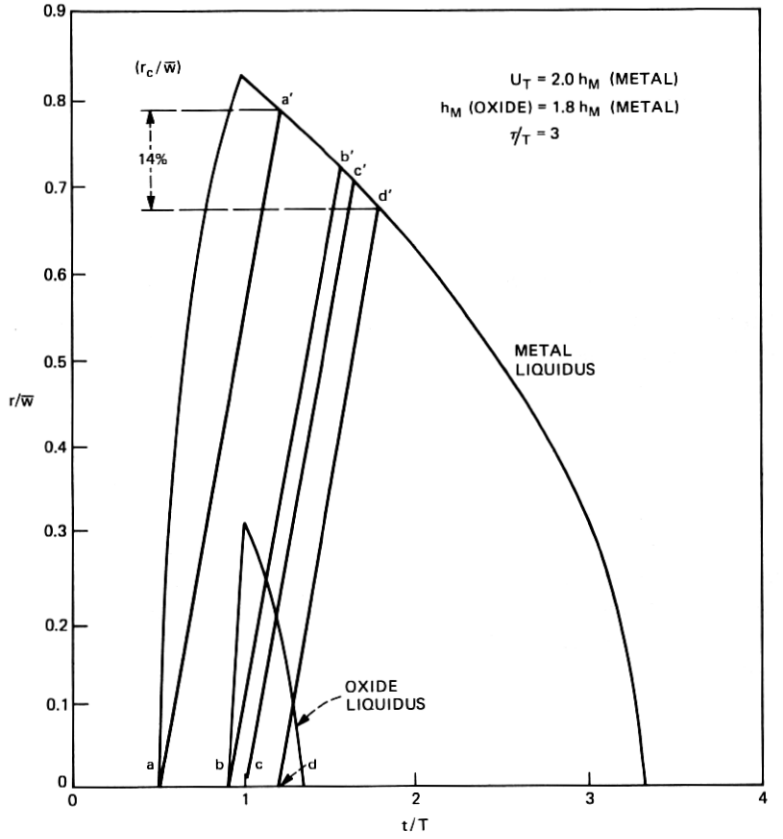

Fig. 24—Generalized kinematical hole-opening model. This figure applies to the case in which threshold is determined by melting a weak surface oxide and large holes are limited by the molten metal diameter. It is intended to show that the final hole diameter is comparatively insensitive to kinematical details if the thermal relaxation time is long and the hole enlargement speed high. The radius r of the metal or oxide liquid-solid boundary is given in units of $\bar{w}$, the laser beam $1/e$-intensity radius. The laser pulse begins at time $t = 0$ and ends at time $t = T$. The metal- and oxide-liquidus loci were obtained from eq. (2) for a case in which the laser pulse energy u_T equals twice the enthalpy $h_M(m)$ needed to melt the metal, and $\tau/T = 3$. The enthalpy $H_M(ox)$ needed to reach the oxide melting point was taken equal to 1.8 $H_M(m)$, corresponding to m = Bi, $ox = Bi_2O_3$. Solid lines are loci of hypothetical hole peripherys, with points a' through d' representing final hole sizes as determined by freezeback of the metal. The lines were obtained from eq. (3) for $(v_R T/\bar{w}) = 1.15$, corresponding to $\bar{w} = 3.4$ μm, $T = 61 \times 10^{-9}$ s, v_R (Rayleigh velocity) $= 5.3 \times 10^3$ cm/s. Line aa' represents the limit of zero nucleation-delay time; i.e., hole opening initiated by melting the metal; line bb' depicts hole opening initiated by melting the oxide; line cc' corresponds to nucleation at the end of the laser pulse; and line dd' illustrates an opening delayed nearly until the onset of oxide freezeback. Note that this wide range of physical conditions produces only a 14-percent spread in hole diameters, and that the predicted diameters are 80 to 85 percent of the maximum molten-metal diameter.

velocities of 1-percent-visible-wavelength-transmitting bismuth, tin, and indium films range from 53 to 67 $\mu m/\mu s$, whence released surface energy is sufficient to enlarge the rim diameter to 6 μm within 50 ns of the hole nucleation instant. If nucleation occurs at the end of the laser pulse, this diameter will intersect the resolidification front (i.e., the final hole diameter will equal 6 μm) of an irradiated area melted to 7.1-μm diameter. This type of result is compatible with the data in Fig. 19 for holes machined well above threshold.

5.3.2 Limitations set by the optical absorption of single-element films

Since laser-machined images are intended for projection viewing by transmitted visible light, the visible-wavelength transmission of unmachined areas must be limited to some generally acceptable maximum to obtain good "black-white" contrast. The transmittance[49] of a specularly reflecting metal film depends on its complex refractive index, $N = n - jk$, evaluated for the wavelengths in question, on its thickness b, and on the incidence angle. When a transmittance value such as 1 percent is assigned for normally incident visible light, n and k become functionally related, with film thickness b as a parameter, as shown in Fig. 25a. (Projection light is incident over angles ranging up to 30 degrees, so the practical transmission of these films is less than 1 percent.) By assuming that this same functional relationship applies at the machining laser wavelength, the absorptance A of these films for laser radiation can be plotted versus n, as is done in Fig. 25b for $\lambda = 0.89$ μm.

The temperature to which any of the above films, whose visible-wavelength transmittance is 1 percent, can be heated by a given intensity of laser radiation depends on its *specific* absorption, A/b, at the laser wavelength and on appropriate film enthalpies evaluated on a per-unit-volume basis. The maximum possible value which can exist for the specific absorption of a 1-percent-transmitting film of given thickness,* as obtained from the curves of Fig. 25b, is plotted in Fig. 25c. The specific absorptions† and thicknesses of 1-percent-transmitting films of various low-melting-point metals have been calculated from bulk optical constants,[50] and it is seen that specularly reflecting films of bismuth, zinc, cadmium, and antimony approach the (A/b) limiting curve at thicknesses in the range 500 to 600Å. (Higher specific absorption limits could be realized with thinner films. But even if metals with the required n and k values existed, Fig. 16 indicates that they would probably be pinhole-rich and would not machine well

* The films must obey the further restriction $n \leq 10$, $k \leq 10$.

† The measured absorptance of 500Å-thick bismuth films is about 20 percent smaller than the absorptance calculated from bulk optical constants in the wavelength range 0.63 to 1.15 μm.

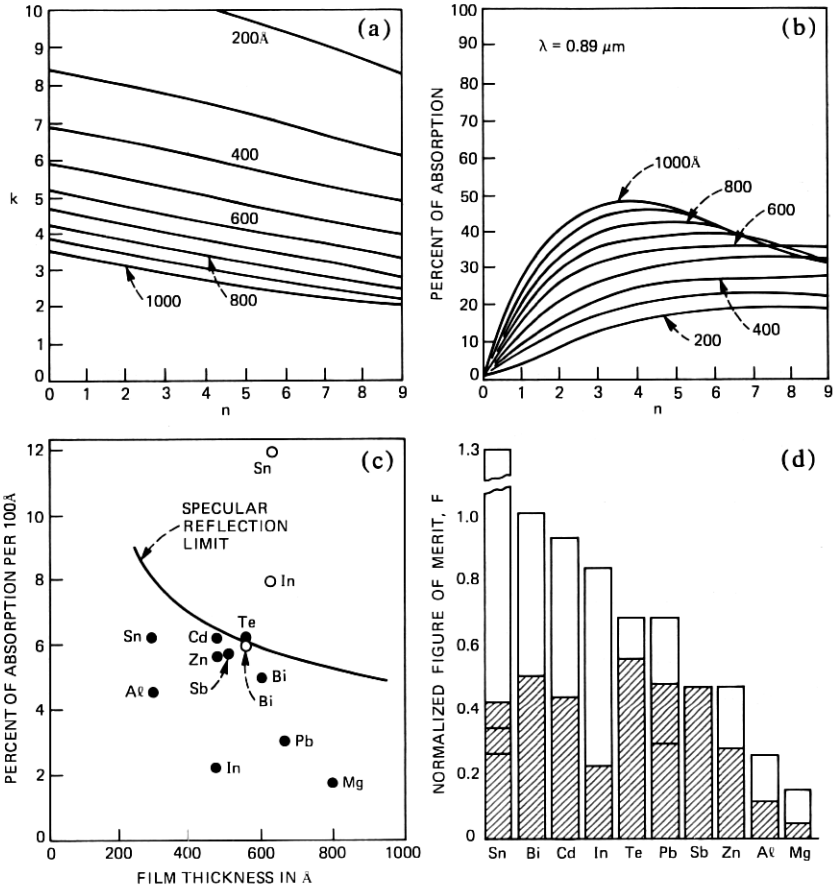

Fig. 25—Optical and thermodynamic limitations on the laser machining of high-contrast microimages in single-element metal films. The descriptions which follow refer to films whose optical transmission at 0.63-μm wavelength equals 1-percent. (a) Real (n) vs. imaginary (k) refractive indices at 0.89-μm wavelength for 1-percent transmitting films of different thickness. (b) The percentage of incident flux at 0.89-μm wavelength which is absorbed in 1-percent-transmitting films of different thickness, as a function of real refractive index, n. (c) The smooth curve is the maximum percentage absorption per 100Å of film thickness, as obtained from the locus of absorption maxima in (b), versus film thickness. The specific absorptions of 1-percent transmitting films of various single-element metals, as calculated from bulk values of their optical constants, are shown as solid dots. The measured specific absorptions of several sputtered films, whose reflection is believed *not* to be specular, are indicated by open circles. (d) The machining figure-of-merit F for single element metals is defined as the absorption per unit thickness divided by the enthalpy per unit volume needed to reach hypothetical hole-nucleation conditions, as follows; values of F for melting the metal (including heat of fusion) are shown by the open bars, normalized to the F-value for melting bismuth; values of F for reaching the oxide melting temperature (excluding the oxide heat of fusion) are shown by the shaded bars, with multiple values indicated for tin and lead, which have more than one possible oxide.

unless they happened to be non-oxidizing.) Figure 25c indicates that specularly reflecting, single-metal film systems are limited to efficiencies of about 35 percent in their ability to absorb light. The measured (A/b) values of *diffusely* reflecting, sputtered tin and indium, shown in Fig. 25c, exceed the specular-reflection limit, a possibility for films whose structure can trap radiation; however, erroneously large values of (A/b) could also have been caused by failure to detect all the reflected light.

Machining figures-of-merit, F, can be defined for actual metals as $F = A_b/(\Delta H_v \cdot b)$, in which A_b is the fraction of laser radiation absorbed in a film of thickness b, obtained either from direct measurement or from appropriate optical constants, and ΔH_v is the enthalpy per unit volume either to melt the metal or to raise its temperature to the oxide melting point. Figure 25d indicates the figures of merit calculated from bulk optical constants at 0.89-μm wavelength, for the various low-melting-point metals of Fig. 25c, normalized to the melt-bismuth F-value. The thickness of each film was chosen so the transmitted intensity was 1 percent at 0.63-μm wavelength, and it is seen that none appears strongly preferable to bismuth and its oxide with respect to the incident radiation needed to satisfy the enthalpy requirements for nucleating and enlarging holes. The nonspecular, sputtered films of indium and tin are found to have machining efficiencies similar to, but not much better than, those of evaporated bismuth (viz. Fig. 22). Since usually more than half the enthalpy needed to melt a metal (starting from room temperature) is associated with the heat of fusion, amorphous alloys, which require no latent heat to melt, may be energetically preferable to their crystalline counterparts even though their specific heats are higher. Electroless nickel[47,51] (an amorphous alloy of nickel and phosphorus), despite its high melting point, has exhibited comparable machining efficiency (and vastly superior scratch resistance and oxidation stability) to bismuth. The As-Te thin films for which excellent laser-machining characteristics have been reported[7] are also amorphous.

Unfortunately, the machining energy requirements for facsimile microimage application of evaporated and sputtered single metal systems, and of all the amorphous alloys investigated, lie a factor of 2 or 3 beyond the practical reach of present GaAs lasers. Figures 23d and 25c indicate that the incident energy for machining could be reduced about a factor of 4 from its value for bismuth (viz., Fig. 19) if the optical absorption were increased to 100 percent and the thermal conductivity to zero without, in the process, adding to the hole formation enthalpy. In fact, very long laminar-heat-loss relaxation times probably *have* been achieved with TiO_2 and vinyltrimethylsilane (VTMS) undercoatings (viz., Fig. 22), but in both cases film adhesion

to the substrate was reduced well below acceptable limits. The most important *practical* machining energy improvements have resulted from the modifications in optical absorption described in Section 5.4.

5.4 Practical multilayer films: the bismuth-selenium system

Antireflective overcoatings can increase the optical absorption of a single-metal film and reduce its rate of oxidation by the atmosphere, but improvements in machining may be thwarted by the added mass which must be melted and displaced, and by possible complications in the hole-opening dynamics. The most obvious counter to this difficulty—substrate-incident machining with an antireflection coating sandwiched between substrate and metal—has proved to be only marginally practical. It has been attempted with bismuth, whose oxide Bi_2O_3 is transparent to visible light, and is a fairly good, near-infrared, antireflection match[52] between the metal and a substrate of 1.5 refractive-index value. Improved machining was obtained by exposing an evaporated Bi_2O_3 layer to air prior to evaporating bismuth, but such films did not age reproducibly.* The combination Bi/Se/Bi on Mylar can also be made antireflective for substrate-incident machining if the bismuth layer adjacent to the Mylar is very thin (75Å). Substrate-incident machining of such films was comparable, but not superior, to the air-incident machining of Se/Bi on Mylar near threshold, and was poorer well above threshold. Further, when substrate-incident machining was attempted with printers in which the film substrate was tensioned over a transparent film gate, position-dependent optical interference occurred between the film gate and the contacting surface of the substrate, producing unintended hole-size modulations similar to those caused by mode destabilization (Section 4.2.3) and preventing gray-scale rendition. The antireflection structures described[41,53] for use with optically recorded video disks are inapplicable when the machined image is viewed by transmitted light.

The largest step toward better machining efficiency has been made by recognizing that the mass added by overcoating can be used to advantage if it consists of an element or compound which mixes exothermically with the metal when both are molten. Low-melting-point dielectrics with high refractive indices comprise one group of overcoating possibilities. For example, a 660Å thickness of selenium[54] (n = 2.56 at 0.89-μm wavelength) deposited on 600Å-thick bismuth trebles the optical absorption at 0.89-μm wavelength from 30 to about 90 percent. But since 2.3 times as much energy is now needed to melt both constituents, the resulting film figure-of-merit (Fig. 25d), consid-

* Sequential evaporation of Bi_2O_3 and bismuth without breaking vacuum produced very stable films but extremely high machining energies, as shown in Figs. 21 and 22.

ering just these factors, would improve only about 29 percent. However, a large exothermic reaction occurs[8,55] when the molten bismuth and selenium mix, as would be expected for two components which tend to form strongly bound intermediate phases. The released energy maximizes at 5.4 Kcal/mole corresponding to the composition Bi_2Se_3. The maximum temperature which the film system can achieve is self-limited by vaporization of selenium. The machining threshold figure-of-merit calculated for this system at stiochiometry is about five times that of a single-layer bismuth film, assuming that there is no selenium vaporization.

A measured comparison between the machining curves of 1-percent-visible-light transmitting bismuth and Se/Bi film is shown in Fig. 26; the energy in 30-ns-duration YAG-laser pulses required to reach machining threshold in Se/Bi has been decreased about a factor of 3.5 from that at the 1.06-μm wavelength for which the optical absorption of the Se/Bi combination was maximized. Uncertainty in the quantity of selenium vaporized and relatively minor departures from exact stoichiometry are sufficient to account for observed differences between the expected and the measured machining performance of the Se/Bi system. The photographic montage of Fig. 26 illustrates a debris pattern consisting of balled-up droplets (presumably Bi_2Se_3) inside and outside the hole, and of beads strung around the peripheral rim. More debris appears inside the holes than was found for the thick bismuth films of Fig. 16, a result suggesting that hole opening in this relatively thick film is not dominated by the viscosity of the molten material. (But compare Ref. 7.) The increase in debris is not enough to detract seriously from microimage quality in transmitted light.

This rather dramatic result prompted the investigation of many two- and three-layer film systems. The machining performance of the most interesting of these is shown in Fig. 27; data on single-layer bismuth, with and without an IBM overcoating, are included from Figs. 22 and 26 for comparison. These curves represent holes produced by YAG-laser pulses of 30-ns duration and variable peak power. The various multilayer film compositions were adjusted to maximize the optical absorption of 1-percent-transmitting film at this wavelength. Although several of these compositions machine better than Se/Bi on polyethylene teraphalate, the Se/Bi system remains the most attractive since both of its components can be evaporated sequentially without breaking vacuum, thereby producing a film of controlled composition with the bismuth well-protected from the atmosphere. In contrast, indium layers of multiconstituent films are difficult to deposit, and the stoichiometry of Sb_2S_3 is difficult to assure.

The fractional improvement in machining brought about by an IBM undercoating of the Se/Bi/Mylar system is essentially the same as its

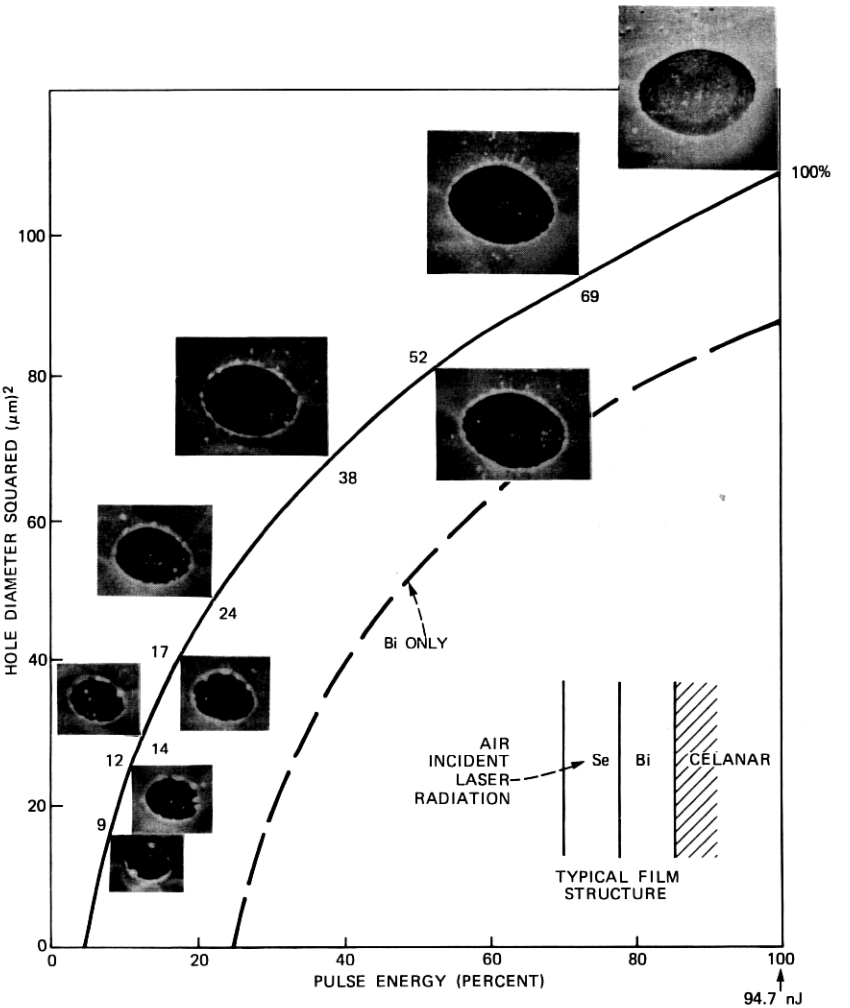

Fig. 26—Size and appearance of holes machined in Se/Bi film as function of laser pulse energy; comparison with bismuth machining curve. The montage of SEM photographs shows the appearance of holes machined in the air/860Å Se/750Å-Bi/substrate film system by the beam from a cavity-dumped YAG laser. The machining pulse duration was 30 ns, and the focused beam diameter was 6.8 μm at 1/e-intensity. The incident pulse energy is given as a percentage of 94.7×10^{-9} joules. The Se/Bi film was less than 0.3-percent transmitting at 0.63-μm wavelength, and the 500Å-thick bismuth film was about 1.5-percent transmitting. The Se/Bi machining threshold power is 7.5 nJ, and 6-μm-diameter holes are machined at 16 nJ.

fractional improvement of the Bi/Mylar system (viz. Fig. 22). The net effect of this undercoating on Se/Bi machining is to shift the Se/Bi curve of Fig. 27 down to the neighborhood of the Se/Bi/In curve. Thus, compared to a single layer of bismuth on Mylar (curve *k*), the

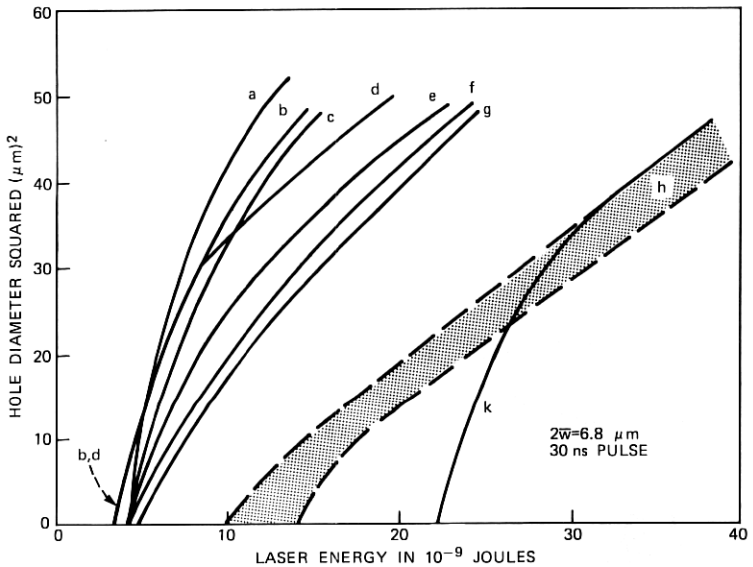

Fig. 27—Machining curves of various two- and three-layer, antireflective film systems; comparison with bismuth. The substrate is 100-μm-thick polyethylene teraphalate (Mylar or Celanar), and the 6.8-μm, 1/e-intensity-diameter, cavity-dumped, YAG-laser beam is incident from air. (a) Air/Se/Bi/IBM/substrate. (b) Air/Se/Bi/In/substrate. (c) Air/Se/In/substrate. (d) Air/Sb_2S_3/Bi/substrate. (e) Air/Se/Bi/substrate. (f) Air/Se/In/Bi/substrate. (g) Air/Bi_2S_3/Bi/substrate. (h) Air/Bi/IBM/substrate. (k) Air/Bi/substrate. The stippled band (*h*) includes data from many film samples.

machining threshold energy of Se/Bi/IBM/Mylar has been lowered a factor of 6, and the energy needed to machine 6-μm-diameter holes has been lowered a factor of 4. This improvement places the Se/Bi/IBM system well within the pulse-power capabilities of the GaAs laser described in Sections III and IV.

5.5 Film chemical stability; shelf life; archival life

The life of unmachined film ends when either its visible-wavelength opacity or its machining efficiency decrease below assigned limits. Optical absorptance declines monotonically with time in low-melting-temperature, single-metal films because opaque metal is gradually converted to optically transparent metal oxide. This increased transparency reduces the image contrast achievable with the film. It also reduces the heat generated by the incident beam, adding to the difficulty of melting the oxide whose stiffness impairs hole nucleation and enlargement. In the earliest stages of aging (identified with planar oxidation of surface crystallites), a gradual increase in film electrical resistivity accompanies the increased optical transmission, and near-threshold machining exhibits the transition from the "melt-metal" to the "melt-oxide" mode (data trend in Fig. 19). Gradual, monotonic

increases in optical transmission continue as the single-metal film ages. Eventually, however, a penetration of oxygen into the film is produced by creepage of oxide tentacles between grain boundaries and by evolution of oxidizing impurities from the substrate. This interrupts the continuity of the metal, causing an abrupt resistivity increase and forcing the machining from the "melt-oxide" into the "boiling-point" mode (curves B and C of Fig. 19).

Changes in the optical transmission at 0.63-μm wavelength of 20 single-metal and multi-constituent film systems have been studied in aging runs conducted at temperatures between 40° and 125°C. Some of these elevated-temperature runs have lasted up to 4000 hours. Both monotonic and nonmonotonic changes in optical transmission with aging time have been observed. End of life in the monotonic cases has been defined as the number of hours required for transmission to increase by a factor of 1.5 from its initial value of 1 percent. Plots of this longevity versus the reciprocal of aging temperature are given in Fig. 28 for bismuth and for eight multiconstituent film systems. In a few cases, the data define straight lines, inviting extrapolation to suggest a value of room-temperature shelf life. No theoretical justification exists for this procedure, since the aging chemistry is generally unknown. Aging results exist for several other systems: thus, sputtered bismuth and indium age about a factor of 10 less rapidly than evaporated bismuth, sputtered tin ages much more rapidly, and aging effects have been undetectable in nickel and Ni_xP_y films.

The optical transmission of multilayers such as Se/Bi whose constituents can react chemically with one another is not monotonic with aging time and does not correspond monotonically to machining efficiency. Chemical reactions at the layer interfaces can increase opacity even while the machining efficiency is decreasing, and a number of reactions may be possible. The following reactions are capable of affecting the shelf life of unmachined Se/Bi/IBM films:

(*i*) Transition[56] of as-evaporated amorphous selenium to crystalline selenium.

(*ii*) Formation of an interfacial layer of Bi_2Se_3 (and/or BiSe).

(*iii*) Glass transition of poly-IBM (at about 70°C).

(*iv*) Formation of Bi_2O_3 by impurities evolved from substrate.

Shelf lives of the Se/Bi and Se/Bi/IBM systems have been studied by measuring changes in machining efficiency and optical transmission. Inclusion of the IBM coating appears not to change film aging significantly. Two different formats for presenting aging data on the Se/Bi/IBM system are used in Figs. 29 and 30. (The high machining threshold of Se/Bi/IBM in Fig. 30 is an artifact caused by the aging conditions: the layer thicknesses were optimized for $\lambda 0.89$ μm but were machined at $\lambda 1.06$ μm during the aging runs.) Quite as expected, the percentage

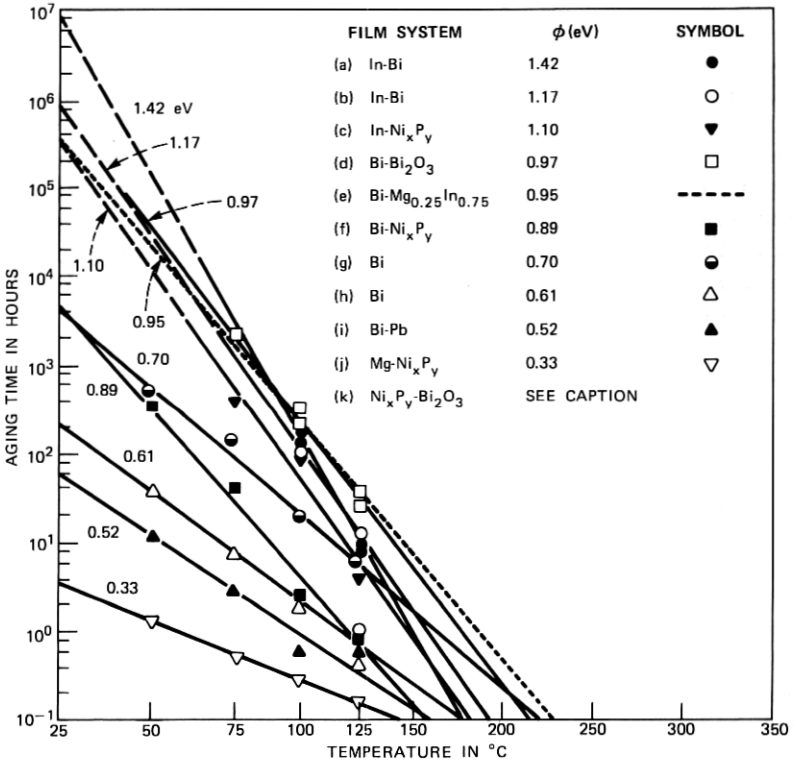

Fig. 28—Longevity of nonreactive, multiconstituent film systems at elevated temperatures. The ordinate is the number of hours required, at the chosen elevated temperature (abscissa), for the film optical transmission at 0.63-μm wavelength to increase by 50-percent from its initial value. Description of the film systems are: (a) In-Bi/Celanar: metals co-evaporated from separate sources to 500Å total thickness; machines similarly to Bi. (b) In-Bi/Celanar: alternate layers evaporated to a total of 5 Bi layers, 4 In layers, 500Å total thickness; requires higher machining power than (a). (c) Air/In/Ni_xP_y/Celanar: 10-percent-transmitting, evaporated Ni_xP_y, overcoated by 1.7-percent-transmitting, evaporated In; intended for substrate-incident machining where it performs better than (a). (d) Air/Bi/Bi_2O_3/Celanar: 500Å-Bi, evaporated onto 3600Å-Bi_2O_3; requires more than boiling point enthalpy to machine (similar to Fig. 22, curve *E*). (e) Air/Bi/$Mg_{0.25}In_{0.75}$/Celanar: $Mg_{0.25}In_{0.75}$ alloy sputtered to 86-percent transmission, then Bi sputtered to 1-percent transmission; intended for substrate-incident machining where it performs comparably to Bi/IBM (Fig. 22, Curve *A*). (f) Air/Bi/Ni_xP_y/Celanar: 10-percent-transmitting Ni_xP_y, 1-percent-transmitting Bi, constructed similarly to (c); machines similarly to (a). (g) Air/Bi/Celanar: 500Å-thick, fast-evaporated Bi (data from one evaporation run). (h) Air/Bi/Celanar: same as (g), but average of three evaporation runs. (i) Bi-Pb/Celanar: prepared similarly to (a); machines better than (a), but ages very rapidly. (j) Air/Mg/Ni_xP_y/Celanar: prepared similarly to (c) and (f); machines better than (a), but ages very rapidly. (k) Air/Ni_xP_y/Bi_2O_3/Celanar: machines like Bi and does not age; the oxide Bi_2O_3 is 3400Å thick (3 λ/4), and Ni_xP_y is 1.4-percent transmitting. Estimates of activation energy φ, in eV, are listed.

change in hole area caused by film aging is large near machining threshold, but decreases monotonically as the hole area increases. Specifically, Fig. 30 shows that the Se/Bi/IBM system machines along a single semilogarithmic curve and that 7000 hours of aging at 25°C

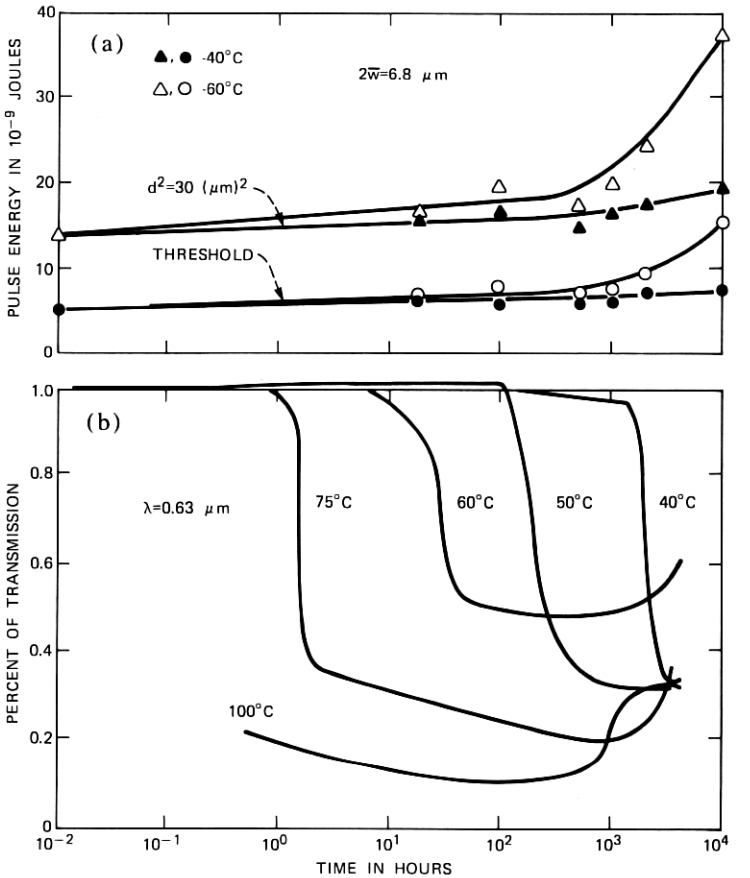

Fig. 29—Longevity of Se/Bi/IBM film system at elevated temperatures. (a) The pulse energies (ordinate) required to reach machining threshold and to machine 5.5-μm-diameter holes were measured at the indicated times (abscissa) on film samples maintained at 40° and 60°C. The film system is air/Se/Bi/IBM/Mylar. (b) Optical transmissions at 0.68-μm wavelength were measured as functions of time for the above film samples at temperatures up to 100°C. The transmission changes are nonmonotonic and are not closely correlated with changes in machining behavior.

causes a 30-percent increase in the energies required to machine large holes. Film shelf life depends, in a practical situation, on the gray-scale requirements of the printer usage and also on the effort expended to automate the electronic control of gray scale. As is shown in Section VIII, effective room temperature shelf life exceeding 10 years can be predicted if gray-scale capability is restricted or forfeited.

Once an image has been machined in Se/Bi film, it is protected and stabilized by the formation of Bi_2Se_3. Images of the IEEE Test Chart (viz. Section VIII) subjected to aging at 125°C for 2000 hours show only slightly degraded readability and gray-scale quality. Close exam-

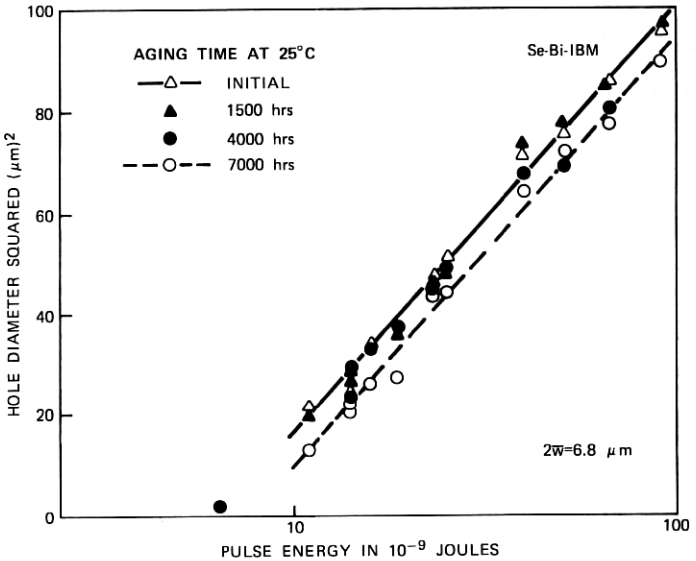

Fig. 30—Changes in machining curves of the Se/Bi/IBM film system with age at room temperature. The apparently high machining threshold for this film occurred because the Se and Bi thicknesses were optimized for use at $\lambda = 0.89$ μm, but the machining data were acquired at $\lambda = 1.06$ μm. The rapid dependence on aging time of hole size near threshold indicates that this film has less than one year shelf life for reproducible machining of gray scale. However, it is quite suitable for high-contrast use for much longer than one year (see Fig. 47).

ination reveals that the degradation has not occurred in the metal image, but instead that crystallites have grown on the Mylar substrate. The several millenia of room-temperature archival life for gray scale in Se/Bi images, suggested by these tests, is not unexpected. Whereas a single-metal film decreases in optical opacity as it ages so that images machined therein eventually lose all contrast, the Se/Bi bilayer increases in optical opacity (Fig. 29b). Hence the contrast between machined and unmachined areas of Se/Bi improves with age, and the gray scale, which is controlled by the fractional machined area, is preserved.

VI. GENERAL OPTICAL CONSIDERATIONS; MACHINING PERFORMANCE WITH GaAs

Generally speaking, the beam-acquisition, guidance, and machining optics in a metal-film-machining printer must be corrected to ~$\lambda/4$-net-optical-path difference from laser to film and must include cylindrical correction of beam astigmatism and ellipticity in printers employing GaAs lasers. Optics whose spherical aberration is equivalent to that of good commercial microscope objectives appear to be ade-

quate, whereas medium-to-large-aperture photographic lenses and projection lenses, even of the best commercial quality, will not deliver a properly focused beam onto the film; they produce poorly shaped holes with low machining efficiency and are only marginally usable even with the high powers provided by cavity-dumped YAG and ArII lasers. The optics may contain more than two dozen air-glass interfaces which, because of the limited GaAs laser power, must have high overall transmission. Typical overall optical throughputs of 75 to 80 percent have been obtained with the aid of single-layer, dielectric, antireflection coatings.

6.1 Beam-acquisition methods

Referring to Fig. 31, consider the astigmatic GaAs laser as an idealized optical source consisting of two displaced orthogonal, cylindrical beam waists with a common principal ray propagating along the $+z$-axis. The waist located at $z = 0$ has a small width, $2w_y(0) \approx 1.5$ μm, from which rays diverge in the $y - z$ plane; the waist located at $z = -A$ has a larger width, $2w_x(-A) \approx 3$ μm, from which rays diverge in the $x - z$ plane.

Although the far-field radiation pattern from these waists is sometimes treated according to the propagation law for cylindrical Gaussian beams,[30] actually neither waist is Gaussian. More realistic physical approximations to the cavity mode spatial dependence have been used to calculate[29] far-field, $y - z$ plane, angular distributions from the Kirchoff-Huygens formalism which agree fairly well with measurement. But the complicated secondary lobe patterns of mode profiles measured parallel to the junction plane (viz. Fig. 11) suggest that a similar estimate for the $x - z$ plane will not be easy. A convincing theory of the junction-plane fields is not presently available.

6.1.1 Astigmatism correction at first-crossover point

The beams diverging from the two sources have a common diameter $2w(z_1)$ in a plane $z = z_1$ just beyond the laser mirror ($z_1 \approx 6$ to 8 μm), as seen in Fig. 31(a). This plane is in the far field of either source. Hence a cylindrical thin lens of focal length $f_y(z_1) = (1 + z_1/A)z_1$ located at z_1 will form a virtual image of the $z = 0$ source at $z = -A$ with magnification $M_y = 1 + A/z_1$. Since z_1 is a plane of beam circularity, this magnification will produce the equality $2w_y(0) \cdot M_y = 2w_x(-A)$. A system of spherical optics placed beyond plane z_1 and designed to image point $z = -A$ onto the film with magnification M will produce a circular machining waist of diameter $2w_F = (2w_x) \cdot M$. (Thus, a machining waist of 7.8-μm diameter at $1/e^2$-intensity represents an $M = 2.6$ magnification of the junction plane virtual waist $2w_x(-A) = 3$ μm).

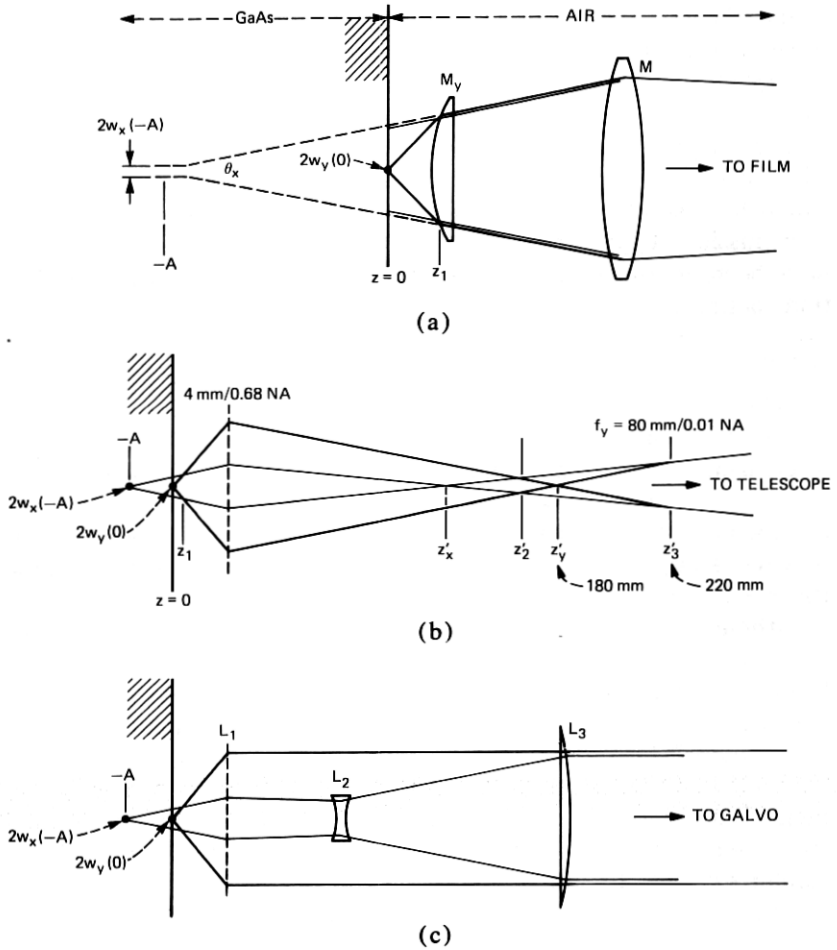

Fig. 31—Methods of acquiring GaAs laser beam. (a) Microoptical system: Intensity profile is circular in plane z_1, close to laser mirror; cylindrical lens M_y of appropriate focal length causes rays in $y - z$ plane to appear to diverge from point $z = -A$, whence spherical lens M can be used to form nonastigmatic, circular beam waist at film. (b) Microscope objective: Intensity profile is circular in plane z'_3, conjugate to plane z_1, and plane z'_x is conjugate to plane $z = -A$. Appropriate cylindrical lens at z'_3 causes rays in $y - z$ plane to appear to diverge from z'_x; subsequent spherical optics form nonastigmatic, circular, beam waist at film. (c) Two-cylinder telescope: Lens L_1 is spherical; lenses L_2 and L_3 refract rays in the x–z plane.

Cylindrical *thick* lenses of ~20-μm diameter and refractive index $n = 1.65$, made by drawing glass fibers from a hemicylindrical boule, can be positioned to yield approximately the same astigmatism and ellipticity corrections as the cylindrical thin lens. The *angular*-spherical-aberration coefficients[57] of such lenses are extremely large for the rapidly diverging ray fan perpendicular to the junction. But the lens

focal length is extremely small, and it turns out that the net lateral spherical aberration in the virtual image at $z = -A$ is a small fraction of the total image size. Rays emerge from the thick lens in an F/3 cone which, when introduced along the optical axis of a parabolic-graded-index glass-fiber lens,[58] can be focused into a ~7-μm-diameter spot on the film.

A printer utilizing these optics[12] has been constructed by aligning a GaAs laser and the two fiberoptic lenses just mentioned along a rigid, low-mass arm which was oscillated about the galvanometer axis. The laser emission acquired by the cylindrical lens was focused by the graded-index lens onto a curved section of film with ~75 μm of free working clearance. Microimages of 8-mm to 9-mm width were successfully back-machined in Se/Bi/Mylar film at ~260-kHz pulse repetition rate. The film radius of curvature was 19 mm.

6.1.2 Astigmatism correction at third-crossover point

A beam-acquisition system of smaller spherical aberration than that of the above micro-optical configuration can be obtained by using a large-NA microscope objective and a weak cylindrical lens, as shown in Fig. 31b. The objective is positioned to produce a real image of the waist $2w_y(0)$ at the design conjugate distance $z = z'_y = 180$ mm. The waist $2w_x(-A)$ will then be imaged at a distance in the range 120 mm $\leq z'_x \leq 140$ mm if the value of A is in the range 27 μm $\leq A \leq 47$ μm. Ray path calculations[59] for a modified, Bausch and Lomb, 4-mm focal length, 0.68-NA, microscope objective* show that optical path differences are smaller than $\lambda/4$ for conjugate points in the range 170 mm $\leq z'_y \leq 190$ mm when the lens is used at full aperture and at 0.9-μm wavelength. When the lens is used at 0.2 NA, the path differences are smaller than $\lambda/3$ for conjugate distances in the range 120 to 140 mm. Hence the microscope objective contributes little spherical aberration to the waists at z'_y and z'_x.

Unfortunately, a numerical aperture of 0.68 is insufficient to accommodate the rapidly diverging ray fan in the laser $y - z$ plane, and intensity profiles scanned in this direction generally exhibit some Fresnel diffraction (viz. Fig. 12b). High-transmission objectives with numerical apertures larger than 0.68 usually have very small working distances. They cannot be used here because the typical 8- to 10-degree beam-steering angle creates a mechanical interference between the laser mounting stud and the lens.

Two planes, z'_2 and z'_3, exist in the image field of the microscope objective at which the orthogonal ray fans have common diameters.

* The elements in this objective were specially spaced to minimize spherical aberration at 0.885-μm wavelength.

The plane z_3' is conjugate to the first-crossover plane z_1, and a cylindrical lens of focal length $f_y(z_3') = (z_3' - z_y')(z_3' - z_x')/(z_y' - z_x')$ placed there will superimpose a virtual image of the waist at z_y' onto the real image z_x', producing a nonastigmatic, circular beam beyond the lens.[13] The numerical aperture of this lens can be ~0.01, in contrast to the very large numerical aperture required for the microcylinder in Section 6.1.1. Hence its aberrations are extremely small; also its focal-length value is rather uncritical. The beam emerging from this lens is enlarged to a suitable diameter (viz. Section 7.1) and collimated by an F/7 Galilean telescope prior to deflection by the galvanometer mirror.

Beam correction can also be effected in less axial distance by using a cylindrical lens of focal length $f_x(z_2') = (z_2' - z_x')(z_y' - z_2')/(z_y' - z_x')$, located at the second-crossover position z_2', which superimposes a real image of the waist at z_x' onto the waist at z_y'. However, this lens requires critical tolerances on its focal length and a significantly larger aperture than 0.01, sacrificing the advantages cited in the previous paragraph.

6.1.3 Two-cylinder beam corrections

The path length from laser to galvanometer mirror is $z_G = 320$ mm when beam correction at point z_3' is followed by a Galilean collimating telescope. This length can be decreased by using two cylindrical lenses for beam correction. One such scheme, which shortens the laser-to-galvanometer distance to $z_G = 150$ mm, is outlined in Fig. 31c. The ray fan perpendicular to the junction plane ($y - z$ plane) is collimated to the desired final beam diameter by a specially constructed, large-working-distance, infinity-corrected, microscope objective. A cylindrical Galilean telescope is used to enlarge the ray fan in the $x - z$ plane and to collimate it to this same diameter.

For the sake of definiteness, suppose that the spherical elements form a beam waist in the $y - z$ plane at their exit pupil. Astigmatism will be eliminated if the Galilean telescope is adjusted to produce a waist in the $x - z$ plane at this same location. The lens of Fig. 31c is provided with mechanical adjustments for correcting astigmatism over a large range, $0 \leq A \leq 100$ μm. However, the cylinders must be large enough to accept the final beam diameter and must be carefully made to maintain aberrationless performance.

6.2 Machining focus and machining performance

Following its acquisition, the enlarged, collimated beam is deflected by a moving galvanometer mirror and focused onto the Se/Bi film by a scanning lens. This lens converts angular displacements of the collimated beam into a translation of the focused beam over a line in a flat focal plane. If the actual beam obeyed the propagation law for

Gaussian beams, the design of an optimal printer (i.e., one which machined a given size frame with minimum optical power) would be straightforward. With GaAs laser beams of the behavior illustrated by Figs. 9, 11, and 12a, deflection and machining apertures must be determined empirically, and even though the principal lobe of the GaAs beam often machines like a Gaussian profile beam, focusing of this lobe usually requires numerical apertures about double those needed for the Gaussian case.

6.2.1 *Focusing and machining performance of gallium-arsenide laser beams*

The numerical aperture requirements for machining with GaAs beams have been estimated by measuring focused beam profiles parallel and perpendicular to the laser junction plane with a mechanically scanned slit/photomultiplier arrangement for several focus conditions. The beam was enlarged and collimated to either 10-mm or 12-mm nominal diameter by an F/7 Galilean telescope and was then focused by lenses of either 37-mm or 50-mm focal length, nominally corrected to $\sim\lambda/4$ optical path difference at 0.885-μm wavelength. The effect of departures from good collimation were estimated by comparing profiles obtained with the telescope first adjusted to produce a beam waist at 15 m and then readjusted to produce the waist at (nominal) infinity. Small increases in the secondary mode amplitudes were noted for the 15-m position, but there was no change in the main (machining) lobe between the two adjustments. The beam-acquisition scheme of Sec. 6.1.2 was used ahead of the telescope with the astigmatism correction checked both visually and by profile scanning. The data shown in Fig. 32 illustrate the beam profiles for a particular focus condition (10-mm nominal collimated-beam diameter, 37-mm-focal-length machining lens) at several different laser currents.

Comparison of Figs. 12 and 32 supports our description of the focused, astigmatism-corrected beam as a superposition of the laser real and virtual waists, $w_y(0)$ and $w_x(-A)$. However, the relative amplitudes of secondary modes in the focused beam are functions of the convergence F-number (a fact not illustrated by Fig. 32) and are also influenced by particulars of the focusing optics. Variations within the secondary structure as the current is changed also depend obscurely on details of the focusing arrangement. The large secondary-mode background in Fig. 32 precludes use of the $1/e^2$-intensity width as a meaningful predictor of machining performance. However, the 1/e-intensity width, $2\bar{w}$, usually lies above this background.

The values of $2\bar{w}$ measured parallel and perpendicular to the junction at 1.5-A pulse current, and also the geometric mean of these values, are plotted in Fig. 33 as functions of the focusing F-number for the four focusing conditions mentioned above. The 1/e-intensity full

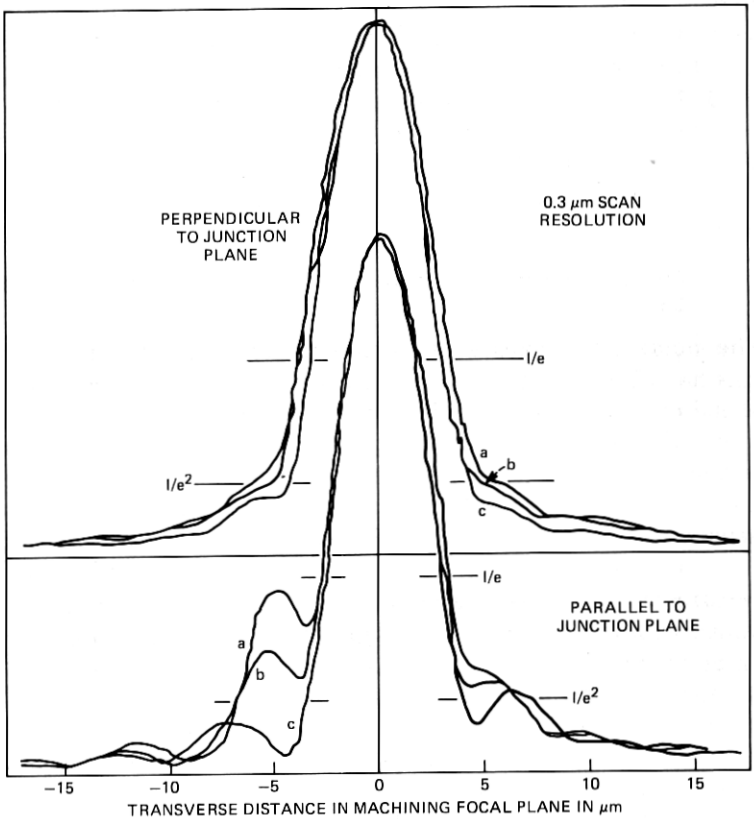

Fig. 32—Machining-beam profiles from GaAs laser. Profiles were measured in machining focal plane (i.e. plane of film) with mechanically scanned slit. Profiles a: 1.7-A laser pulse current, 100-ns duration. Profiles b: 1.5-A laser pulse current, 100-ns duration. Profiles c: 1.0-A laser pulse current, 100-ns duration. The machining beam was accurately corrected for astigmatism with an $f_y = 80$-mm cylindrical lens located at plane z_3' of Fig. 31b. Its residual ellipticity in the machining focal plane is 1.2:1 at the 1/e-intensity level. The beam was enlarged and collimated to 10-mm nominal diameter by an F/7 Galilean telescope and focused onto the film with a 37-mm-focal-length machining lens.

widths which would be produced by the same F-numbers with a Gaussian beam are also shown. We see that the numerical-aperture requirements for focusing the GaAs beams are approximately double those calculated from the Gaussian-beam expansion law.

A focusing arrangement which provides the required apertures over a large image field is illustrated in Fig. 34. The galvanometer mirror is positioned in the entrance pupil of a flat-field scanning lens. A telecentric lens design[60] (i.e., principal rays in the image space lie roughly parallel to the optic axis) was used to obtain enough spacing between the entrance pupil and the lens to keep the incident beam from

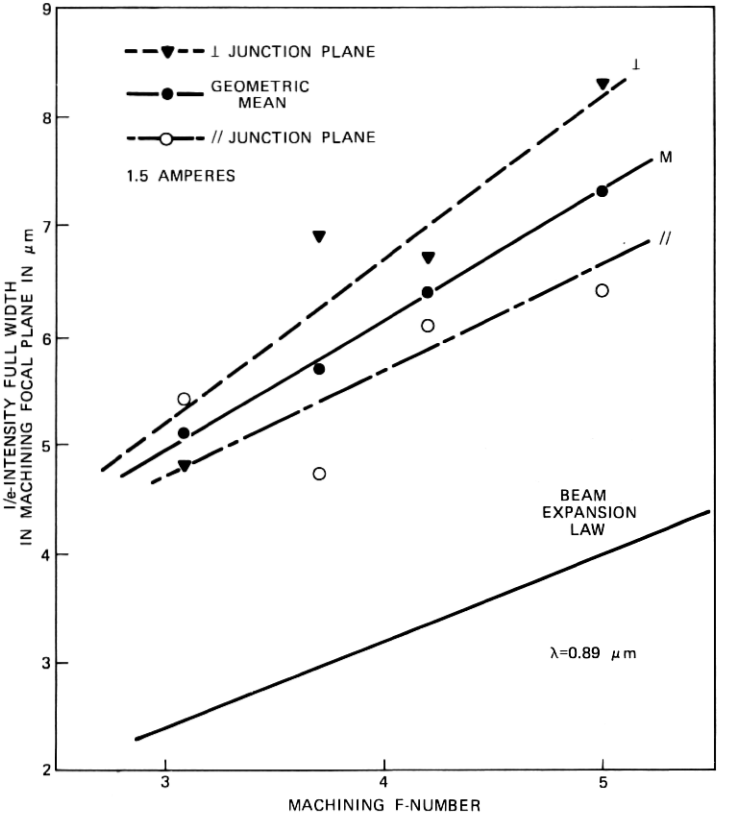

Fig. 33—Numerical-aperture requirements for focusing GaAs beam. The 1/e-intensity full widths of the machining-beam waist measured parallel and perpendicular to the junction plane are plotted versus the machining beam F-number (i.e., the ratio machining-lens-focal-length/collimated-beam-nominal-diameter) for 1.5-A laser current. Predictions of the Gaussian-beam expansion law at 0.89-μm wavelength are shown for comparison.

truncating on the lens housing. Tangent distortion was provided to produce images whose size scales linearly with galvanometer deflection angle. Several recent GaAs printers have employed a telecentric lens of focal length 36.7 mm, corrected to $\sim\lambda/4$ optical path difference over a 14.7-mm-diameter focal plane and over a chromatic bandwidth of $\pm$100Å centered at 0.887-μm wavelength. The entrance pupil diameter is 12.6 mm, spaced 18 mm from the lens. Figure 34, which is scaled to the above dimensions, suggests that a mirror-bias-angle $\psi = 40°$ should provide comfortable clearance between the lens body and the incoming collimated beam. The 14.7-mm field permits frames up to 9×11.6 mm to be optically raster-scanned. A lens designed to accommodate only the 9-mm-wide line scan could be physically much smaller.

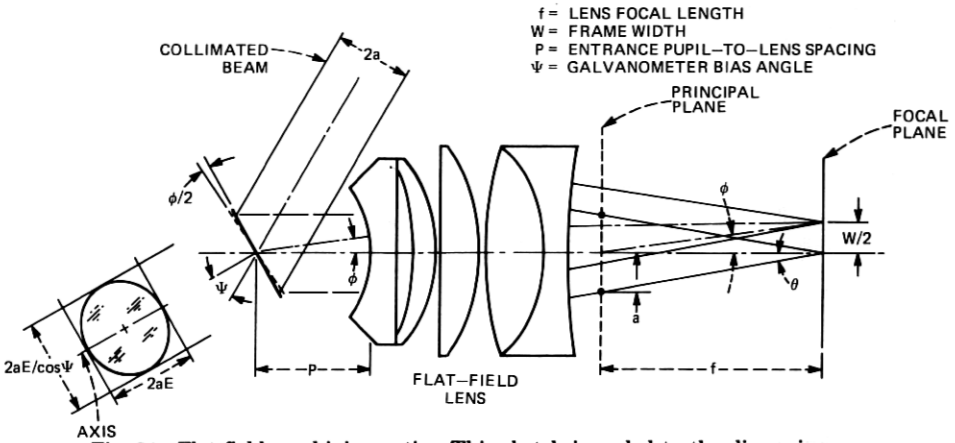

Fig. 34—Flat-field machining optics. This sketch is scaled to the dimensions mentioned in Section 6.2.1, with $P = 18$ mm and $f = 36.7$ mm. The machining F-number, $f/2a$, is limited to a minimum value of $(12.6/36.7)^{-1} = 2.9$. The image-field angular half width, $\phi = \tan^{-1}(W/2f)$, is limited to a maximum value of 11.3 degrees by the lens design. The lens-housing outside diameter equals 51 mm.

6.2.2 Gallium-arsenide machining curves

The scaling behavior for machining of unoxidized films with Gaussian profile beams of different diameters follows from eqs. (1) and (2): the power P_{th} required to reach machining threshold and the slope of the semi-logarithmic machining curve should both increase proportionally to the area $\pi\bar{w}^2$ of the focused beam. Figure 35 indicates that the machining produced by focusing the cavity-dumped beam from a He-Ne laser onto fresh Se/Bi film with various microscope objectives conforms at least qualitatively to these expectations. This figure compares the He-Ne data with machining curves measured for the GaAs laser and the four focusing conditions of Fig. 33. The GaAs machining results (with one exception) vary with width of the main machining lobe roughly as required by the above scaling laws; they exhibit higher machining thresholds than He-Ne curves of approximately the same slope, as expected from the diversion of power into secondary, nonmachining modes.

The comparison between GaAs and He-Ne laser machining results is continued in Fig. 36. The GaAs data were obtained with F/3 machining optics (viz. Figs. 32, 33) on 40 lasers selected from the same LPE-grown wafer. Figure 36 contains a sample of these data for nine lasers, and it repeats several He-Ne machining curves of Fig. 35. The nine GaAs curves would be coincident if the wafer produced identical lasers. The observed differences are attributed to differing proportions of power wasted in nonmachining secondary modes and to variations in width of the machining main lobe. The slopes of the GaAs curves fall roughly into two classes. Those curves having the smaller slope

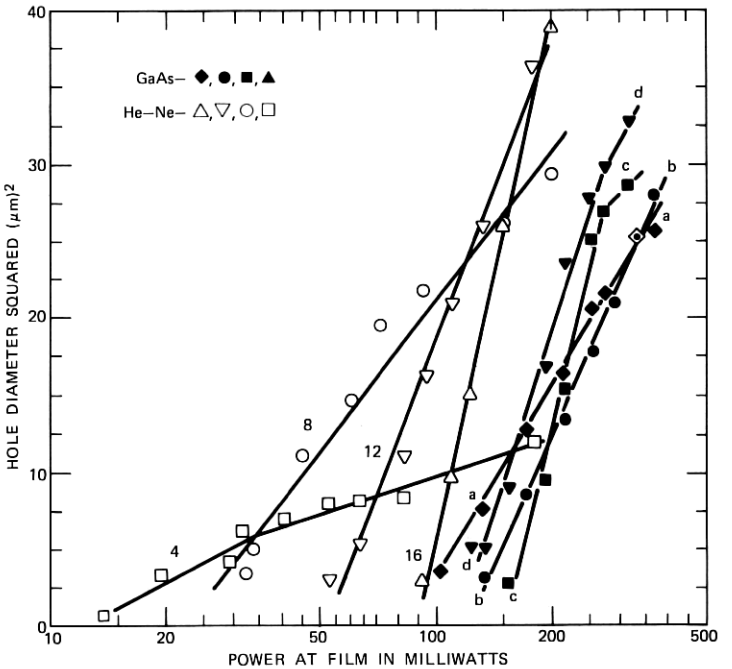

Fig. 35—Effect of focusing optics on machining; comparison of He-Ne and GaAs. Machined-hole diameter squared is plotted versus power incident onto film for the four GaAs-beam focus conditions of Fig. 33, and also for a cavity-dumped, 0.63-μm wavelength, He-Ne beam focused by various microscope objectives. The Se/Bi/Mylar film samples were separately optimized for machining by 0.89-μm- and 0.63-μm-wavelength beams. Solid symbols refer to machining of 600Å-Bi/600Å-Se film by 100-ns-duration GaAs pulses, with focused beam diameters $2\bar{w}$ at 1/e-intensity as follows: (◆, a)-5.1 μm; (●, b)-5.7 μm; (■, c)-7.3 μm; (▼, d)-6.4 μm. Open symbols refer to machining of 600Å-Bi/446Å-Se film by 100-ns-duration He-Ne pulses, with beam focused by microscope objectives of focal lengths as follows: (△, 16 mm), (▽, 12 mm), (○, 8 mm), (□, 4 mm).

value (shown dashed in Fig. 36) also have the lowest machining-threshold powers, whence the scaling laws suggest that these lasers have the smallest main-lobe width. Curves having the larger slope not only have larger threshold powers but also have a fairly large spread in thresholds; here, the scaling laws suggest a larger main-lobe width and varying fractions of power in nonmachining modes. Although some of the GaAs curves overlap He-Ne machining data, the machining thresholds for GaAs curves of given slope are never smaller than those for Ne-He curves of approximately the same slope.

A machining curve obtained by varying the pulse duration at a constant laser-pulse-current is shown in Fig. 37. (The data refer to the laser and the F/3 focusing conditions of Fig. 33.) The focused-spot profile is the same for each point on this curve, unlike the data of Fig.

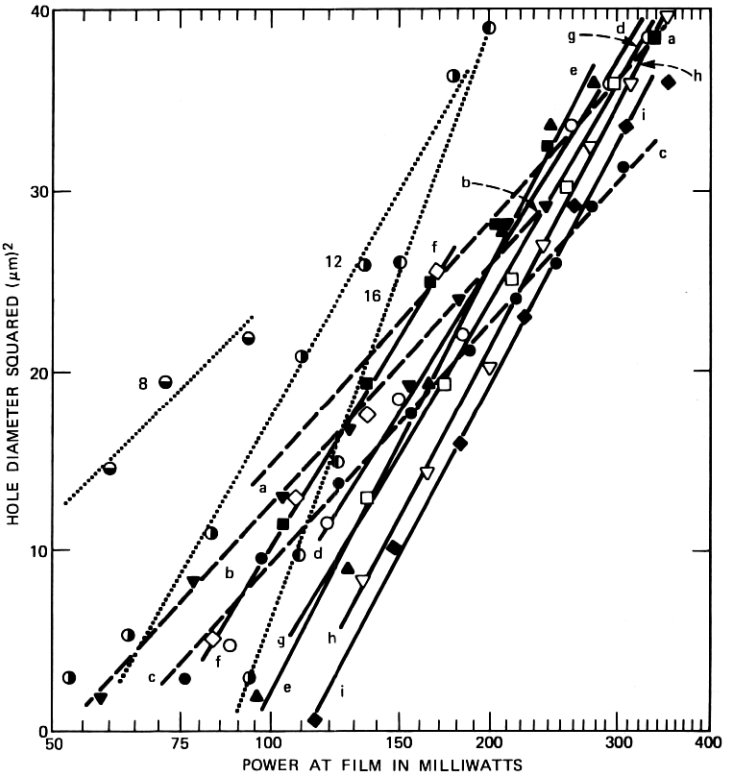

Fig. 36—Variation in machining performance of GaAs lasers; comparison with He-Ne machining. The F/3.0-focusing conditions of Fig. 33 were used to obtain machining data from a sample of nine GaAs lasers cleaved from the same wafer. Variations exist in the focused beam sizes and secondary-mode amplitudes produced by these lasers, and hence in the slopes and threshold power of their semi-logarithmically-plotted machining curves. (a, ■); (b, ▼); (c, ●)—GaAs lasers whose machining curves have small slopes and low thresholds, suggestive of a small focused-beam diameter. (d, ○); (e, ▲); (f, ◇); (g, □); (h, ▽); (i, ◆)—GaAs lasers whose machining curves have large slopes and high thresholds, suggestive of larger focused-beam diameter. ◐; ◑; ◒ He-Ne conditions of Fig. 35 for machining with 16-, 12-, and 8-mm-focal-length microscope objectives.

32 in which the secondary-mode amplitudes and the primary (machining)-mode width are both current dependent. The principal motives for considering pulse-width modulation in preference to current modulation were discussed in Section IV.

VII. PRINTER DESIGN CONSIDERATIONS

The design of a laser machining printer starts with knowledge of the machining curve and assigned values of frame width and frame writing time. These quantities determine the machining lens and the line-scan-galvanometer requirements. If suitable allowances are made for

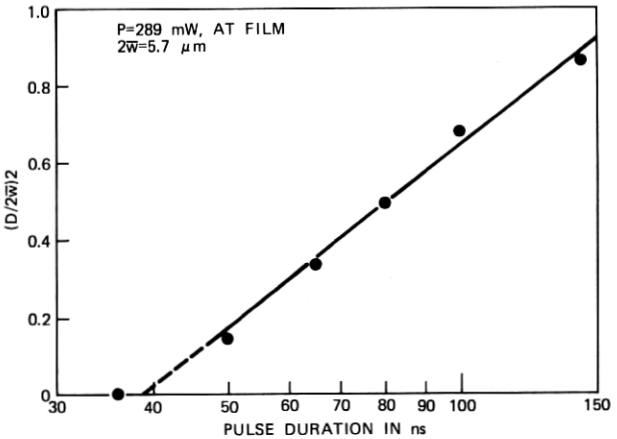

Fig. 37—Machined hole sizes versus GaAs-laser pulse duration. The laser peak-pulse current and power were kept constant, and the pulse duration was varied. The hole diameter D has been normalized to the beam diameter $2\bar{w}$ in plotting the data. Since the beam junction-plane displacements and steering-angle shifts stabilize within 30 ns of the pulse turn-on instant, all holes were machined with the same size and shape beam. The existence of secondary-mode amplitudes can still produce undesirable effects; thus, the slope of this maching curve is significantly smaller than that of a Gaussian-beam machining curve of the same threshold plotted in the normalized $(D/2\bar{w})^2$ units.

the larger apertures needed to focus GaAs laser beams, useful designs can be carried out in terms of a hypothetical Gaussian beam.

7.1 Scanning rate limitations of galvanometer mirrors

Referring to the geometry of Fig. 34, consider a frame of width W, with N contiguous machining hole sites per line, and a line-scan repetition rate ν. We assume that the beam profile is Gaussian, of diameter $2\bar{w}$ at 1/e-intensity and that the machined-hole area is defined by a single semilogarithmic curve of type A or B in Fig. 19. Then the optical power needed to machine the hole diameter W/N is a *minimum* if $2\bar{w} = W/N$, as follows from Section 5.2.1 and Ref. 2. Let ϕ be the peak-to-peak mechanical-deflection angle of the galvanometer, so that 2ϕ is the field angle subtended by W at the machining-lens principal plane. Let $2a$ be the $1/e^2$ intensity diameter of the beam entering the lens. The values of $\bar{w}$ and a are related by the expansion law for a Gaussian beam of wavelength λ, i.e.,

$$a \tan \phi = (\lambda/\pi\sqrt{2})(W/2\bar{w}) = (1/\sqrt{2}\pi)\lambda N. \tag{4}$$

Specifically, for $\lambda = 0.885$ μm and $N = 1600$, the line-scanning galvanometer requirements for "optimal" machining are defined by the condition $a \tan \phi = 0.32$ mm and by the scanning rate ν.

The field angle ϕ must be chosen such that the resulting mirror

dimensions yield a moment of inertia, and hence a loaded resonant frequency ν_{0L}, which satisfies the fundamental scan-linearity requirement[9]

$$\nu_{0L} \geq 2.5\ \nu.$$

The mirror is an ellipse whose dimensions parallel and perpendicular to the galvanometer axis equal $2aE$ and $2aE/\cos\psi$, as labeled in Fig. 34. The numerical factor E ($1.2 \leq E \leq 1.3$) represents the ratio of aperture width to incident-beam $1/e^2$-intensity width which is needed to avoid serious reduction of focused beam intensity by Fresnel diffraction at the aperture.[61] It is unfortunate for the realization of fast scan rates that the mirror moment of inertia depends most strongly on the major axis dimension.

Design values $W = 8$ mm frame width, $N = 1600$ hole sites/line, $\phi/2 = \pm 3.5$ degrees mirror mechanical-deflection angle, and $\psi = 40$ to 45 degrees mirror bias angle have been used in several laser-machining printers. Mirror minor and major axes of 6.8 and 9.6 mm would be needed to achieve this design with a *Gaussian* beam at 0.885-μm wavelength, and the moment of inertia of a corresponding 1.5-mm thick glass ellipse would be $I_m = 0.0114$ gm cm^2. The General Scanning Co. G-108 galvanometer,* rated for ± 4-degree mechanical deflection, has an intrinsic moment of inertia $I_u = 0.011$ gm cm^2 and an unloaded resonant frequency $\nu_{0u} = 1500$ Hz. If this galvanometer is used with the above mirror, the deflection-system loaded resonant frequency is $\nu_{0L} = [I_u/(I_m + I_u)]^{1/2}\nu_{0u} = 1050$ Hz, whence acceptable scan linearity would be expected for line repetition frequencies smaller than 420 Hz. Circular mirrors of 8-mm diameter were employed in early printers which machined images at 500-Hz line rates using the TEM_{00} beam from a cavity-dumped He-Ne laser. Good scan linearity was very hard to achieve at this rate, presumably because the limit $\nu_{0L} \geq 2.5\nu$ was being pressed too closely, but the linearity at and below 400 Hz was satisfactory.

Profiles of the collimated GaAs beam used with the 37-mm-focal-length machining lens of Fig. 34 (the F/3.6 aperture of Fig. 33) have been measured with a mechanically scanned slit. These profiles are shown in Fig. 38 superimposed on a mirror which can deflect the beam at a bias angle $\psi = 40$ degrees with some allowance for diffraction losses, assuming that the laser junction plane is oriented parallel to the 12.6-mm mirror height. The deflection-system loaded resonant frequency, when a G-108 galvanometer is used with a 1.5-mm thick mirror, is measured to be 555 Hz; hence linear sawtooth scanning should be available up to ~220-Hz scan rate, corresponding to 9-s

* General Scanning Co., Watertown, Mass., 02172.

writing time for a 2000-line frame. Acceptable scan linearity has been observed with this mirror at 166-Hz line rates (12-s frames). The mirror has also been used at this rate at F/3.0 aperture by tolerating more diffraction loss. However, its 12.6-mm height is insufficient to handle large, current-dependent beam shifts parallel to the junction. Indeed, as follows from Section 4.2.1, a mirror with this capability is impractical, and the limitation must be removed by the use of pulse-duration rather than pulse-amplitude modulation.

The model G-108 galvanometer, which has been used in nearly all our printers, can produce a linear sawtooth scan at 600-Hz rates when the external load is small compared to the galvanometer intrinsic moment of inertia. The external load (mirror plus mounting seat) must be kept below 0.025 gm cm^2 to maintain linearity at sawtooth scan rates of 500 Hz. The mirror principal-axis of inertia should be aligned with the galvanometer axis to achieve even loading of the shaft bearings. The mirror moment of inertia can be reduced significantly by tapering, as illustrated by the dimensions t_1 and t_2 in Fig. 38. The taper is formed prior to grinding the front of the mirror optically flat. No trouble has been encountered in maintaining flatness during sawtooth deflection up to 500-Hz line rate, but considerable art is needed to avoid flatness distortions when the mirror is affixed, either by epoxy or by mechanical clamping, to the galvanometer shaft. Such distortions can easily exceed $\lambda/2$, and are among the most frequent causes of low machining efficiency and poor images. A total thickness $(t_1 + t_2) \geq 1.5$ mm is usually needed to preserve $\lambda/4$-quality flatness after mounting when mirrors larger than about 10-mm diameter are used. Hence a moment of inertia of about 0.05 gm cm^2 is expected for a practical mirror (viz., Fig. 38) used with a GaAs laser in the machining geometry of Fig. 34. Factor-of-2 reductions in the moment of inertia of glass mirrors have been obtained, apparently without impairing the mirror flatness, by honey-combing the back of the glass blank, but such mirrors have not yet been used in a fast-scan-rate printer.

The mirror width needed to accommodate a given beam diameter can be reduced by 30 percent, and the mirror moment of inertia by nearly a factor of 3, if the machining geometry of Fig. 34 is modified so that the beam is normally incident onto the mirror ($\psi = 0°$). This is readily accomplished by using the scanning lens in a double-pass mode[62] as shown in Fig. 39. This usage exploits the fact that focus is flat over a plane, so that rays which appear to diverge from a point such as a′, located in the focal plane an appropriate distance above or below the scanned line, can be collimated by the lens, reflected from the galvanometer mirror at a small bias angle ψ, and refocused onto the line being scanned. A smaller scanning lens can be used because the entrance-pupil-to-lens distance need now be only a few millimeters,

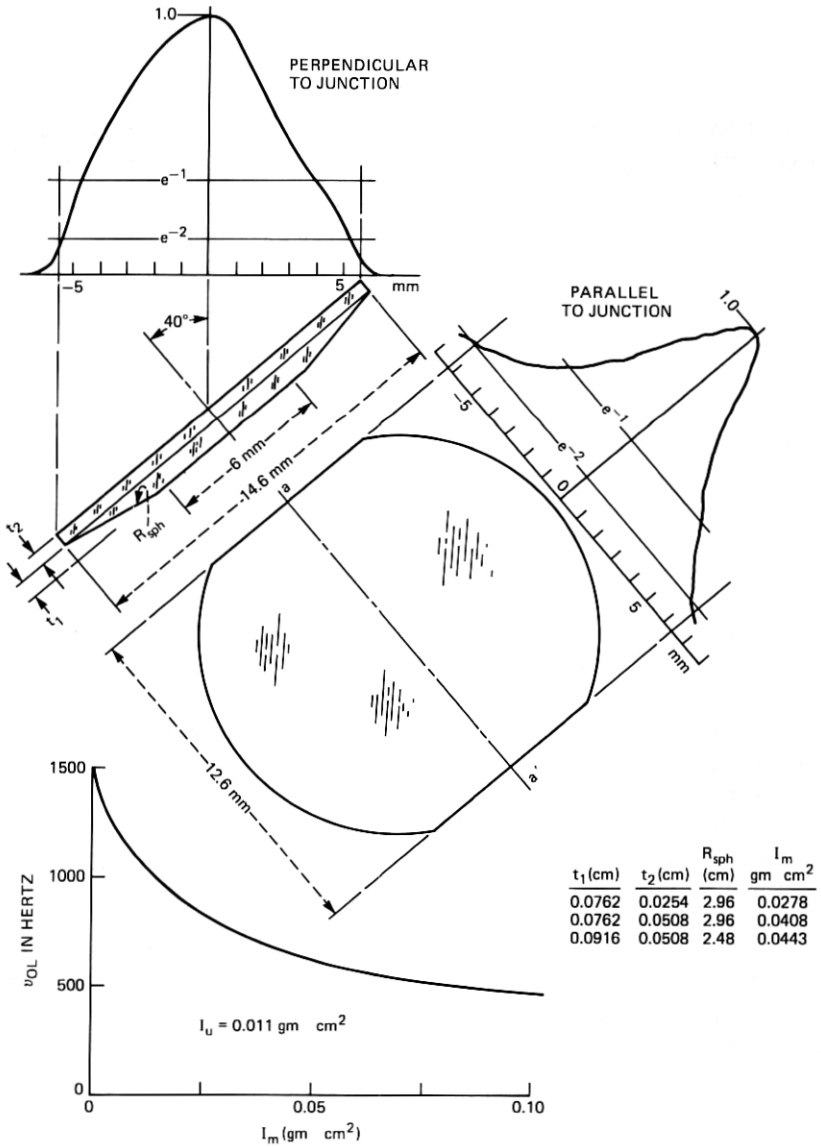

t_1 (cm)	t_2 (cm)	R_{sph} (cm)	I_m gm cm^2
0.0762	0.0254	2.96	0.0278
0.0762	0.0508	2.96	0.0408
0.0916	0.0508	2.48	0.0443

Fig. 38—Galvanometer-mirror properties. The mirror is deflected about axis aa′, and the beam is incident onto it at an angle of 40 degrees to the normal. The laser junction plane is oriented parallel to axis aa′. Profiles of the beam, as enlarged and collimated by an F/7 Galilean telescope preparatory to machining by a 37-mm-focal-length machining lens, are shown. The mirror moment-of-inertia I_m is strongly influenced by the thicknesses t_1 and t_2. Difficulty in maintaining $\lambda/4$ flatness of this mirror surface is encountered if $(t_1 + t_2)$ is smaller than 1.5 mm. The deflection-system loaded resonant frequency is also shown as a function of I_m for a G-108 galvanometer, whose unloaded moment-of-inertia I_u equals 0.011 gm cm^2.

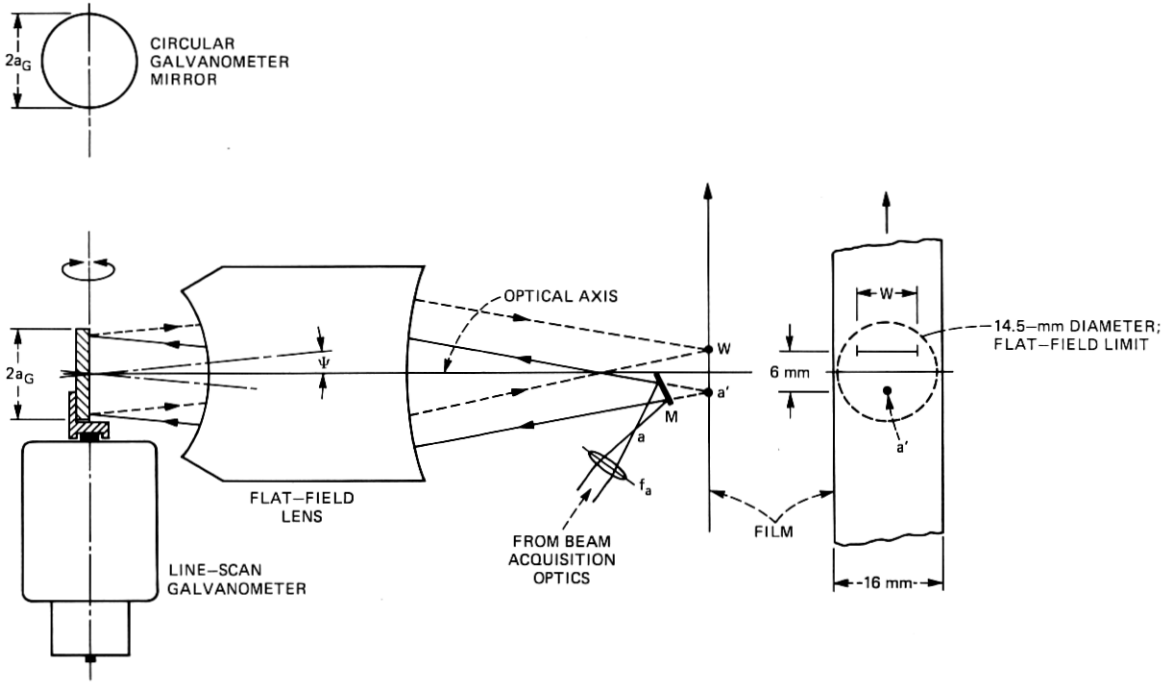

Fig. 39—Double-pass machining optics for higher scan rates. Lens f_a is a microscope objective chosen to produce a beam waist at point a equal in size to the desired machining beam waist. The small steering mirror M produces a virtual image of point a at point a' located in the film plane about 3 mm below the flat-field-lens optic axis. The beam diverging from M is collimated by the flat-field lens and made incident onto the galvanometer mirror at an angle $\psi = 4.6$ degrees to its normal. After deflection by the moving galvanometer mirror, the beam is refocussed by the flat-field lens to the appropriate point on the scanned focal line in the film. The scanned line of length W is located 3 mm above the optic axis.

and symmetries of the double-pass geometry may permit other simplifications in the lens design. Although assembly of a double-pass machining system has required some extra care, its machining quality with GaAs lasers at 160-Hz line scanning rate has been the same as that of the Fig. 34 single-pass system.

Marginally acceptable scan linearity was obtained for images machined at 500-Hz line rate with the double-pass geometry when a 9-mm-diameter mirror, tapered similarly to the example in Fig. 38, was used, with approximately 35 percent of the 2-ms line period allotted to flyback. Unfortunately, the image quality at this higher printing speed was unacceptable for the reasons mentioned in Section 4.4.2: namely, nonuniform hole sizes were machined in correlation with the laser line-averaged duty factor. At high pulse-repetition rates, the varying facsimile-information content produced temperature variations at the p-$n_{0.02}$ junction which prevented the laser from operating along a unique or predictable machining curve. The laser mounting stud was cooled thermoelectrically to maintain the p-active region at 20°C at 1-MHz pulse rate and prolong laser life, but the heat sinking was ineffective in damping temperature fluctuations produced on a millisecond time scale. Examples of such hole size nonuniformity are shown in Section 8.3.

7.2 Frame-scan, film-gate, and frame-projection considerations

A very high degree of smoothness in the frame scan (slow scan) is essential for image uniformity. Hesitations, slippages, or jerkiness which produce abrupt changes as small as a few microns in the spacing between adjacent scanned lines are highly visible in the final image—the more so if the discontinuities occur periodically along the frame length. A close match of the film to the focus of the line scan is similarly essential. A tilt of the film by one milliradian with respect to the line-scan focus can cause the beam size at the film to vary sufficiently over an 8-mm frame width to produce noticeable gray-scale variations from side to side in the final image.

Early printers that used a flat-field scanning lens were designed for stationary-frame, real-time viewing as sketched in Fig. 40a. The film was tensioned over a rectangular, frame-size opening in a smooth metal plate, nominally coincident with the focal plane of the scanning lens, and was vacuum-chucked around the perimeter of this opening. The vibrating-diaphragm pump which produced the film hold-down vacuum was also used to draw off the metal "tektites" which are sprayed out from the film during machining in a well-aligned printer. The line-scanning galvanometer was mounted in a gimbal whose axis passed through the center of the mirror orthogonally to the galvanometer axis and to the machining-lens optical axis. The gimbal axis was direct-

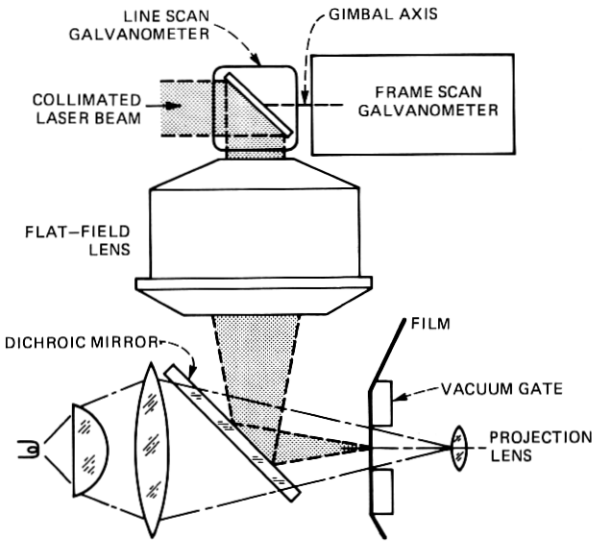

(a)

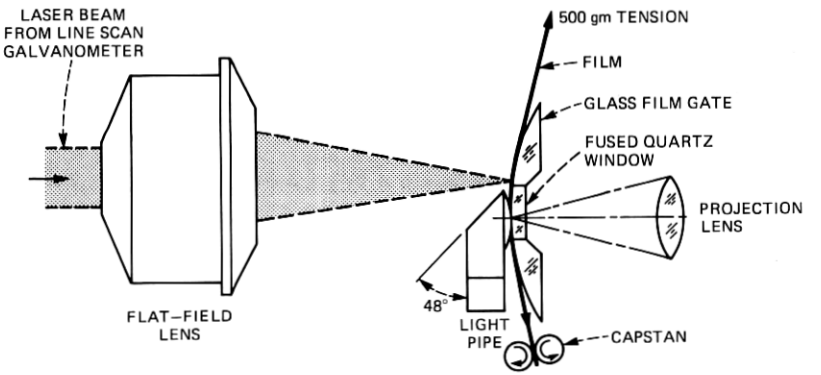

(b)

Fig. 40—Stationary-frame and moving-film machining systems. (a) The film is free-standing in the gate opening; the vacuum system which clamps it down around the perimeter of the opening is not shown. This vacuum system also draws away the metallic "tektites" which are usually evolved during machining and prevents their redeposition on the film. The line scan occurs in the plane of the drawing. (b) The line scan is perpendicular to the plane of the paper. An elastic putty is used as the dashpot fluid for damping the film-transport capstan.

coupled to the shaft of a heavy-duty, slow-scan galvanometer (General Scanning Co. G-300 series). A $\lambda/4$-flat dichroic mirror between lens and film reflected the infrared machining beam onto the film and simultaneously transmitted visible light from a projection lamp to the

film. The beam was focused by adjusting the machining lens. The gimbal-drive galvanometer slowly scanned the machining line down the length of the frame, producing a stationary final image which became visible instantly as it was machined.

Such real-time viewing has putative esthetic value but numerous engineering problems: the free-standing frame area must remain coincident with the machining focal plane in the face of temperature variations caused by its continuously changing absorption of projection light, severely limiting the tolerable projection brightness; the slow-scan galvanometer cannot be damped heavily enough to be free of microphonic vibrations and jerkiness; the scanning lens must be designed with an awkwardly long working distance and the projection-lamp optics with large diameters to accommodate the dichroic mirror; and the mirror itself is expensive and must be provided with twist and tilt adjustments. The microphonic vibration problem was particularly intransigent.

These defects can be avoided by abandoning the attempt to write in strict real time and by using instead a heavily damped film transport for the frame scan, with the film stretched at high tension over a glass cylindrical surface, as depicted in Fig. 40b. A rectangular, optically flat, fused-quartz window was set into this detail, tangent at its edges to the two cylindrical sections, whose radius of curvature was 50 mm. Machining occurs along a line close to the boundary between one cylindrical surface and the flat window, and the machined portion of film is transported over the window as frame machining proceeds. The distance between the machining line focus and the position at which the image first becomes visible in the projection field is approximately one-tenth of a frame height. Following this delay, the written frame moves steadily into the projection field and comes to rest, centered in the field, a short time after the last line has been machined. The film was tensioned at 500 gm, which forced it to be flat within ± 2 μm across the machining line (well within the focused-beam-waist field depth) but maintained it free-standing about 25 μm away from the optical flat. This latter spacing is sufficient to wash out the effects of color fringes which would occur in the projected image if the film were in more intimate optical contact with the flat. The damping dashpot responsible for the continuity and linearity of the frame scan used Dow Corning bouncing putty as the viscous fluid, the friction disk being driven by a 300-ounce-inch synchronous motor.

A projection illumination flux of 7.5 lumens was obtained from a fan-cooled, 80-W, quartz-iodine projection lamp with an integral focusing reflector. A fused-quartz light pipe was used to convey this light from the rear of the printer enclosure to the film. A prism reflector and a 20-mm-focal-length lens at the end of the light pipe (viz. Fig.

40b) directed the light through the film and into an F/2 projection lens of 19-mm focal length, causing an image of the frame to be rear-projected onto an 8.5 × 11 in., frosted-glass screen via two path-folding mirrors. The brightness of the final projected image, including a gain factor of 1.5 from the forward-scattering frosted screen, was 17 foot-lamberts. The screen was highly directional despite its low gain, providing satisfactory viewing contrast at forward angles even with a 160-W fluorescent lighting fixture operating directly overhead. Projection-flux power densities up to 150 mW/cm^2 at the film have caused no problems with film flatness or film overheating, in contrast with the film buckling which afflicts stationary-frame printers at high projection-lamp brightness. The scanning lens in the moving-film printer was cantilevered from the film-gate support by Invar rods (not shown) to maintain machining focus against ambient temperature changes. The machining and projection optics for either the stationary-frame or the moving-film systems can easily be fitted into the confines of conventional, desk-top, microfiche or microfilm viewers. A photograph of a GaAs laser printer utilizing the moving-film system and the projection optics just described is shown in Fig 41.

VIII. MACHINED-IMAGE QUALITY

The ultimate quality of laser-machined images, limited by the number of hole sites allotted to each frame and by the reproducibility of the machining curve, can be very high. The quality achieved in practice is determined for high contrast black-and-white images primarily by the linearity and smoothness of the raster scan, and for gray-scale images both by scan linearity and by the shape and reproducibility of the machining curve near threshold. Attempts have not been made in the present stage of printer developments to match the video-amplifier gain curve dynamically to the overall machining curve of a GaAs laser and Se/Bi film sample. Hence, only the expected result can be reported: the contrast, boldness, and edge-sharpening adjustments which produce best high-contrast performance differ, in general, from those which produce best gray scale. Consequently, the images machined in Se/Bi film in a printer assigned to general facsimile use are the result of compromise. If the printer is committed to black-white graphics use, there is no need to compromise.

8.1 Facsimile images

Facsimile signals were generated from original documents by two methods. In the first method, the page was raster-scanned by a He-Ne-laser, double-galvanometer, flying-spot scanner which used a photomultiplier to detect the document red-light reflectivity. In the second method, the length of the page was mechanically scanned by an

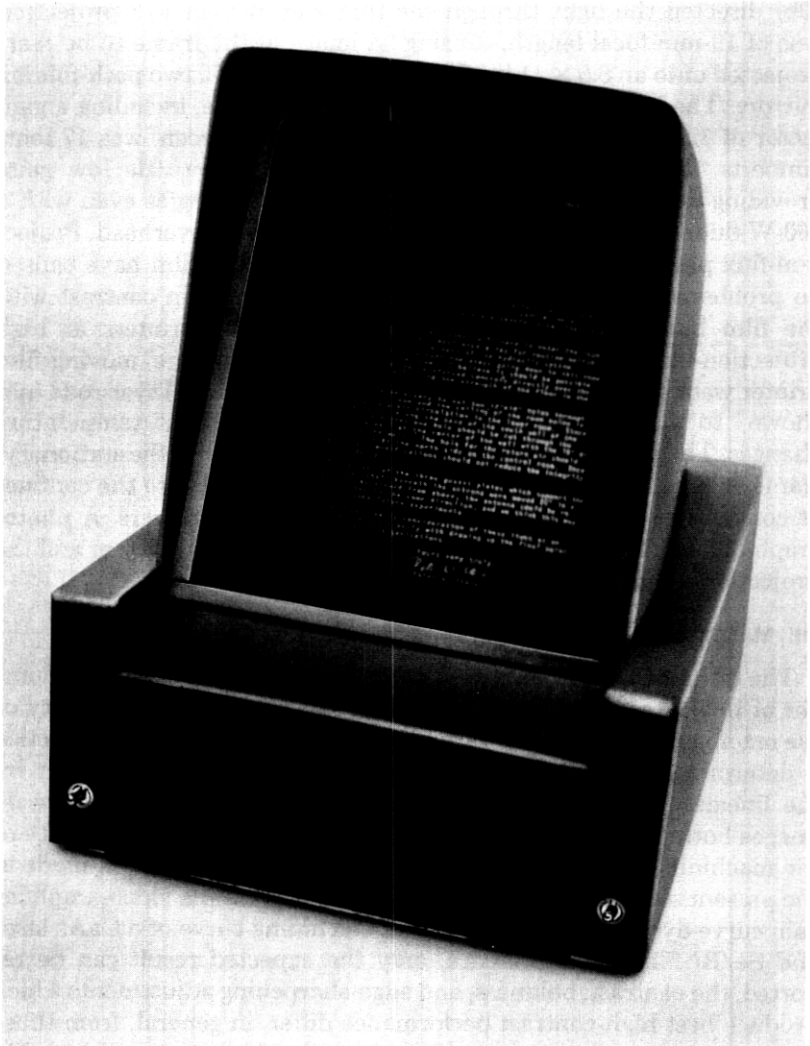

Fig. 41—Desk top gallium-arsenide laser printer. The viewing screen size is 8.5 × 11 inches.

assembly which provided white-light illumination and employed a 1728-element, linear, charge-coupled photodetector* to effect the line scan. Figures 42a and 42b are photographic enlargements of 7.7-mm-wide frames machined on Se/Bi/IBM film by a GaAs-laser printer. This printer acquired the beam with the optics of Fig. 31b and

* CCD 121 Linear Image Sensor, manufactured by Fairchild Semiconductor Components Group.

(a)

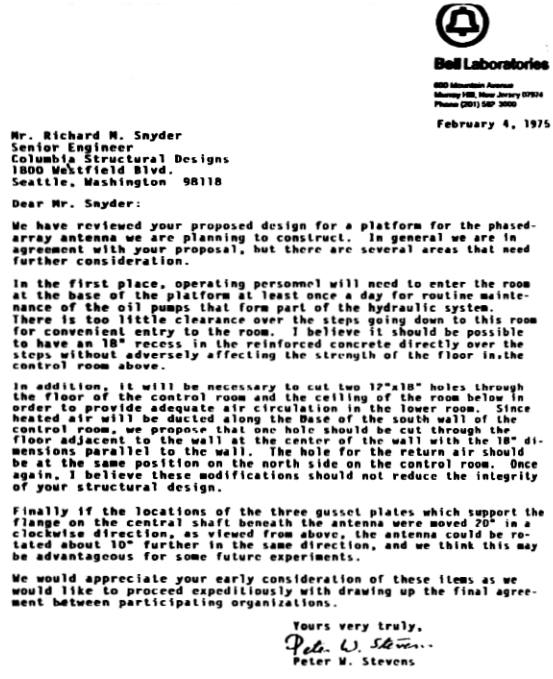

Bell Laboratories

February 4, 1975

Mr. Richard M. Snyder
Senior Engineer
Columbia Structural Designs
1800 Westfield Blvd.
Seattle, Washington 98118

Dear Mr. Snyder:

We have reviewed your proposed design for a platform for the phased-array antenna we are planning to construct. In general we are in agreement with your proposal, but there are several areas that need further consideration.

In the first place, operating personnel will need to enter the room at the base of the platform at least once a day for routine maintenance of the oil pumps that form part of the hydraulic system. There is too little clearance over the steps going down to this room for convenient entry to the room. I believe it should be possible to have an 18" recess in the reinforced concrete directly over the steps without adversely affecting the strength of the floor in.the control room above.

In addition, it will be necessary to cut two 12"x18" holes through the floor of the control room and the ceiling of the room below in order to provide adequate air circulation in the lower room. Since heated air will be ducted along the base of the south wall of the control room, we propose that one hole should be cut through the floor adjacent to the wall at the center of the wall with the 18" dimensions parallel to the wall. The hole for the return air should be at the same position on the north side on the control room. Once again, I believe these modifications should not reduce the integrity of your structural design.

Finally if the locations of the three gusset plates which support the flange on the central shaft beneath the antenna were moved 20° in a clockwise direction, as viewed from above, the antenna could be rotated about 10° further in the same direction, and we think this may be advantageous for some future experiments.

We would appreciate your early consideration of these items as we would like to proceed expeditiously with drawing up the final agreement between participating organizations.

Yours very truly,

Peter W. Stevens

(b)

Fig. 42—Quality of laser-machined facsimile images. Photographic enlargements of facsimile images of two types of subject matter as machined in Se/Bi/IBM films by a GaAs-laser printer are shown. The laser pulse repetition rate was approximately 0.33 MHz and the line scan rate approximately 160 Hz (with 30-percent allowance for flyback time). The machined frames are 7.7-mm wide, and their facsimile signals were generated by scanning with a linear charge-coupled detector.

machined with the stationary-frame optics of Fig. 40a, utilizing pulse-intensity modulation rather than pulse-duration modulation to vary the machined-hole size. Facsimile signals for these 2000-line frames were obtained from the charge-coupled photodetector operated at 160-Hz line repetition rate. The ramp for the printer line-scan galvanometer was synchronized to this photodetector electronic scan at the start of each line.

Resolution and gray scale both suffer in the photographic processing of Fig. 42, relative to the image quality perceptible in ×20 rear-projection enlargements of the microimages onto a ground-glass screen. Six-point type can just be read in the machined IEEE test charts of Fig. 42a, whereas four-point material can be read in the rear-projection enlargements, with only minor difficulties caused by line-scan jitter, edge raggedness, and missing holes. Gray-scale tonality in the GaAs-produced frames ranges up to seven distinguishable shades when viewed under rear-projection conditions. (Twelve distinguishable shades have been attained on 10.3-mm-wide frames which were machined by a cavity-dumped YAG-laser printer, using similar subject matter scanned by the He-Ne flying-spot scanner.) Image defects are noticeable even in casual inspections of Figs. 42a and 42b, and their number increases as the inspection becomes more detailed and critical. Examples of the most frequently occurring defects are presented in Section 8.3.

8.2 Synchronized images

The resolution of fine detail in the facsimile images just illustrated falls short of the ultimate which could be expected of frames containing 3.3×10^6 picture elements. Lack of synchronization between the laser pulse timing and the galvanometer-mirror instantaneous position is the largest factor in this shortcoming. The examples below demonstrate that such synchronization is inappropriate in general facsimile usage, since it runs the danger of producing a beating phenomenon (moiré fringes) in the images of documents containing finely-spaced periodic structures. However, synchronization can be employed to great advantage with computer-generated images, as shown in Fig. 43.

Figure 43a represents a microphotograph of a portion of a machined image obtained in a facsimile application. It illustrates the edge raggedness characteristic of random pulse timing with respect to the line-scan start and of a galvanometer employing neither position- nor velocity-sensing feedback. Figure 43b illustrates an ASCII-coded graphics application. Alphanumeric graphics were generated by converting 8-bit ASCII code into a 16x20-element matrix of machining hole sites; a row of ASCII characters was translated by a minicomputer into machining instructions for 20 rows of holes which were transmitted to the printer synchronously with a staircase sweep applied to a line-

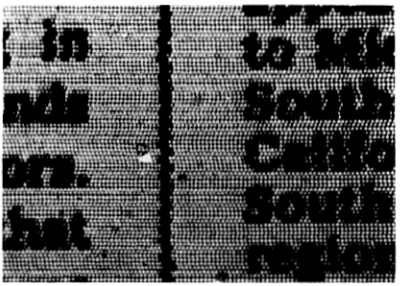

(a)

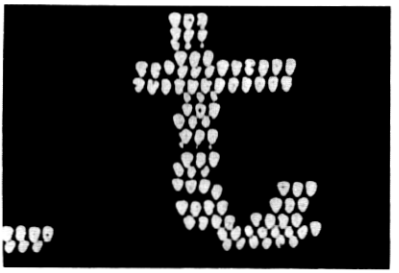

(b)

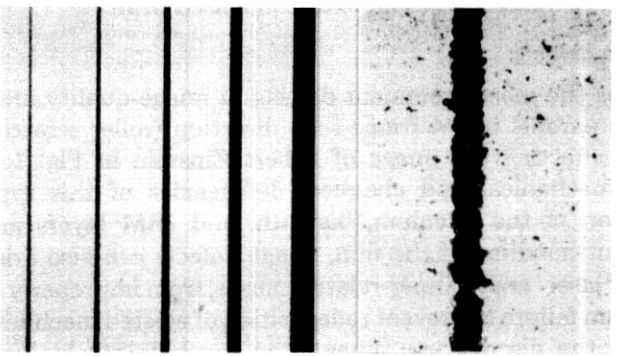

(c) (c′)

Fig. 43—Effects of pulse synchronization on the definition of vertical edges in facsimile use and in computer-graphics use. (a) Laser pulses free-running with respect to start of line scan; no position- or velocity-sensing feedback used with line scan. (b) An alphanumeric graphic character from moving-film printer. The laser pulses are synchronized to the edges of a 20-Hz-line-rate staircase sweep applied to the galvanometer, using position-sensing feedback. Vertical edges are defined to within about ±0.5-hole diameter. (c) Laser pulses synchronized to scanned-beam instantaneous position; the direction of line scan is from left to right. Photograph (c′) is an enlargement of the narrowest line in (c) and represents a line exactly one hole-diameter wide. Vertical edges are defined to within ±0.1-hole diameter.

scanning galvanometer. Well-shaped characters were obtained by synchronizing the laser pulses to edges of the staircase and by using a position-sensing feedback capacitor to assure galvanometer deflection reproducibility from line to line. Figure 43b is an enlarged microphotograph of one such character.

The best vertical edge definition yet achieved in a laser-machining printer geometry is depicted in the microphotographs of Figs. 43c and 43c′. These vertical lines were machined in a raster-scanned application in which a secondary laser beam, collinear with the machining beam*

* The machining beam for Figs. 43c, 43c′ was obtained from a cavity-dumped ArII laser.

but differing from it in wavelength, was deflected by the galvanometer, separated out by a dichroic mirror, and made incident onto a ruled transmission grating located in a (mirror-image) focal plane of the scanning lens. The pulse count generated in a detector placed behind the grating measured the instantaneous beam position and was used to synchronize the output information from a minicomputer. The resolution provided by the focused secondary-beam size and the grating ruling density was higher than 1600 sites per line and, with suitable signal processing, permitted the machining of long straight lines exactly one hole-diameter wide, as in Fig. 43c. This width corresponds to 0.005 in. on an 8.5-in. wide page, smaller than the line width of two-point characters, and suggestive of a capability for handling computer-generated mathematical text and extracondensed print.

8.3 Image defects

Perhaps the most prominent defects in image quality are the long striations parallel to the frame-scan direction (roller scratches), such as those affecting the image of Albert Einstein in Fig. 1c. Beyond obvious mechanical and chemical deficiencies of this type in the preparation of the selenium, bismuth, and IBM layers and in the subsequent handling of the film, image defects can also arise from a variety of laser- and scanner-related causes, from improperly corrected optics, from failure to prevent redeposition of ejected machining debris, and from the discreteness inherent in the hole machining method. Some of these are illustrated in Figs. 44, 45, and 46 for GaAs-laser facsimile images.

Fig. 44

(a) Frame-scan discontinuities (D)—microphonics, caused by rapping the printer table, affected the gimballed frame-scanning galvanometer; this highly visible defect is not seen with strongly damped, film-transport scans.

(b) Line-scan nonlinearity—the line-scanning galvanometer is moving faster (F) and slower (S) than its average speed in the indicated regions; the defect is difficult to correct only when the scan rate exceeds 40 percent of the galvanometer loaded resonant frequency.

(c) Line-scan wobble—bad galvanometer bearings caused waviness in the scan lines, most easily seen here in region VV; local bunching of lines (bands W) produces short, horizontal, dark lines in the image which are highly visible.

(d) Frame-scan nonlinearity—regions of faster- and slower-than-average frame speed, indicated by (F) and (S), occur both with gimballed galvanometer and with film-transport frame scans.

Fig. 45

(a),(a′) Moiré effect—a position-sensing line-scan galvanometer was used, with machining synchronized to the start of the scan, for facsimile

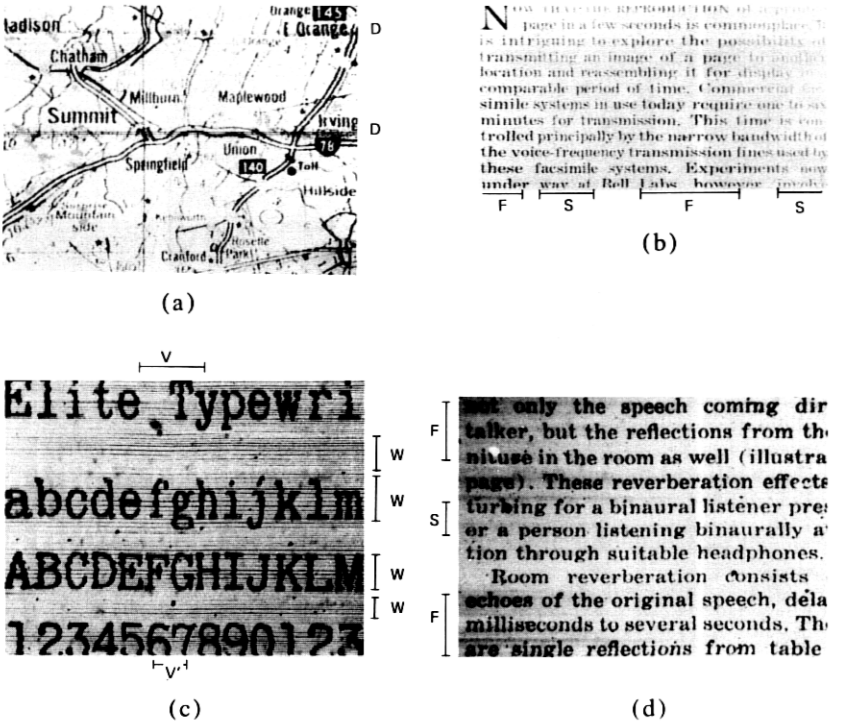

(a) (b) (c) (d)

Fig. 44—Image defects. Various defects caused by line- and frame-scan irregularities, as described in text.

image (a); a strong moiré beat results from the attempt to reproduce the dot array in the original (a′) with the regular-hole array of the facsimile.

(b) Moiré effect—galvanometer did not utilize position- or velocity-sensing feedback, and laser pulses were unsynchronized with start of line scan; moiré beat in halftone background (Atlantic Ocean) is weaker than in Fig. 45a.

(c) Bad machining in center of frame—film buckled out of the machining focal plane during "real-time" printing due to overheating by projection illumination; a limitation with the stationary-frame printer of Fig. 40a, but not with the moving-film printer of Fig. 40b.

(d) Badly machined holes—poor transmission in "white" areas, caused by balled-up metal remaining in center of each hole (confirmed by secondary electron microscopy); typical of machining produced by poorly corrected optics and/or a nonplanar galvanometer mirror.

Fig. 46

(a),(a′) Duty-factor-dependent machining—given a 500-Hz line-scan rate and the indicated directions of line and frame scans, note that

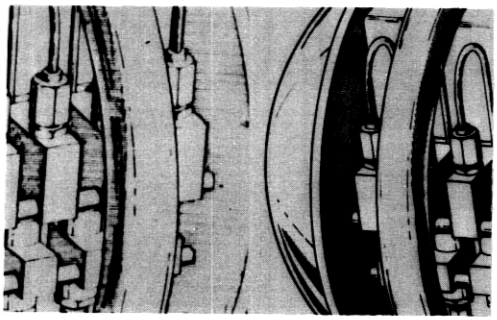

(a) (a′)

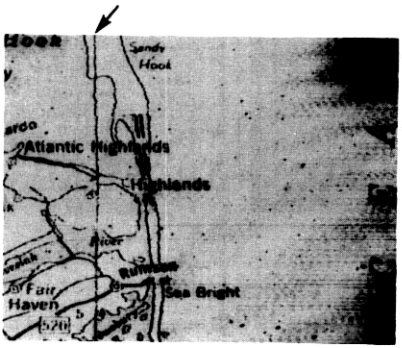

(b)

(c)

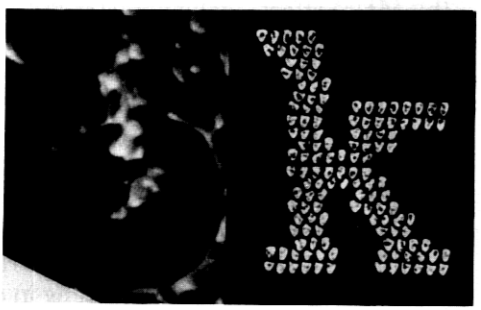

(d)

Fig. 45—Image defects. (a) Moiré effects in facsimile. (a′) Original of (a). (b) Moiré effect. (c) Film buckling. (d) Debris in holes caused by poor-optical-quality machining beam.

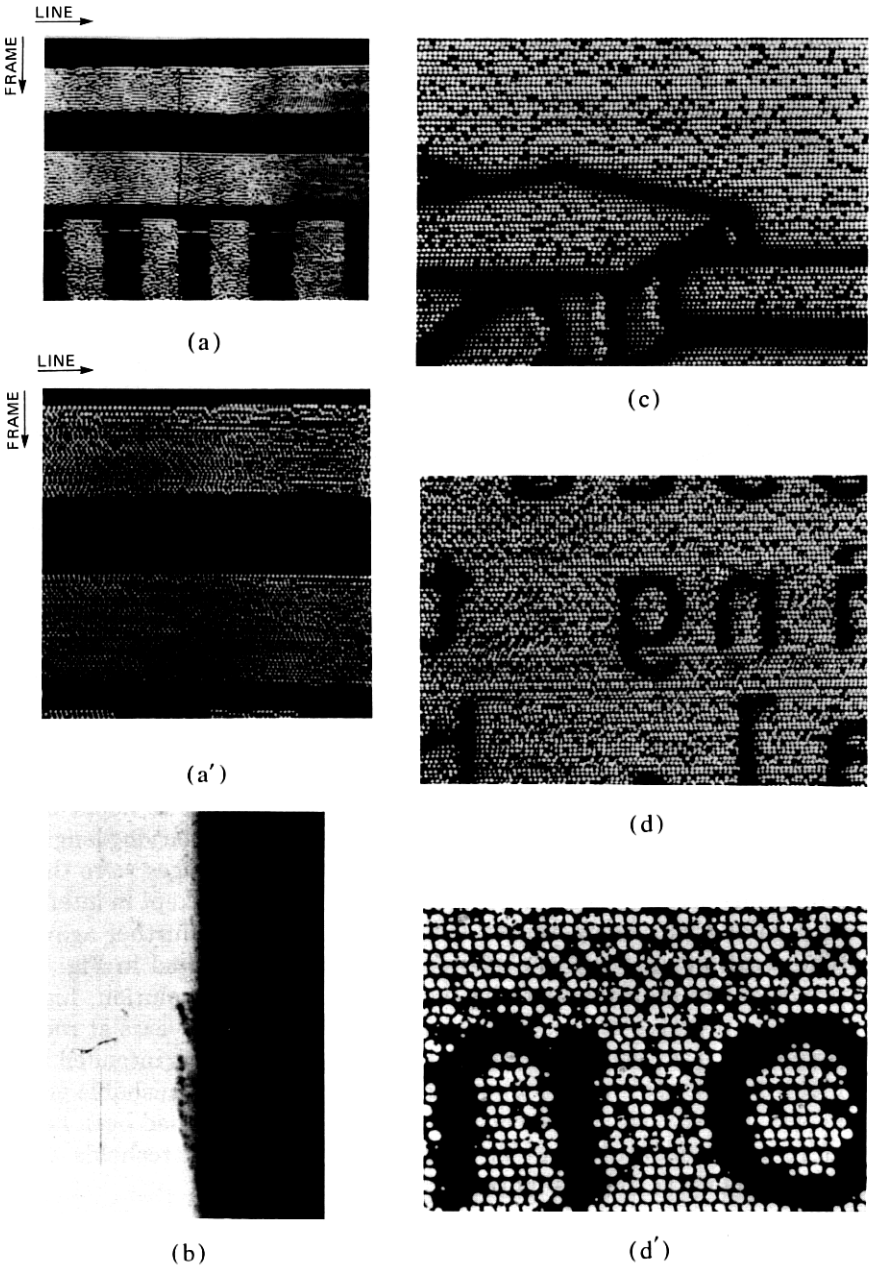

Fig. 46—Image defects. (a), (a′) Laser overheating at high printing speed. (b) Redeposition of machining debris. (c), (d), (d′) Erratic machining caused by reflection-induced instabilities.

holes produced at 1-MHz pulse-repetition rate slowly decrease in size and quality along the length of a scanned line. The laser temperature does not completely recover during flyback time at the 500-Hz line-scan rate, so the hole-quality degradation accelerates with successive scans of high-duty-factor machining. However, if the laser is left off for several lines, the temperature recovers, and large, well-shaped holes reappear when machining resumes.

(b) Redeposition of machined bismuth—metal, evolved from Se/Bi/IBM film during machining at 0.3-MHz repetition rate, is shown redeposited on uncoated margin of film. This effect can impair image quality if redeposition is permitted to occur within the frame, as in "Madison-Summit" area of map, Fig. 44a. Its effect can be more serious at 1-MHz repetition rate where the bismuth, when allowed to redeposit ahead of the raster scan, has raised the machining threshold enough to prevent machining.

(c),(d),(d′) Reflection-induced beam destabilization—this effect, described in Section 4.2.3, can cause holes to be omitted (c), or to be both omitted and misshapen (d), (d′).

Means for curing or avoiding most of the defects illustrated in Figs. 44, 45, and 46 have been described in the preceding sections.

8.4 Image quality of aged film in high contrast use

Extensive time-temperature stress tests conducted on the Se/Bi/IBM/Mylar film system over the temperature range 25° to 60°C yield an activation-energy value of 24 Kcal/mole for the aging process responsible for degraded film machining, assuming that the process corresponds to a single activation energy at these temperatures. Under this assumption, one week of life at 60°C is equivalent to about one year of life at 25°C. Film samples were aged at 60°C for varying lengths of time up to 20 weeks, and high-contrast negative images were then simultaneously machined in them. (Aged samples were kept in interim storage at 4°C, a temperature which strongly inhibits further aging.) The results for 2-, 10-, and 20-week samples, as depicted in Fig. 47, provisionally indicate that the film can yield high-resolution, high-contrast, negative images after a time equivalent to 10 years at room temperature. A second test, made in a printer which was intended for high contrast use and which produced only a few distinguishable gray levels, showed that three-year-old films of Se/Bi which had been kept at room temperature provided the same machining thresholds and image quality as did freshly prepared film.

IX. SUMMARY AND DISCUSSION

Miniature archival images have been machined in Se/Bi film with the galvanometer-deflected beam from a pulsed-current GaAs laser.

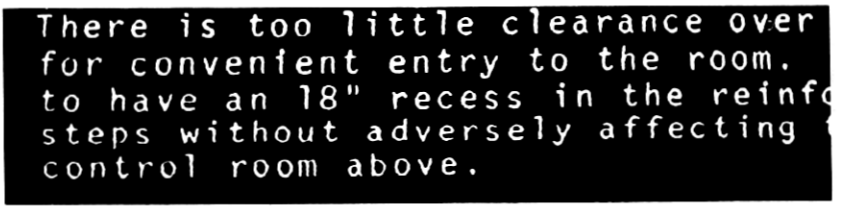

(a)

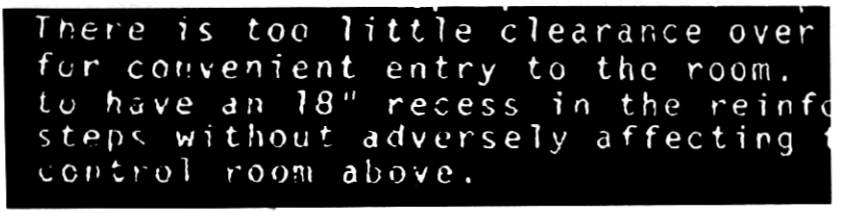

(b)

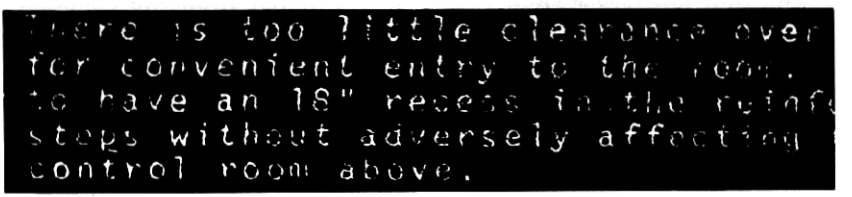

(c)

Fig. 47—Aging of Se/Bi/IBM film in high-contrast use. Figures (a), (b), and (c) refer to Se/Bi/IBM Mylar film samples which had been aged at 60°C for 2, 10, and 20 weeks, respectively, prior to machining of computer-generated negative images by the moving-film printer. Given an activation energy of 24 Kcal/mole for the film-degradation process, image (b) corresponds to high-contrast machining on film aged for 10 years at 25°C.

High resolution is readily available with this image-forming method. Frames containing 3×10^6 machining hole sites and demonstrating up to seven distinguishable gray levels have been written in 12 seconds. Machined white background areas of the film are about 50 percent transparent to visible projection illumination, and unmachined areas are less than 1 percent transparent. Information can be added to unmachined frame areas at later times, up to a limit set by the shelf life of the film. The images can be viewed instantly as they are written.

Polymer-undercoated Se/Bi is the most sensitive metal film system for the GaAs wavelength which exhibits mechanical integrity and good shelf life. At present, the room-temperature shelf life of this film for high-contrast (black-white) printing exceeds 10 years, and the archival

life of machined images probably exceeds several centuries. Further development effort on Se/Bi film might concentrate on extending shelf life and improving the compromise between low machining threshold energy and adhesion. Rather sketchy aging data suggest that present GaAs machining lasers can have commercially adequate life when used at 12-s frame rates. However, attempts to reduce the frame machining time to 4 seconds have foundered on laser thermal diffusivity limitations, and this printing speed also strains the capabilities of the line-scan galvanometer.

Junction-plane secondary modes, which do not contribute to hole enlargement, are usually present in the pulsed output of proton-delineated, stripe-geometry, double-heterostructure GaAs lasers when their current exceeds lasing threshold by 10 or 20 percent. As a result, the total power which must be drawn from present lasers to obtain enough peak intensity at the Se/Bi film to machine 8×10mm images often exceeds by 50 percent or more the power that would suffice if only the fundamental beam mode were present. Also because of the junction-plane modes, the numerical apertures required in the deflection and writing optics to focus the main GaAs machining lobe into a given size at the film are larger than would be calculated from the Gaussian beam propagation law. Recent progress in high-power buried-stripe heterostructures provides hope that most of these laser-related printing problems will eventually yield to satisfactory technical compromise.

X. ACKNOWLEDGMENTS

The development of laser-machining facsimile receivers started in 1970 with initial contributions from D. Maydan and R. Sard, and has been concentrated since 1973 on the Bi-Se film system and the GaAs laser. A large number of coworkers have been associated with the project since its beginning.

Contributions to metal film studies have been made by D. J. Bartelink, E. W. Chase, P. S. Henry, and D. Y. Lou, with assistance from C. Van Hise and W. Q. McKnight. Contributions to the GaAs laser development were made by B. C. DeLoach, B. W. Hakki, R. T. Hepplewhite, D. C. Krupka, T.L. Paoli, N. C. Schumaker, and D. L. Van Haren. The experimental work on early GaAs printers was done by R. G. Chemelli, D. D. Cook, and D. C. Krupka, assisted by R. B. Lawry and E. W. Chapman. Work on the most recent printer was done by T. G. Melone, J. S. Wagner, A. D. White, and D. L. White. A prototype YAG-laser printer was investigated by D. Cheng, with assistance from M. C. Page; a compact, self-contained version of this printer was assembled and made operational by R. G. Chemelli and E. D. Urbanek. The charge-coupled-device page scanner was produced

by D. Cheng, E. W. Chase, R. G. Chemelli, and E. D. Urbanek. A large fraction of the diffraction-limited printer optics was designed either in prototype or final form by A. D. White. Optics fabrication was in the hands of W. Gronros and T. G.Melone. Joseph Hill was responsible for the mechanical design details of several GaAs printers.

The authors thank J. H. Brúning for permission to use results from his ArII mask-machining facility, J. S. Courtney-Pratt and his associates for the He-Ne flying-spot scanner, R. G. Chemelli for help with the preparation of this paper, and R. W. Dixon for valuable comments on the manuscript.

REFERENCES

1. H. A. Watson, Bell Laboratories Record, *53* (March, 1975), p. 163.
2. D. Maydan, "Micromachining and Image Recording on Thin Films by Laser Beams," B.S.T.J., *50,* No. 6 (July-August 1971), pp. 1761–1789.
3. H. S. Carslaw and J. C. Jaeger, *Conduction of Heat in Solids,* 2nd ed, New York: Oxford, 1959, Ch. XII.
4. C. O. Carlson, E. Stone, H. L. Bernstein, W. K. Tomita, and W. C. Myers, Science, *154* (December 23 1966), p. 1550.
5. M. B. Panish and I. Hayashi, *Appl. Solid State Science*, Vol. 4, ed. R. Wolf, New York: Academic Press, 1974, p. 235.
6. L. A. D'Asaro, J. Luminescence, *7* (1973), p. 310.
7. M. Terao et al, Proceedings of IEEE/OSA Conf. on Laser Eng. and Applic., Wash. D.C., June, 1979.
8. T. Maekawa, T. Yokokawa, and K. Niwa, J. Chem. Therm., *4* (1972), p. 873.
9. P. J. Brosens, Electro-Optical Systems Design, 4/71, p. 21.
10. D. Marcuse, *Light Transmission Optics*, New York: Van Nostrand Reinhold, 1972, Ch. 6.
11. D. D. Cook and F. R. Nash, J. Appl. Phys., 46 (1975), p. 1660.
12. R. G. Chemelli, D. D. Cook, and R. C. Miller, U.S. Patent 4,030,122 (June 14, 1977).
13. R. G. Chemelli and R. C. Miller, U.S. Patent 3,974,507 (Aug. 10, 1976).
14. T. L. Paoli, B. W. Hakki, and B. I. Miller, J. Appl. Phys., *44* (1973), p. 1276.
15. J. C. Dyment, L. A. D'Asaro, J. C. North, B. I. Miller, and J. E. Ripper, Proc. IEEE Lett., *60* (1972), p. 726.
16. H. C. Casey, Jr. and M. B. Panish, *Heterostructure Lasers; Part B: Materials and Operating Characteristics*, New York: Academic Press, 1978, Ch. 8.
17. B. W. Hakki and C. J. Hwang, J. Appl. Phys., *45* (1974), p. 2168.
18. D. C. Krupka, IEEE J. Quantum Electronics, *QE-11* (1975), p. 390.
19. B. W. Hakki, J. Appl. Phys., *46* (1975), p. 292.
20. W. B. Joyce and S. H. Wemple, J. Appl. Phys., *41* (1970), p. 3818.
21. W. O. Schlosser, "Gain-Induced Modes in Planar Structures," B. S. T. J., *52,* No. 6 (July-August 1973), pp. 887–905.
22. F. R. Nash, J. Appl. Phys., *44* (1973), p. 4696.
23. D. Marcuse, Ref. 10, Ch. 7.
24. G. H. B. Thompson, D. F. Lovelace, and S. E. H. Turley, Solid-State and Electron Devices, *2* (1978), p. 12.
25. T. L. Paoli, IEEE J Quantum Electronics, *QE-13* (1977), p. 662.
26. R. W. Dixon, F. R. Nash, R. L. Hartman, and R. T. Hepplewhite, Appl. Phys. Lett., *29* (1976), p. 372.
27. T. L. Paoli, IEEE J. Quantum Electronics, *QE-12* (1976), p. 770.
28. R. W. Dixon, W. B. Joyce, and R. C. Miller, J. Appl. Phys., *50* (1979), p. 1128.
29. H. C. Casey Jr., M. B. Panish, and J. J. Merz, J. Appl. Phys., *44* (1973), p. 5470.
30. T. H. Zachos and J. C. Dyment, IEEE J Quantum Electronics, *QE-6* (1970), p. 317.
31. J. P. J. Heemskerk et al, Proceedings of IEEE/OSA Conf. Laser Eng. and Appl., Wash. D.C. (June, 1979).
32. W. T. Tsang, R. A. Logan, and M. Ilegems, Appl. Phys. Lett., *32* (1978), p. 311.
33. M. Born and E. Wolf, *Principals of Optics,* 4th ed. New York: Pergamon Press, 1970, Section 1.6. Theoretical TE and TM reflectivity-versus-angle curves were calculated from the one-layer and two-layer M-matrix formalism.

34. F. K. Reinhardt, I. Hayashi, and M. B. Panish, J. Appl. Phys., *42* (1971), p. 4466.
35. T. Ikegami, IEEE J. Quantum Electronics, *QE-8* (1972), p. 470.
36. E. I. Gordon, IEEE J. Quantum Electronics, *QE-9* (1973), p. 772.
37. B. W. Hakki and F. R. Nash, J. Appl. Phys., *45* (1974), p. 3907.
38. R. C. Miller and W. B. Joyce, Appl. Phys. Lett., *31* (1977), p. 764.
39. W. B. Joyce and R. W. Dixon, J. Appl. Phys., *46* (1975), p. 855. A junction-temperature increase of 34° C per watt of input electrical power was calculated by Joyce for our laser structure.
40. Lord Rayleigh, Sci. Papers *3* (1902), p. 441.
41. A. E. Bell and F. W. Spong, IEEE J. Quantum Electron., *QE-14* (July, 1978), p. 487.
42. A. J. deVries, Rec. Trav. Chim., *77* (1958), pp. 383 and 441.
43. J. Bohdansky, J. Chem. Phys., *49* (1968), p. 2982.
44. J. W. Rutter in *Liquid Metals and Solidification*, Chicago: Am. Soc. for Metals, 1958, p. 243.
45. Yu F. Komnik, Fiz. metal. metalloved. *25* (1968), p. 817.
46. R. Hultgren, R. L. Orr, P. D. Anderson, and K. K. Kelley, *Selected Values of Thermodynamic Properties of Metals and Alloys*, Am. Soc. Metals, 1973; also R. C. Weast, ed., *Handbook of Chemistry and Physics*, 52nd ed., Chemical Rubber Publishing Co., 1971.
47. R. Berry, P. Hall and M. Harris, *Thin Film Technology*, New York: Van Nostrand, 1968, p. 265.
48. D. Benjamin and C. Weaver, Proc. Roy. Soc., *A254* (1960a), p. 163.
49. F. Abeles, *Advances in Optical Technology*, A. C. S. Van Heel, ed., Amsterdam: North Holland, 1967, p. 144.
50. Values of bulk optical constants may be obtained from the following sources:
    Bi: A. P. Lenham, D. M. Treherne, and R. J. Metcalfe, J. Opt. Soc. Am., *55* (1965), p. 1072; J. N. Hodgson, Proc. Phys. Soc. (London), *B67* (1954), p. 269.
    Sb: Lenham et al, ibid.
    Cd, Zn, Mg: R. H. W. Graves and A. P. Lenham, J. Opt. Soc. Am., *58* (1968), p. 58.
    Pb: A. I. Golorashkin, JETP (USSR), *48* (1965), p. 825; Soviet Phys. JETP, *21* (1965), p. 548.
    In: I. N. Shkylyarevskii and R. G. Yarovaya, Optika i Spek., *16* (1964), p. 85; Optics and Spectrosc., *16* (1964), p. 45.
    Sn: A. I. Golorashkin and G. P. Motulevich, JETP (USSR), *47* (1964), p. 64.
    Te: J. Stuke and H. Keller, Phys. Stat. Sol., *7* (1964), p. 189.
    Al: L. G. Schult, J. Opt. Soc. Am., *44* (1954), pp. 357 and 362; J. N. Hodgson, Proc. Phys. Soc. (London), *B68* (1955), p. 593.
51. M. Hansen, *Constitution of Binary Alloys*, New York: McGraw Hill, 1958.
52. Our refractive-index dispersion curve for evaporated Bi_2O_3 is intermediate between the results of P. B. Clapham, Brit. J. Appl. Phys., *18* (1967), p. 363, for sputtered Bi_2O_3 and of J. Halford and H. Hacker, Jr., Thin Solid Films, *4* (1969), p. 265, for evaporated Bi_2O_3.
53. R. A. Bartolini, A. E. Bell, and F. W. Spong, Proc. IEEE/OSA Conf. on Laser Eng. and Appl., Wash., D. C. (June 1979).
54. The bulk optical constants of selenium may be obtained from C. Froissart, C. R. Acad. Sc. Paris, *270B* (1970), p. 1544.
55. P. Chaudhari and B. Beaver, Trans. Met. Soc. *239* (1967), p. 501.
56. R. G. Crystal, J. Poly. Sci. (A-2) *8* (1970), p. 2153.
57. W. J. Smith, *Modern Optical Engineering*, New York: McGraw-Hill, 1966, Sec. 13.6.
58. H. Kita, I. Kitano, T. Uchida, and M. Furukawa, NEC Research and Development, *25* (1972), p. 21.
59. The optical path calculations were carried out by P. E. Naufnagel, Bausch and Lomb Optics Center, Rochester, New York.
60. W. J. Smith, Ref. 57, p. 131, Fig. 6.9.
61. A. L. Buck, Proc. IEEE, *55* (1967), p. 448.
62. W. J. Smith, Ref. 57, p. 434, Fig. 14.15.